FCC

March 27, 2025

Study of the feasibility of the observation of $B^0 \to K^{*0}\tau\tau$ at FCC-ee and related vertex detector performance requirements

Tristan Miralles[a], Stéphane Monteil[a]

[a] *Université Clermont Auvergne, CNRS/IN2P3, LPC, Clermont-Ferrand, France*

Abstract

The aim of the work described in this analysis note is to study the capabilities of experiments at the Future Circular Collider FCC-ee to unravel the quark transitions $b \to s\tau^+\tau^-$, unobserved to date. The decay $B_d^0 \to K^*\tau^+\tau^-$ considering the three-prongs transition $\tau \to \pi\pi\pi\nu_\tau$ is studied with a method to reconstruct explicitly the kinematics of the two undetected neutrinos. Detector requirements to observe this decay are evaluated; in particular several vertexing resolution performances are emulated and tested against this physics case. An actual detector design (IDEA) has been as well tested with FCC-ee simulations to fix a reference of the state-of-the-art performance. Analyses of simulated signal events together with simulated dominant backgrounds has been done in order to draw the precision of the $B_d^0 \to K^*\tau^+\tau^-$ branching fraction measurement as function of the vertexing resolution performances. The vertexing performance to observed this specific decay at FCC-ee is provided.

Contents

1 Introduction

The scientific context of the work summarised in this analysis note is the Feasibility Study of an e^+e^- circular collider running at the four relevant electroweak thresholds: Z pole, WW pair production threshold, H produced in association with a Z boson threshold and top quark pair production. In particular, the exquisite luminosity at the Z pole, and hence the abundant production of b-flavoured particles, provides opportunities to test Beyond Standard Model (BSM) contributions in quark transitions involving third generation fermion particles.

Canonical examples of such transitions are the semileptonic and dileptonic decays of B mesons into pairs of τ leptons, *e.g.*, the decay $B_s \to \tau^+\tau^-$ or the semileptonic quark transition $b \to s\tau^+\tau^-$.

This work is focused on the study of the decay mode $B^0 \to K^{*0}\tau\tau$, for which the Standard Model (SM) predicts a suppressed Branching Fraction at the level of $\mathcal{O}(10^{-7})$ [1]. This small branching fraction can possibly be improved by New Physics (NP) contributions [2–5]. This decay channel is unobserved to date. Only limits have been obtained [6, 7]. The main experimental challenge consists in reconstructing the neutrino(s) in the τ decays. In the absence of an explicit measurement of the missing energy, the selection of the decay channels of interest in this work is overwhelmed by b-physics background contributions.

It is actually possible to solve fully the kinematics of the decay $B^0 \to K^{*0}\tau\tau$ if one considers the final states with the three-prong decay $\tau \to 3\pi\nu$. The method is based on the explicit reconstruction of the secondary and tertiary decay vertices and will be developed in Section 3.

The conjunction of the boost experienced at the Z pole by B-meson decay particles and the potentially exquisite decay vertex reconstruction performance makes FCC-*ee* an adequate experimental environment to reach the observation of these decay channels even at the small SM prediction value.

The work described in this article has a double entangled objective: assess the feasibility of the measurement of the branching fraction at the SM value and provide vertex detector requirements (as a function of the measurement precision). The analysis uses the FCCAnalyses software that features a fast simulation DELPHES [8] of the IDEA [9, 10] detector. However, in order to evaluate the actual vertex detector requirements, arbitrarily good decay vertex reconstruction performances were emulated in order to assess the precision on the branching fraction measurement.

The note is organised as follows: The physics motivations of the study are brought in the first section. Details on the decay topology are presented below to introduce the reconstruction method in the second section. In the third section, an overview of the FCC-*ee* project and a description of its software used are given. A description of the signal mode reconstruction is then presented in the fourth section. The fifth section contains the exploration of the potential backgrounds, as well as an evaluation of the hierarchy of their importance. The development of a multivariate-based selection to reduce the background sources is explained in a sixth section. The method to assess the precision on the branching fraction measurement is then presented in a seventh section. The feasibility of the measurement and the detector requirements are eventually discussed in a eighth section.

2 Physics motivations

2.1 Semileptonic decays: BSM amplitudes in $B^0 \to K^{*0}\tau\tau$

The fermion couplings among the third-generation are the most demanding to observe experimentally, and consequently the less well-known. Specific models addressing the Flavour problem(s), *e.g.* the mass hierarchy among fermion generations and the minimal flavour violation suggested by the neutral meson mixing phenomenology, are often providing $b \to \tau$ ($m_\tau \sim 20m_\mu$) enhancement or modification w.r.t. the SM prediction. The $b \to s\tau\tau$ transition proceeds in the SM through electroweak penguin diagrams such as the one sketched in Figure 1. It should be noted that the heaviest SM particles (with the notable exception of the BEH boson) are virtually involved in the loops that contribute to the amplitude of the process. These amplitudes can *naturally* welcome new heavy degrees of freedom and are therefore sensitive to potential Beyond Standard Model (BSM) amplitudes such as those involving new gauge bosons Z' [2] or new types of particles such as leptoquarks [3, 11] for example.

The main challenge to observe $b \to s\tau^+\tau^-$ quark transition comes from the measurements of the neutrinos that occur from the lepton decays.

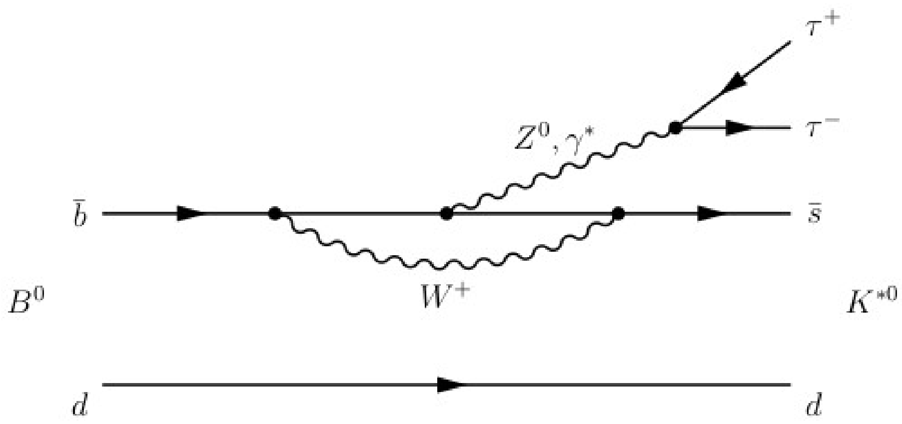

Figure 1: Feynman diagram of the $B^0 \to K^{*0}\tau\tau$ process.

2.2 Experimental status

Very scarce experimental handles do exist on the quark transitions $b \to s\tau\tau$ despite the remarkable possibilities offered by the current Flavour experiments at colliders, LHCb and Belle II. Though the LHCb experiment [12] records highly-boosted b-hadrons produced with enormous cross-sections, its geometry (a spectrometer) in conjunction with the hadronic environment does not allow to date to constrain the missing energy characteristic of these decays. By contrast, the Belle II experiment [13] benefits from a clean environment and can use the energy-momentum constraint. However, the modest boost experienced by the B-mesons at the $\Upsilon(4S)$ energy makes it difficult to resolve the τ decays. Limits on the branching fractions of the modes of interest have been, however, set, but their values are several orders of magnitude larger than the SM prediction. The simultaneous advantages of the boost at the Z pole and the experimental cleanliness of FCC-ee interactions make it an adequate laboratory to search for $b \to s\tau\tau$ quark transitions.

2.3 A comment on B-meson Lepton Flavour Universality observables

The Lepton Flavour Universality (LFU) is a consequence of the Standard Model fermion representations, that features identical couplings of the three charged leptons with the gauge bosons. Intriguing and appealing tensions w.r.t. the LFU have been reported by the LHCb experiment, in the ratios of semileptonic $b \to s\ell\ell$ transitions involving electrons or muons. The observables are defined as branching fraction ratios such as $R_{K(^*)} = BF(B \to K(^*)\mu\mu)/BF(B \to K(^*)ee)$ [14] [One needs to cite as well $R_{D]^{(*)}}$ papers]. The LHCb collaboration provided recently updated measurements [15] of these ratios. The executive summary of the results is shown in Figure 2. A fair agreement with the SM predictions is now reported, with precisions at the level of $5 - 10\%$ dominated by statistical uncertainties. The near future will shed further light on other semileptonic Flavour observables sectors, such as R_{D,D^*} [16, 17] or the $b \to s\ell\ell$ angular analyses [18, 19]. Though the tensions with the SM predictions are relaxed for some class of observables, the case to search for LFU violations in the quark transitions involving τ leptons is self-contained and remains vibrant.

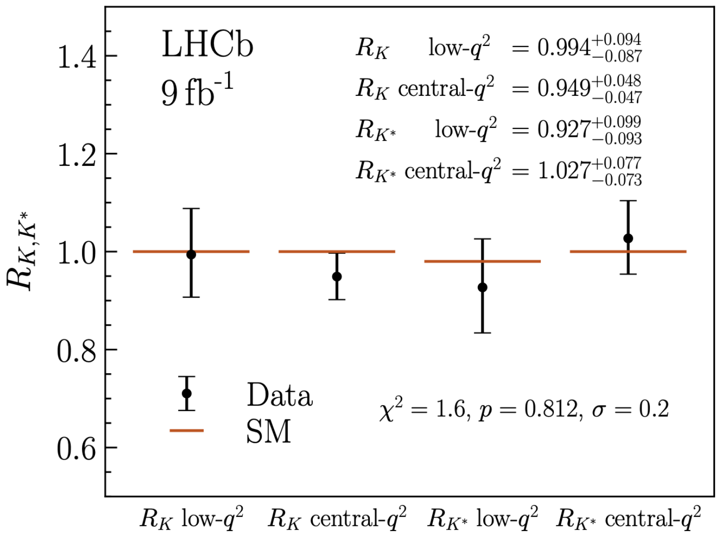

Figure 2: Summary of the 2022 R_{K,K^*} measurements performed by LHCb.

3 Topologogical reconstruction of the decay $B^0 \to K^{*0}\tau\tau$

3.1 The topology of $B^0 \to K^{*0}\tau\tau$ events

The decay channel $B^0 \to K^{*0}\tau\tau$ provides a large variety of final states. Since the reconstruction method requires the determination of the secondary vertex, only the charged decay $K^{*0}(892) \to K^-\pi^+$ will be considered. Furthermore, the knowledge of the tertiary vertices (tau decays locations) is as well required by the reconstruction method. This constraint imposes to consider at least the three-prongs decay of the τ lepton. The topology of this process is represented on Figure 3: there are three decay vertices, eight charged tracks in the final state and two undetected neutrinos.

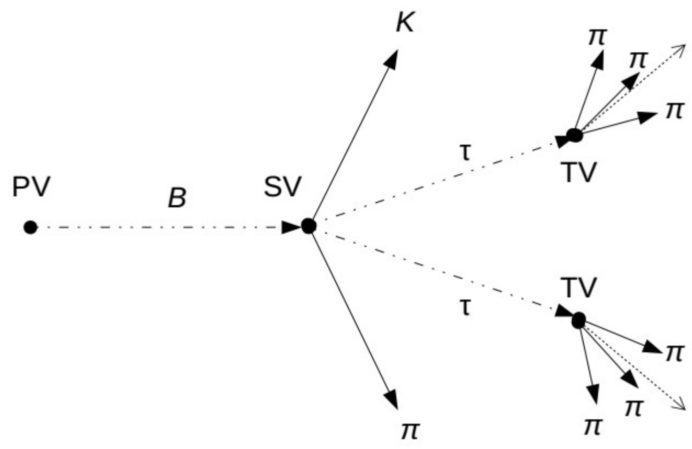

Figure 3: $B^0 \to K^{*0}\tau\tau$ topology with $K^{*0} \to K\pi$ and $\tau \to \pi\pi\pi\nu_\tau$.

3.2 Neutrinos reconstruction method

The section 3.1 highlighted that 2 out of the 10 final state particles of the decay mode of interest are not detected (and therefore not reconstructed in the data): these are the two neutrinos issued from the tertiary vertices of the τ decays (see Figure 3). A complete reconstruction of the B^0 candidates requires neutrinos momenta to be inferred from the properties of the reconstructed decays.

It will be shown that the knowledge of the flight vectors of the tau (accessible thanks to the knowledge of the production vertices of the K^* and of the systems of three π) together with the knowledge of the τ mass (measured with high precision at τ factories [20]) can be used to determine the missing coordinates.

The conservation of the energy-momentum at the tertiary vertex (valid for each of the two tertiary vertices) is first required:

$$\begin{cases} E_\tau = E_{\pi_t} + E_{\nu_\tau} \\ \vec{p_\tau} = \vec{p_{\pi_t}} + \vec{p_{\nu_\tau}} \end{cases} , \tag{3.1}$$

where π_t denotes the system of the three pions issued from the tau decay. The τ and ν_τ notations designate either the particle or the anti-particle (one equation comes with a single τ).

Introducing, with natural units:

$$E^2 = \vec{p}^2 + m^2$$

and assuming $E_\nu = p_\nu$ as in Standard Model:

$$\sqrt{m_\tau^2 + p_\tau^2} = \sqrt{m_{\pi_t}^2 + p_{\pi_t}^2} + p_{\nu_\tau}.$$

Squaring the expression

$$m_\tau^2 + p_\tau^2 = E_{\pi_t}^2 + p_{\nu_\tau}^2 + 2p_{\nu_\tau} E_{\pi_t},$$

and projecting the conservation of the momentum onto the tau flight direction:

$$p_\tau = p_{\pi_t}^{\parallel} + p_{\nu_\tau}^{\parallel} \ \& \ 0 = p_{\pi_t}^{\perp} + p_{\nu_\tau}^{\perp},$$

one can find this intermediate equation:

$$p_\tau^2 = p_{\pi_t}^{\parallel,2} + p_{\nu_\tau}^{\parallel,2} + 2p_{\pi_t}^{\parallel} \cdot p_{\nu_\tau}^{\parallel}.$$

Using

$$p^2 = p^{\perp,2} + p^{\parallel,2},$$

one can obtain:

$$m_\tau^2 = E_{\pi_t}^2 + \cancel{p_{\nu_\tau}^{\parallel,2}} + p_{\nu_\tau}^{\perp,2} + 2p_{\nu_\tau} E_{\pi_t} - p_{\pi_t}^{\parallel,2} - \cancel{p_{\nu_\tau}^{\parallel,2}} - 2p_{\pi_t}^{\parallel} \cdot p_{\nu_\tau}^{\parallel}.$$

Developing to determine the neutrino momentum

$$p_{\nu_\tau}^{\perp,2} = p_{\pi_t}^{\perp,2},$$

then:

$$m_\tau^2 - E_{\pi_t}^2 + p_{\pi_t}^{\parallel,2} - p_{\pi_t}^{\perp,2} = 2(p_{\nu_\tau} E_{\pi_t} - p_{\pi_t}^{\parallel} \cdot p_{\nu_\tau}^{\parallel}),$$

let's introduce an intermediary quantity denoted K as:

$$2K = m_\tau^2 - E_{\pi_t}^2 + p_{\pi_t}^{\parallel,2} - p_{\pi_t}^{\perp,2} = m_\tau^2 - m_{\pi_t}^2 - 2p_{\pi_t}^{\perp,2}.$$

One gets the following expressions :

$$K + p_{\pi_t}^{\parallel} \cdot p_{\nu_\tau}^{\parallel} = \sqrt{p_{\nu_\tau}^{\perp,2} + p_{\nu_\tau}^{\parallel,2}}\, E_{\pi_t}.$$

By squaring the two sides and put all on left, a second degree equation is obtained:

$$p_{\nu_\tau}^{\parallel,2}(p_{\pi_t}^{\parallel,2} - E_{\pi_t}^2) + p_{\nu_\tau}^{\parallel} 2K p_{\pi_t}^{\parallel} + (K^2 - p_{\pi_t}^{\perp,2} E_{\pi_t}^2) = 0,$$

with Δ expressed as

$$\begin{aligned}
&\Delta = 4[K^2 p_{\pi_t}^{\parallel,2} - (p_{\pi_t}^{\parallel,2} - E_{\pi_t}^2)(K^2 - p_{\pi_t}^{\perp,2} E_{\pi_t}^2)] \\
\Leftrightarrow\ &\Delta = 4E_{\pi_t}^2 (p_{\pi_t}^{\parallel,2} p_{\pi_t}^{\perp,2} + K^2 - p_{\pi_t}^{\perp,2} E_{\pi_t}^2) \\
\Leftrightarrow\ &\Delta = E_{\pi_t}^2 (m_\delta^2 - 4p_{\pi_t}^{\perp,2} m_\tau^2),
\end{aligned}$$

where:

$$m_\delta = m_\tau^2 - m_{\pi_t}^2.$$

The transverse invariant-mass of the three-pions system reads:

$$\begin{aligned} p_{\pi_t}^{\parallel,2} - E_{\pi_t}^2 &= -(m_{\pi_t}^2 + p_{\pi_t}^{\perp,2}) \\ 2Kp_{\pi_t}^{\parallel} &= (m_\delta - p_{\pi_t}^{\perp,2})p_{\pi_t}^{\parallel}. \end{aligned}$$

One eventually obtains the parallel component of the neutrino momentum:

$$p_{\nu_\tau}^{\parallel} = \frac{((m_\tau^2 - m_{\pi_t}^2) - 2p_{\pi_t}^{\perp,2})}{2(p_{\pi_t}^{\perp,2} + m_{\pi_t}^2)}.p_{\pi_t}^{\parallel} \pm \frac{\sqrt{(m_\tau^2 - m_{\pi_t}^2)^2 - 4m_\tau^2 p_{\pi_t}^{\perp,2}}}{2(p_{\pi_t}^{\perp,2} + m_{\pi_t}^2)}.E_{\pi_t}.$$

To summarize the computation the reconstructed momentum of the neutrino is given in equation 3.2:

$$\begin{cases} p_{\nu_\tau}^{\perp} = -p_{\pi_t}^{\perp} \\ p_{\nu_\tau}^{\parallel} = \dfrac{((m_\tau^2 - m_{\pi_t}^2) - 2p_{\pi_t}^{\perp,2})}{2(p_{\pi_t}^{\perp,2} + m_{\pi_t}^2)}.p_{\pi_t}^{\parallel} \pm \dfrac{\sqrt{(m_\tau^2 - m_{\pi_t}^2)^2 - 4m_\tau^2 p_{\pi_t}^{\perp,2}}}{2(p_{\pi_t}^{\perp,2} + m_{\pi_t}^2)}.E_{\pi_t}. \end{cases} \tag{3.2}$$

There is a straightforward result obtained for the transverse momentum of the neutrino since it is the opposite to the three-pions system transverse momentum. On the other hand, the longitudinal momentum is more involved and reveals a quadratic ambiguity.

The consequence of this quadratic ambiguity is that when reconstructing the neutrinos coming from a B^0 there are four possible solutions per B^0 candidate (namely, there are two solutions per neutrino and two neutrinos per B^0).

3.3 Selection rule

It has been proven aboveline that the neutrino reconstruction method leads to four different solutions for the mass of B^0, among which only one is correct ! A selection rule is desirable to choose the "true solution" and the properties of the decay are here also useful. By using the energy momentum conservation at B^0 decay vertex:

$$\begin{cases} E_B = E_{\tau^+} + E_{\tau^-} + E_{K^{*0}} \\ \vec{p}_B = \vec{p}_{\tau^+} + \vec{p}_{\tau^-} + \vec{p}_{K^*}, \end{cases}$$

one obtains:

$$p_{\tau^+}.\vec{e}_{\tau^+} = p_B.\vec{e}_B - p_{\tau^-}.\vec{e}_{\tau^-} - p_{K^*}.\vec{e}_{K^*},$$

where $\vec{e}_i$ (unitary flight vectors) denotes the unitary vector of the particle i direction. It is practical to single out the τ momentum by multiplying each side by $\vec{e}_{\tau^+}$:

$$p_{\tau^+} = p_B.(\vec{e}_B.\vec{e}_{\tau^+}) - p_{\tau^-}.(\vec{e}_{\tau^-}.\vec{e}_{\tau^+}) - p_{K^*}.(\vec{e}_{K^*}.\vec{e}_{\tau^+}). \tag{3.3}$$

On the other hand, the projection of the momentum equation onto the B^0 direction yields:

$$\begin{cases} 0 = p_{\tau^+}^{\perp} + p_{\tau^-}^{\perp} + p_{K^*}^{\perp} \\ p_B = p_{\tau^+}^{\parallel} + p_{\tau^-}^{\parallel} + p_{K^*}^{\parallel} \end{cases},$$

that one can rewrite explicitly for the parallel projection with scalar products :

$$p_B = p_{\tau^+}.(\vec{e}_B.\vec{e}_{\tau^+}) + p_{\tau^-}.(\vec{e}_B.\vec{e}_{\tau^-}) + p_{K^*}.(\vec{e}_B.\vec{e}_{K^*}). \tag{3.4}$$

Injecting 3.4 in 3.3 and isolating p_{τ^+}, one finds:

$$p_{\tau^+} = \frac{\vec{p}_{K^*}.[(\vec{e}_B.\vec{e}_{K^*}).(\vec{e}_B.\vec{e}_{\tau^+}) - (\vec{e}_{K^*}.\vec{e}_{\tau^+})]}{1-(\vec{e}_{\tau^+}.\vec{e}_B)^2} - p_{\tau^-}.\frac{\vec{e}_{\tau^+}.\vec{e}_{\tau^-} - (\vec{e}_{\tau^+}.\vec{e}_B)(\vec{e}_{\tau^-}.\vec{e}_B)}{1-(\vec{e}_{\tau^+}.\vec{e}_B)^2}.$$

An equivalent computation can be done by starting from p_{τ^-}. The energy-momentum conservation applied at the level of the B^0 decay eventually provides a relation between the momentum of the two τ and the K^* as explicited in equation 3.5:

$$p_{\tau^\pm} = -\frac{\vec{p}^{\perp}_{K^*}.\vec{e}_{\tau^\pm}}{1-(\vec{e}_{\tau_\pm}.\vec{e}_B)^2} - p_{\tau^\mp}.\frac{\vec{e}_{\tau^\pm}.\vec{e}_{\tau^\mp} - (\vec{e}_{\tau^\pm}.\vec{e}_B)(\vec{e}_{\tau_\mp}.\vec{e}_B)}{1-(\vec{e}_{\tau^\pm}.\vec{e}_B)^2}. \tag{3.5}$$

One τ momentum can be predicted from the other. It is therefore possible to choose the reconstructed τ^+/τ^- solution that minimizes the deviation between τ momenta predictions and reconstructions.

4 FCC-*ee*

4.1 The FCC-*ee* project

The Future Circular Collider (FCC) [21–23] is a particle collider project, currently in the phase of Feasibility Study, hosted by CERN. This new machine is expected to take over from the HL-LHC in the exploration of particle physics at the horizon of 2040. The collider project consists in two phases: an e^+e^- collider, with a center-of-mass energy span from 90 GeV to 360 GeV, crossing all the relevant electroweak thresholds; it shall be followed, using the same civil engineering infrastructure, by a *pp* collider at an energy in the center-of-mass at or above 100 TeV (against 13 TeV at the LHC). The footprint of the machine wiggles between France and Switzerland and the most recent implementation features a ring of around 91 km of circumference (tunnels of 4 m of diameter) placed 300 m underground as shown in Figure 4.

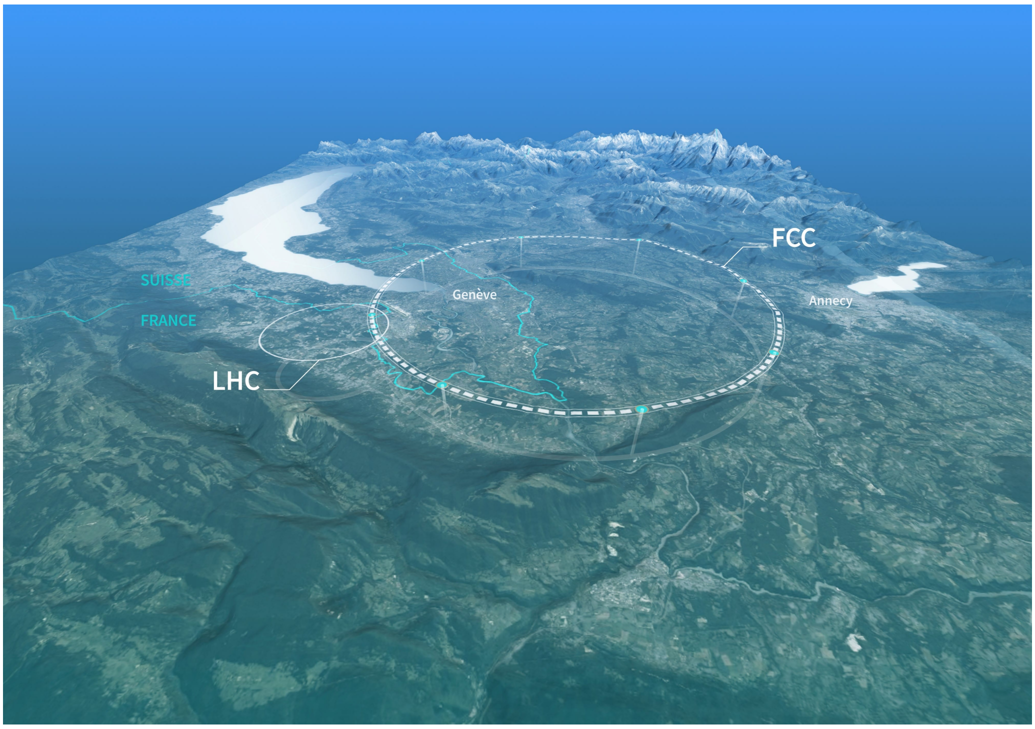

Figure 4: FCC footprint, 91km circular collider.

The LHC would serve as an injector for the FCC-pp, allowing to maximally benefit from the current CERN infrastructures. The work reported in this document focusses on the first phase of the FCC: FCC-*ee*.

The exquisite statistics which can be obtained at FCC-*ee* is best displayed in the luminosity plot in Figure 5, where several e^+e^- collider projects performance are superimposed. The current baseline of the FCC-*ee* design comprises 4 interaction points. Figure 6 summarises the center-of-mass operation scheme. In particular, the Z pole running, of interest for this work, will consist in four years of data taking and shall gather 6.10^{12} Z decays. The large partial width of the Z boson into $b\bar{b}$ pairs provides in turn about 740^9 B^0 mesons.

As previously underlined, FCC-*ee* combines the virtue of a clean experimental environment and the presence of boosted b-hadrons. It gathers the advantageous attributes of the current flavour physics collider facilities, SUPERKEB and LHC. The enormous, invincible cross-section obtained at LHC is to a certain extent mitigated by the exquisite luminosity expected at the Z pole.

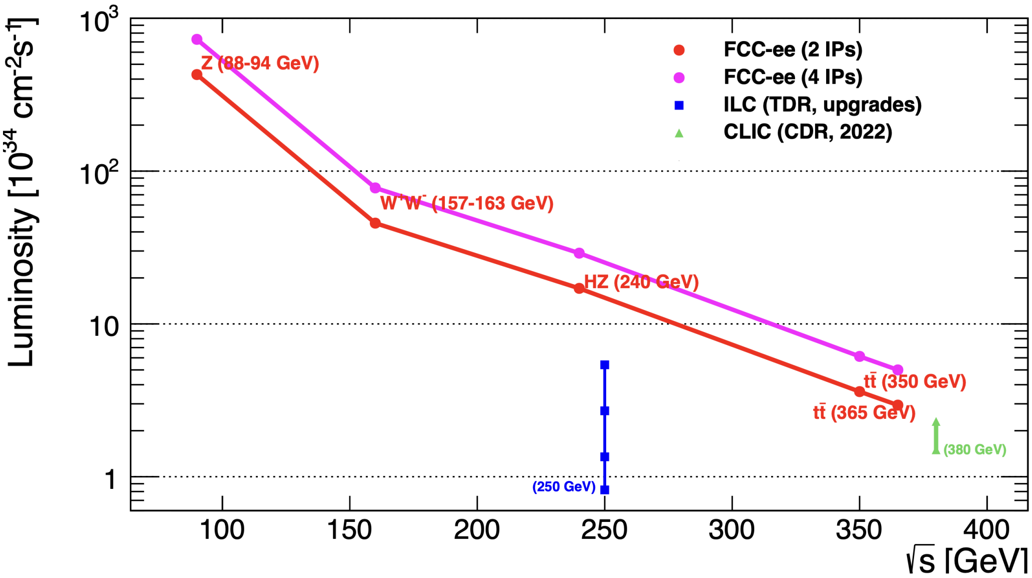

Figure 5: Comparison of e^+e^- collider luminosities.

Working point	Z, years 1-2	Z, later	WW, years 1-2	WW, later	ZH	$t\bar{t}$	
$\sqrt{s}$ (GeV)	88, 91, 94		157, 163		240	340–350	365
Lumi/IP ($10^{34}\,\mathrm{cm^{-2}s^{-1}}$)	70	140	10	20	5.0	0.75	1.20
Lumi/year ($\mathrm{ab^{-1}}$)	34	68	4.8	9.6	2.4	0.36	0.58
Run time (year)	2	2	2	0	3	1	4
Number of events	$6\,10^{12}$ Z		$2.4\,10^{8}$ WW		$1.45\,10^{6}$ HZ + 45k WW $\rightarrow$ H	$1.9\,10^{6}$ $t\bar{t}$ +330k HZ +80k WW $\rightarrow$ H	

Figure 6: Operation scheme in the current FCC-*ee* baseline.

4.2 The IDEA detector

Among the detector concepts at hand for FCC-*ee*, the IDEA concept [9,10] (Innovative Detector for Electron-positron Accelerators) is used in this work. This detector project comprises a high-granularity vertex detector with pixel read-out (as developed for the ALICE experiment [24]), an ultralight drift chamber (followed by an ultimate silicon layer), which complements the tracking system and potentially allows for hadron particle identification. A dual read-out calorimeter with several options completes the sub-detectors. An artist view of this detector concept is displayed in Figure 7.

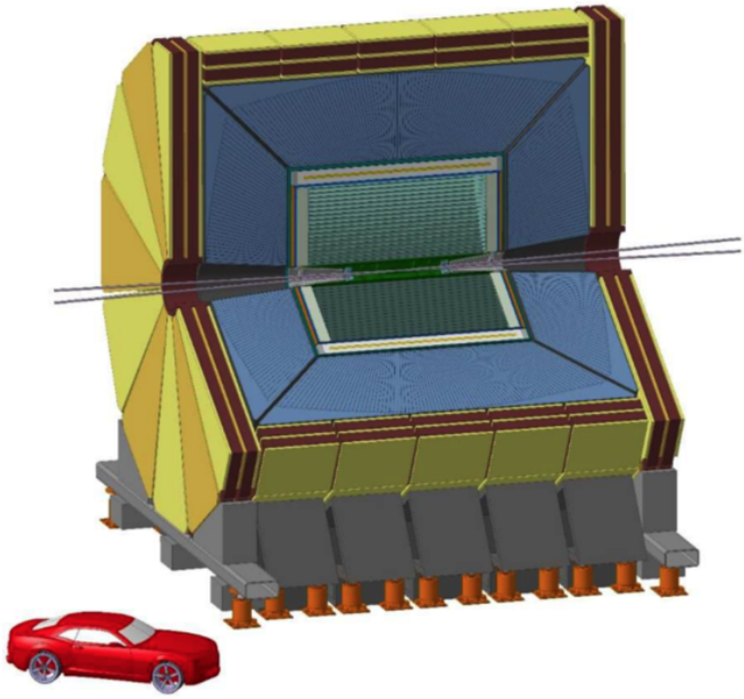

Figure 7: IDEA detector

The IDEA version used in this work is limited to the tracking system. The purpose of this work consists in assessing the necessary vertex detector performance to observe the decay $B^0 \to K^*\tau\tau$ at the SM value. The resolution on the decay vertex measurements will therefore be emulated (several performances are then tested) and compared to the actual IDEA working point (in its current design).

5 Reconstruction method

5.1 Software and data

Signal events used in this work are generated with Pythia [25] ($Z \to b\bar{b}$ and hadronisation) and EvtGen [26] (to force the decay with adequate models) through exclusive samples (all the simulated events are $B^0 \to K^{*0}\tau\tau$ with $K^{*0} \to K^+\pi^-$ and $\tau \to \pi\pi\pi\nu_\tau$ events).The reconstruction is performed with the FCCAnalyses software using Delphes [8] simulation (featuring the IDEA detector) and the winter2023 production version. The simulated data use particles reconstructed with the momentum resolution given by the IDEA tracking system [9, 10], *i.e.* the vertex detector complemented by the drift chamber. The decay files used to simulate the signal samples can be found on the winter2023 branch of the official FCC-config github project following the path FCCee/Generator/EvtGen/Bd2KstarTauTau.dec, the corresponding generated files are available at : /eos/experiment/fcc/ee/generation/DelphesEvents/winter2023/IDEA/p8_ee_Zbb_ecm91_EvtGen_Bd2KstarTauTau.

An analyzer, as the usual FCCAnalyses tool to produce tuples ready for analysis from the simulated datas, has been built to make the analysis level tuples. The analysis level tuples contain various informations:

- MC-Truth kinematics of the particles (momentum, energy, decay vertex position),
- MC-truth PID-PDG index of the particles,
- MC-truth informations concerning the genealogy of the events,
- MC-truth primary vertex of the events,
- reconstructed simulated kinematics of the final particles,
- association tags between MC-truth and reconstructed simulated particles.

The analysis of these tuples is based on the Python computing language with Uproot [27] and Awkward Array [28] libraries.

5.2 The $B^0 \to K^{*0}\tau\tau$ signal candidates

The first step of the analysis is to select the $B^0 \to K^{*0}\tau\tau$ candidates from the final state particles of each event. Pions and kaons are selected from the reconstructed particles (reconstructed through the fast-simulated detector) via their MC-truth PID number in order to limit the multiplicity of the upcoming candidates.

The $K^{*0}(892)$ candidates are made from combinations of opposite charges $\pi - K$. They are selected if their reconstructed invariant-mass is found within $0.1\,\mathrm{GeV/c^2}$ around the K^{*0} PDG [20] mass. Note that the natural width of $K^{*0}(892)$ is about 50 MeV. A perfect seeding of the candidates is performed to limit the multiplicity. Its effect will be embodied in the final selection efficiency determination.

The τ candidates are built by combining three charged π which yield to a +1 or -1 electric charge. Candidates are selected when the reconstructed mass falls in the $[3m_\pi, m_\tau]$ range corresponding to the possible mass of the τ built from only 3π due to missing neutrinos. Again, a perfect seeding on the pions is applied to limit combinatorics.The event candidate is retained if two oppositely charged τ candidates are found. Individual τ candidates must not share final state pions.

The B^0 candidates are eventually formed by combininging the K^{*0} and the two τ candidates (τ and K^{*0} candidates shall not share final state particles nor a common vertex. The reconstructed mass of the combination must be found below the B^0 PDG [20] mass because of the two undetected neutrinos that take part of the decay kinematics (e.g. it is expected to have a candidate mass that is below the B^0 PDG [20] mass).

In fact, a final particle of the decay can be missed by the simulated detector, or the resolution of the detector on the measured kinematics of the final particles (which are used to build invariant mass) can lead to the cut of an event which was generated at MC-Truth level. These two reasons explain why not all the events have a $B^0 \to K^{*0}\tau\tau$ candidate. From the simulated signal samples, the efficiency to have $B^0 \to K^{*0}\tau\tau$ candidate for an event is measured to be 77% for the signal samples (given by the number of candidates obtained divided by the number of generated events). This somehow low reconstruction efficiency can be understood because of the high multiplicity of the decay and the low momenta of the final state particles: the tracking efficiency is worst at low momentum.

The kinematics of the K^{*0} and τ candidates are also computed and saved for the next steps of the analysis.

5.3 Neutrino reconstruction and selection rule

To reconstruct the missing neutrinos, the flight vectors of the B^0 and τ's candidates are build (both in a MC-truth version for verification purposes and a reconstructed version for analysis; see below) and used in equation 3.2 which yields two solutions of reconstructed neutrinos for each τ. The neutrino reconstructed kinematics is propagated to the τ candidates with the determination of $p_{\tau^+_+}, p_{\tau^+_-}, p_{\tau^-_+}$ and $p_{\tau^-_-}$ where the upper sign denotes the charge of the considered τ and the lower sign denotes the solution taken to reconstruct neutrinos in equation 3.2. The τ reconstruction is propagated to B^0 kinematics, which leads to four solutions for each B^0 candidate.

The correct B^0 candidate can be identified thanks to the selection rule, described in section 3.3. It provides a prediction for the τ momentum : $p^{pred}_{\tau^+_+}, p^{pred}_{\tau^+_-}, p^{pred}_{\tau^-_+}$ and $p^{pred}_{\tau^-_-}$, where the upper sign denotes the charge of the considered τ and the lower sign denotes the other τ solution that has been used in equation 3.5. All the differences between the reconstructed and predicted τ momentum are then built (4 per charge):

- $p_{\tau^+_-} - p^{pred}_{\tau^+_-}$, $p_{\tau^+_-} - p^{pred}_{\tau^+_+}$, $p_{\tau^+_+} - p^{pred}_{\tau^+_-}$, $p_{\tau^+_+} - p^{pred}_{\tau^+_+}$,
- $p_{\tau^-_-} - p^{pred}_{\tau^-_-}$, $p_{\tau^-_-} - p^{pred}_{\tau^-_+}$, $p_{\tau^-_+} - p^{pred}_{\tau^-_-}$, $p_{\tau^-_+} - p^{pred}_{\tau^-_+}$.

The τ reconstruction best solutions (e.g. the lower sign of the two momentum of each difference corresponds to a $\pm$ solution of the two τ reconstruction) are selected by taking the ones that correspond to the smallest difference. It should be noted that the selection efficiency of this rule is 100 % in case of infinite resolution.

Due to the presence of a square root in equation 3.2, the neutrino reconstruction could lead to unphysical solutions due to momentum resolutions or due to rounding precision. On the other hand, the selection rule can, for the same reason, lead to consider a wrong solution combination. The neutrino reconstruction method efficiency (an event is lost when at least one neutrino leads to a wrong value) and the purity of the selection rule are evaluated by checking respectively the number of events that pass the neutrino reconstruction and by determining at MC-Truth level the right sign of the τ candidates.

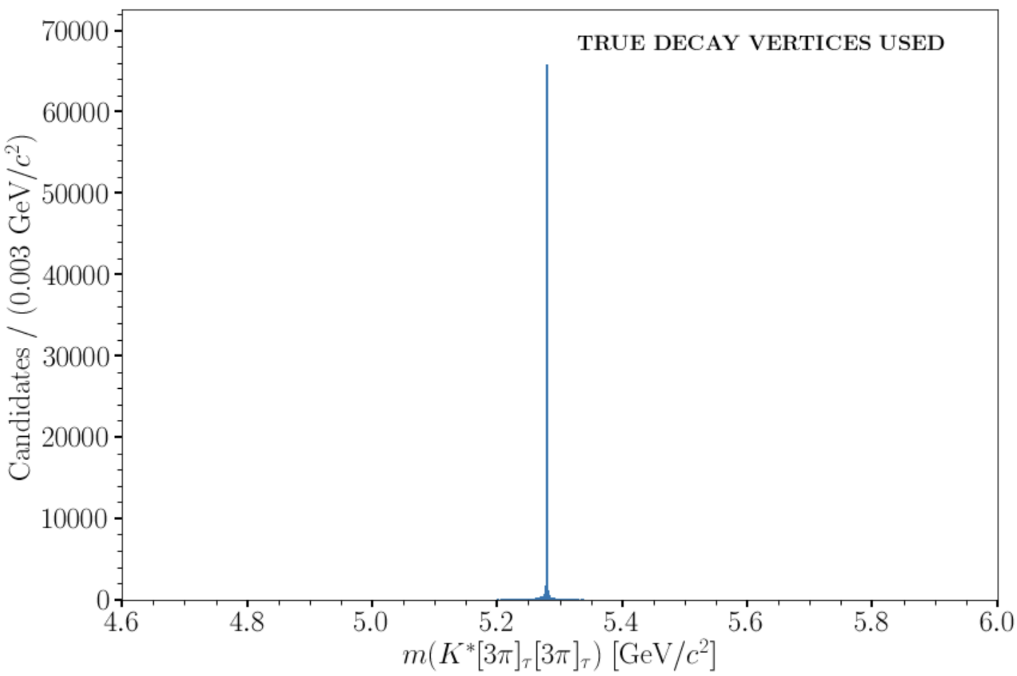

Figure 8: The B^0 invariant-mass reconstructed (100000 events file) with the neutrino reconstruction method and the selection rule from the MC-Truth kinematics of the final state particles. A Dirac-like peak is observed at the PDG B^0 invariant mass, validating the method and its implementation.

5.4 Signal reconstruction result

5.4.1 MC reconstruction

For verification purposes, the method explained in this section has been first applied to the $B^0 \to K^{*0}\tau\tau$ candidates by using the MC-Truth kinematics of the final state particles. The correct solution shall be found for each candidate. Yet, the precision rounding of the flat tuples kinematic variables induced a small inefficiency. The neutrino reconstruction efficiency is about 99% and the selection rule purity is about 98%. These high values, together with the invariant-mass distribution of the B^0 reconstructed in Figure 8, are enough to confirm the consistency of the method.

5.4.2 Vertices performance emulation

The main goal of this study is to determine the vertex detector requirements in order to measure $B^0 \to K^{*0}\tau\tau$ at the SM value. The vertexing performances are varied and therefore emulated for the reconstructed $B^0 \to K^{*0}\tau\tau$ candidates in this first phase of the study. The primary vertex has been smeared once for all from its MC-Truth position with numbers close to the 3D resolutions determined in the Cartesian coordinates from the determinations done in Section 9.1 , *e.g.* 3 µm on x and z coordinates, 0.0238 µm on y coordinate. This includes the beam spot luminous region constraints. As far as the secondary and tertiary vertices are concerned, regarding the fact that decaying particles are boosted along one direction for each event, it has been decided to perform a 2D ellipsoidal Gaussian smearing with longitudinal directions aligned onto the decaying particle directions and transverse directions picked-up randomly in the corresponding orthogonal plan (via the association of a random angle in the orthogonal plan and a random displacement). The Figure 9 illustrates the smearing of the vertices.

The SV and TV position reconstruction are the main drivers of the topological reconstruction performances. Several SV and TV smearing configurations are used in term of

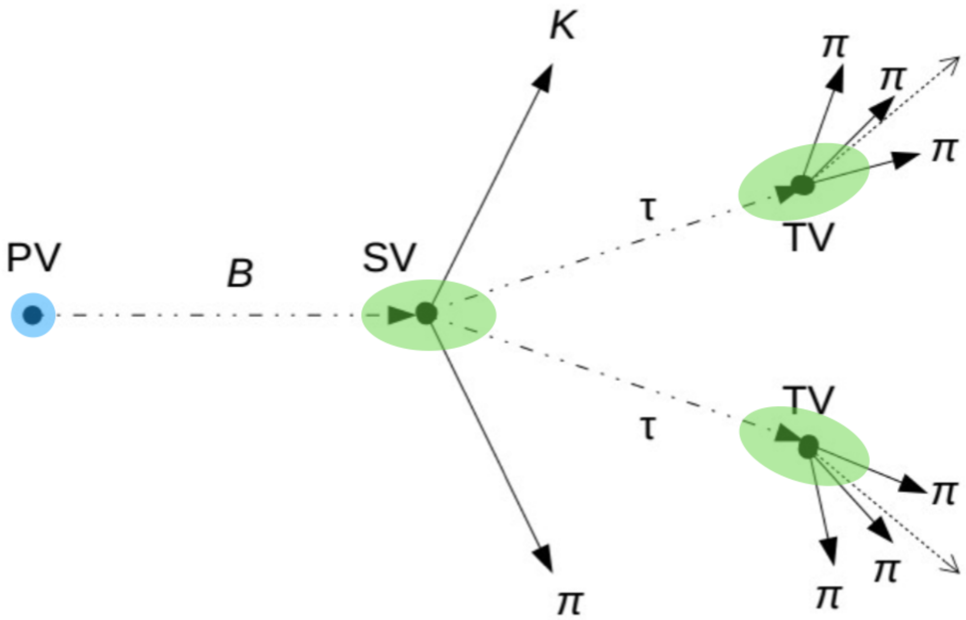

Figure 9: Illustration of the smearing applied to the vertices in order to emulate the vertex detector performances, blue circle denotes the 3D smearing of the PV and green ellipses denote the ellipsoidal smearing of SV and TV.

Longitudinal-Transverse (L-T) Gaussian standard deviation. For SV and TV smearing, three longitudinal resolutions are used: 5 µm, 10 µm, 20 µm, and eight transverse resolutions:1 µm, 2 µm, 3 µm, 4 µm, 5 µm, 6 µm, 7 µm, 8 µm. Most of the figures in the next sections consider the $20-3$µm ellipsoidal smearing for SV and TV as a reference.

This emulation does not take into account any vertexing efficiency. We arbitrarily but conservatively set it to 80% in the derivation of the selection efficiency at the stage of the signal and background yields estimations.

5.4.3 Simulated data reconstruction

The method is finally applied to $B^0 \to K^{*0}\tau\tau$ candidate by using the reconstructed kinematics of the final state particles for the vertexing working points previously defined. On the reference vertexing configuration of $20-3$µm, selection rule purity is about 50% (still better than 25% which corresponds to a random choice) and the total reconstruction efficiency is about 38% (77% of B^0 candidates building and $\sim 50\%$ of neutrinos reconstruction). The Figure 10 shows the invariant-mass distributions obtained with the reference vertexing working point.

5.5 Expected yields of signal at FCC-*ee*

Thanks to the determination of the signal efficiency obtained with the IDEA detector and the vertex detector performance corresponding to the reference working point, it is possible to determine the expected number of selected signal events corresponding to this detector at FCC-*ee*. Equation 5.1 shows the formula to determine this number of events:

$$\mathcal{N}_{K^*\tau\tau\to K7\pi2\nu} = \mathcal{N}_Z \cdot BF(Z \to b\bar{b}) \cdot 2f_d \cdot BF(K^*\tau\tau) \cdot BF(\tau \to \pi\pi\pi\nu)^2 . BF(K^* \to K\pi) \cdot \epsilon_{\text{reco}} . \epsilon_{\text{vertex}}, \quad (5.1)$$

where $\mathcal{N}_Z = 6 \times 10^{12}$ the expected number of Z produced w.r.t. FCC-*ee* baseline, $BF(Z \to b\bar{b}) = 0.1512 \pm 0.0005$ [20], $f_d = 0.407 \pm 0.007$ is the hadronisation fraction corresponding to

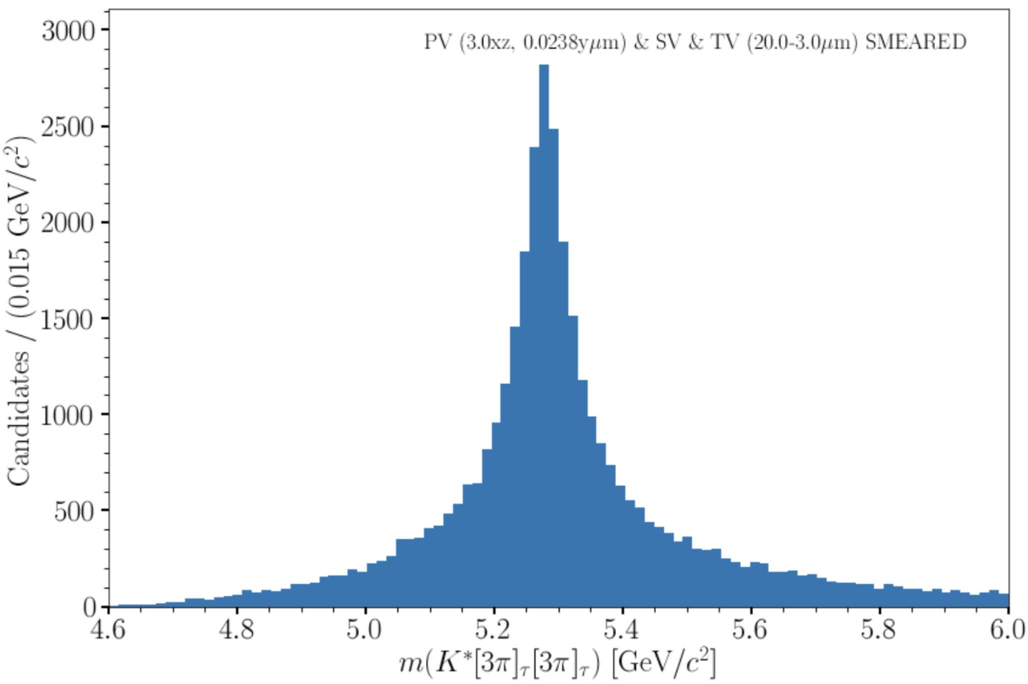

Figure 10: Reconstructed B^0 candidate invariant-mass(100000 events file) with the neutrinos reconstruction method and the selection rule from the reconstructed (by the simulated detector) kinematics of the final state particles on the simulated signal samples.

$b \to B_d^0$ [29], $BF(K^*\tau\tau) = 1.30 \times 10^{-7} \pm 10\%$ the SM predicted branching fraction [1], $BR(\tau \to \pi\pi\pi\nu) = 0.0931 \pm 0.0005$ [20], $BR(K^* \to K\pi) = 0.69$ [20] (the PDG $BR(K^* \to K\pi) \simeq 1$ is composed of $0.31(K_S^0\pi^0) + 0.69(K^+\pi^-)$), $\epsilon_{reco} = 0.3840 \pm 0.0007$ is the total reconstruction efficiency determined for a $3\,\mu\text{m} - 20\,\mu\text{m}$ smearing, and $\epsilon_{vertex} = 0.8$ is the assumed vertex reconstruction efficiency.

Assuming the SM and the baseline FCC-ee luminosity, one eventually would select $\mathcal{N}_{\mathcal{K}^*\tau\tau\to\mathcal{K}\pi\in\nu} = \infty\imath\not\pm\infty\forall$. The identification of the background sources and their evaluation will play a major role in the examination of the feasibility of the measurement.

6 Backgrounds

6.1 Identification

The potential sources of background to consider are those providing a similar final state as the signal one (one kaon and seven pions); they must be of physical origin and can occur from $b \to c\bar{c}s$ and $b \to c\tau\nu_\tau$ transitions. Among the $b \to c\bar{c}s$ modes, the decays involving a $D_s^{(*)}$ in the final state like $B^0 \to K^{*0} D_s^{(*)} D_s^{(*)}$ are potentially dominant since the D_s decays can provide either a real τ particle or three-prongs mimicking a *tau*: $D_s \to \tau\nu$, $D_s \to 3\pi\pi^0$ and $D_s \to 3\pi 2\pi^0$. For $b \to c\tau\nu_\tau$ modes like $B_s^0 \to K^{*0} D^{(*)} \tau\nu$ with $D \to 3\pi\pi^0$ and/or $D^* \to D\pi^0$ or $D^* \to D^0\pi$ with $D^0 \to 4\pi\pi^0$, and $B^0 \to K^{*0} D_s^{(*)} \tau\nu$ with the aforementioned D_s decays can also mimic the signal. There modes are not measured to date and their branching fractions must be guesstimated, as detailed in the next Section 6.2.

6.2 BF determination

6.2.1 $B^0 \to K^{*0} D_s^{(*)} D_s^{(*)}$

LHC*b* [12] performed recently the first measurement of the branching fraction of the decay mode $B^+ \to K^+ D_s^+ D_s^-$ [30]:

$$BF(B^+ \to K^+ D_s^+ D_s^-) = (1.15 \pm 0.39) \times 10^{-4}. \tag{6.1}$$

This decay proceeds through the same amplitudes as the background source of interest in this work $B^0 \to K^{*0} D_s D_s$. The only difference is carried by the spectator quark (u for B^+ and d for B^0) and this similarity makes this measurement a good proxy for $BF(B^0 \to K^{*0} D_s D_s)$. Yet, a corrective factor that takes into account the difference in the form factors ($B^+ \to K^+$ vs $B^0 \to K^{*0}$ transitions) and another that accounts for the phase space difference are needed.

The form factor correction is inferred from measured modes with equivalent amplitudes, one with a K, the other with a K^*: it is directly taken as the ratio of their branching fractions. The PDG [20] provides the measurements of $B^+ \to D^0 K^+$ and $B^+ \to D^0 K^{*+}$ branching fractions, which match the aforementioned requirement. The measurements give $BF(B^+ \to D^0 K^+) = (3.64 \pm 0.15) \times 10^{-4}$ and $BF(B^+ \to D^0 K^{*+}) = (5.3 \pm 0.4) \times 10^{-4}$. The form factor correction is determined in equation 6.2:

$$C_{\mathrm{FF}} = \frac{\mathrm{FF}_{\mathrm{K}^*}}{\mathrm{FF}_{\mathrm{K}}} = \frac{BF(B^+ \to D^0 K^{*+})}{BF(B^+ \to D^0 K^+)} = 1.46 \pm 0.13, \tag{6.2}$$

where the uncertainty comes from the standard propagation of the BF uncertainties without correlations .

The phase space correction is accordingly determined by comparing two equivalent modes one with a K, the other with a K^*, and then build their ratio. Starting from $B^+ \to K^+ D_s^+ D_s^-$, the corresponding mode is $B^+ \to K^{*+} D_s^+ D_s^-$. The phase spaces of the two modes have been computed numerically by 2D integrations in the Dalitz Plane [31] of the decays (the Dalitz Plane is a common representation of the three-body decay phase space) and provides $PS(B^+ \to K^+ D_s^+ D_s^-) = 1.076 \times 10^{-7}$ and $PS(B^+ \to K^{*+} D_s^+ D_s^-) = 3.507 \times 10^{-8}$. The phase space correction is determined in equation 6.3:

$$C_{\mathrm{PS}} = \frac{PS(B^+ \to K^{*+} D_s^+ D_s^-)}{PS(B^+ \to K^+ D_s^+ D_s^-)} = 0.326, \tag{6.3}$$

where no uncertainty is considered from the computation.

The $B^0 \to K^{*0} D_s D_s$ branching fraction is computed from the $B^+ \to K^+ D_s^+ D_s^-$ measurement and the corrective factors by merging together equations 6.1, 6.2 and 6.3 to obtain the result in equation 6.4:

$$BF(B^0 \to K^{*0} D_s D_s) = BF(B^+ \to K^+ D_s^+ D_s^-) \times C_{\mathrm{FF}} \times C_{\mathrm{PS}} = (5.47 \pm 1.92) \times 10^{-5}, \quad (6.4)$$

where uncertainty comes from the propagation of the previous uncertainties.

To determine $BF(B^0 \to K^{*0} D_s^* D_s)$ and $BF(B^0 \to K^{*0} D_s^* D_s^*)$, the form factor hierarchy between the $D_s D_s$, $D_s^* D_s$ and $D_s^* D_s^*$ final states is needed. One way to determine this hierarchy is to consider the branching fractions of measured modes that involved two $D_s^{(*)}$. The $B_s^0 \to D_s^{(*)} D_s^{(*)}$ [20] match this requirement. The needed branching fractions are given in equations 6.5, 6.6 and 6.7:

$$BF(B_s^0 \to D_s D_s) = (4.4 \pm 0.5) \times 10^{-3}, \quad (6.5)$$
$$BF(B_s^0 \to D_s^* D_s) = (1.39 \pm 0.17) \times 10^{-2}, \quad (6.6)$$
$$BF(B_s^0 \to D_s^* D_s^*) = (1.44 \pm 0.21) \times 10^{-2}. \quad (6.7)$$

The branching fractions given in equations 6.5, 6.6 and 6.7 are added to determine the inclusive $BF(B_s^0 \to D_s^{(*)} D_s^{(*)})$ and with equation 6.4 divided by the $B_s^0 \to D_s D_s$ branching fraction it allow the determination of the inclusive $B^0 \to K^{*0} D_s^{(*)} D_s^{(*)}$ branching fraction in equation 6.8:

$$BF(B^0 \to K^{*0} D_s^{(*)} D_s^{(*)}) = BF(B^0 \to K^{*0} D_s D_s) \times \frac{BF(B_s^0 \to D_s^{(*)} D_s^{(*)})}{BF(B_s^0 \to D_s D_s)} = (4.07 \pm 1.54) \times 10^{-4}, \quad (6.8)$$

where the uncertainty is determined by propagating all the intermediate branching fractions uncertainties.

The branching fraction of $B^0 \to K^{*0} D_s^* D_s$ is estimated, by considering the inclusive $BF(B^0 \to K^{*0} D_s^{(*)} D_s^{(*)})$ and following the hierarchy given by $B_s^0 \to D_s^{(*)} D_s^{(*)}$, as written in equation 6.9:

$$BF(B^0 \to K^{*0} D_s^* D_s) = BF(B^0 \to K^{*0} D_s^{(*)} D_s^{(*)}) \times \frac{BF(B_s^0 \to D_s^* D_s)}{BF(B_s^0 \to D_s^{(*)} D_s^{(*)})} = (1.73 \pm 0.70) \times 10^{-4}. \quad (6.9)$$

Similarly the branching fraction of $B^0 \to K^{*0} D_s^* D_s^*$ is estimated by considering the inclusive $BF(B^0 \to K^{*0} D_s^{(*)} D_s^{(*)})$ and following the hierarchy given by $B_s^0 \to D_s^{(*)} D_s^{(*)}$, as written in equation 6.10:

$$BF(B^0 \to K^{*0} D_s^* D_s^*) = BF(B^0 \to K^{*0} D_s^{(*)} D_s^{(*)}) \times \frac{BF(B_s^0 \to D_s^* D_s^*)}{BF(B_s^0 \to D_s^{(*)} D_s^{(*)})} = (1.79 \pm 0.72) \times 10^{-4}. \quad (6.10)$$

6.2.2 $B^0 \to K^{*0} D_s^{(*)} \tau\nu$

To determine the inclusive branching fraction of $B^0 \to K^{*0} D_s^{(*)} \tau\nu$ a strategy of analogy is used [32] considering the mode $B^+ \to K^+ D_s^{(*)} \mu\nu$ as reference with $BF(B^+ \to K^+ D_s^{(*)} \mu\nu) = (6.1 \pm 1.0) \times 10^{-4}$ [20]. The $BF(B^0 \to K^{*0} D_s^{(*)} \tau\nu)$ can be estimated from $BF(B^+ \to K^+ D_s^{(*)} \mu\nu)$ by correcting for the suppression effects ($s\bar{s}$ and τ) using a phase space ratio. The inclusive branching fraction of $B^0 \to K^{*0} D_s^{(*)} \tau\nu$ is given in equation 6.11:

$$BF(B^0 \to K^{*0} D_s^{(*)} \tau\nu) = BF(B^+ \to K^+ D_s^{(*)} \mu\nu) \times \frac{PS(B^0 \to K^{*0} D_s^{(*)} \tau\nu)}{PS(B^+ \to K^+ D_s^{(*)} \mu\nu)} = (2.95 \pm 0.48) \times 10^{-5}, \quad (6.11)$$

where $PS(B^0 \to K^{*0} D_s^{(*)} \tau\nu) = 3.1 \times 10^{-8}$ and $PS(B^+ \to K^+ D_s^{(*)} \mu\nu) = 6.4 \times 10^{-7}$ are computed via numerical pseudo 3-body phase space integration by considering the dominant $K - D$ hadronic resonances [32]. The uncertainty comes from $BF(B^+ \to K^+ D_s^{(*)} \mu\nu)$.

The $B^0 \to K^{*0} D_s \tau\nu$ and $B^0 \to K^{*0} D_s^* \tau\nu$ branching fraction are then accessed from $BF(B^0 \to K^{*0} D_s^{(*)} \tau\nu)$ following the hierarchy of the $B^0 \to D^* \ell\nu_\ell$ modes, measured to be $BF(B^0 \to D\ell\nu_\ell) = (2.24 \pm 0.09) \times 10^{-2}$ and $BF(B^0 \to D^* \ell\nu_\ell) = (4.97 \pm 0.12) \times 10^{-2}$. The branching fractions $B^0 \to K^{*0} D_s \tau\nu$ and $B^0 \to K^{*0} D_s^* \tau\nu$ are therefore

$$BF(B^0 \to K^{*0} D_s \tau\nu) = BF(B^0 \to K^{*0} D_s^{(*)} \tau\nu) \times \frac{BF(B^0 \to D\ell\nu_\ell)}{BF(B^0 \to D^{(*)}\ell\nu_\ell)} = (9.17 \pm 1.56) \times 10^{-6}, \tag{6.12}$$

$$BF(B^0 \to K^{*0} D_s^* \tau\nu) = BF(B^0 \to K^{*0} D_s^{(*)} \tau\nu) \times \frac{BF(B^0 \to D^*\ell\nu_\ell)}{BF(B^0 \to D^{(*)}\ell\nu_\ell)} = (2.03 \pm 0.34) \times 10^{-5}, \tag{6.13}$$

where uncertainties comes from the propagation of the intermediate branching fractions uncertainties.

6.2.3 $B_s^0 \to K^{*0} D^{(*)} \tau\nu$

To determine the inclusive branching fraction of $B_s^0 \to K^{*0} D^{(*)} \tau\nu$ a strategy of analogy is used [32] considering the mode $B_s^0 \to D_{s1}(2536)^- \mu\nu$ as a reference with $BF(B_s^0 \to D_{s1}(2536)^- \mu\nu) = (2.7 \pm 0.7) \times 10^{-3}$ [20]. The $BF(B_s^0 \to K^{*0} D^{(*)} \tau\nu)$ can be estimated from $BF(B_s^0 \to D_{s1}(2536)^- \mu\nu)$ with the method developed in Section 6.2.2. With respect to the method, the inclusive branching fraction of $B_s^0 \to K^{*0} D^{(*)} \tau\nu$ is given in equation 6.14:

$$BF(B_s^0 \to K^{*0} D^{(*)} \tau\nu) = BF(B_s^0 \to D_{s1}(2536)^- \mu\nu) \times \frac{PS(B_s^0 \to K^{*0} D^{(*)} \tau\nu)}{PS(B_s^0 \to D_{s1}(2536)^- \mu\nu)} = (2.34 \pm 0.61) \times 10^{-4}, \tag{6.14}$$

where $PS(B_s^0 \to K^{*0} D^{(*)} \tau\nu) = 5.7 \times 10^{-8}$ and $PS(B_s^0 \to D_{s1}(2536)^- \mu\nu) = 6.6 \times 10^{-7}$ are computed via numerical phase space integration considered as pseudo 3-body [32]. The uncertainty comes from $BF(B_s^0 \to D_{s1}(2536)^- \mu\nu)$.

The $B_s^0 \to K^{*0} D \tau\nu$ and $B_s^0 \to K^{*0} D^* \tau\nu$ branching fractions are accessed following the method developed in Section 6.2.2. The $B_s^0 \to K^{*0} D \tau\nu$ and $B_s^0 \to K^{*0} D_s^* \tau\nu$ branching fractions are summarised in equations 6.15 and 6.16:

$$BF(B_s^0 \to K^{*0} D \tau\nu) = BF(B_s^0 \to K^{*0} D^{(*)} \tau\nu) \times \frac{BF(B^0 \to D\ell\nu_\ell)}{BF(B^0 \to D^{(*)}\ell\nu_\ell)} = (7.27 \pm 1.92) \times 10^{-5}, \tag{6.15}$$

$$BF(B_s^0 \to K^{*0} D^* \tau\nu) = BF(B_s^0 \to K^{*0} D^{(*)} \tau\nu) \times \frac{BF(B^0 \to D^*\ell\nu_\ell)}{BF(B^0 \to D^{(*)}\ell\nu_\ell)} = (1.61 \pm 0.42) \times 10^{-4}, \tag{6.16}$$

where uncertainties comes from the propagation of the considered intermediate branching fractions uncertainties.

6.3 Visible BF determination

The visible branching fractions of the possible backgrounds are computed following equation 6.17:

$$BF(X \to y) = BF(Z^0 \to b\bar{b}) \times 2 \times f_X \times BF(X \to x) \times BF(x \to y), \tag{6.17}$$

where $BF(Z^0 \to b\bar{b}) = (15.12 \pm 0.05) \times 10^{-2}$ [20], the factor 2 takes into account the charge conjugated process, X denotes the b-hadron considered, x denotes the decay product of the b-hadron, y denotes the final state, f_X is the hadronisation fraction of the $b \to X$, taken from

HFLAV measurements [29], $BF(X \to x)$ comes from section 6.2 and $BF(x \to y)$ is the product of the intermediate BF to obtain the final state [20].

Here, it is important to notice that the intermediate branching fractions $BF(D_s \to 3\pi\pi^0)$ and $BF(D_s \to 3\pi 2\pi^0)$ require to consider their intermediate η and ω contributions. Equations 6.18 and 6.19 are detailing the numbers considered:

$$\begin{aligned} BF(D_s \to 3\pi\pi^0) &= BF(D_s \to \eta\pi) \times BF(\eta \to 2\pi\pi^0) + BF(D_s \to \omega\pi) \times BF(\omega \to 2\pi\pi^0) \\ BF(D_s \to 3\pi\pi^0) &= (5.58 \pm 0.34) \times 10^{-3}, \end{aligned} \tag{6.18}$$

$$\begin{aligned} BF(D_s \to 3\pi 2\pi^0) &= BF(D_s \to \eta\pi\pi^0) \times BF(\eta \to 2\pi\pi^0) + BF(D_s \to \omega\pi\pi^0) \times BF(\omega \to 2\pi\pi^0) \\ BF(D_s \to 3\pi 2\pi^0) &= (4.68 \pm 0.64) \times 10^{-2}, \end{aligned} \tag{6.19}$$

where the branching fractions values are taken from [20].

Table 1 summarises the branching fractions of the possible modes and in addition provides the list of the additional missing particles for each of them.

6.4 Backgrounds to consider

The possible interesting backgrounds have been presented and their branching fractions are estimated. It is now needed to choose the backgrounds to consider.

Regarding the $b \to c\tau\nu$ backgrounds, they are problematic since D and most prominently D_s mesons can decay leptonically to a τ particle or mimic a hadronic final state close to the signal. In term of lifetime D_s is closer to τ than D, which provides a further advantage to the D_s backgrounds in the reconstruction method. Furthermore, $D_s \to 3\pi 2\pi^0$ is ten times more likely compared to $D \to 3\pi 2\pi^0$. Finally, D_s seems to be a more suitable candidate to mimic a signal τ compared to D, leading to the exclusion of B_s^0 backgrounds for which the simultaneous production of a $D_s K^*(892)$ pair is disfavoured.

In order to choose in an educated way, the backgrounds to consider in the remaining ones, having a look at the branching fractions only, is not enough. The reconstruction efficiency (mostly related to phase space specifics of the background decays) will modulate the toxicity of the backgrounds depending on their abilities to survive the reconstruction method and their abilities to produce invariant masses close to the B^0 invariant mass. To address these effects, simulations of unique background types have been done: $B^0 \to K^{*0} D_s \tau\nu$ with $D_s \to \tau\nu$, $B^0 \to K^{*0} D_s D_s$ with $D_s \to \tau\nu$ and $D_s \to 3\pi\pi^0$ and $D_s \to 3\pi 2\pi^0$ and $D_s \to \tau\nu/3\pi\pi^0$, $B^0 \to K^{*0} D_s^* D_s$ with $D_s \to \tau\nu$. The goal in the following is to build a per-track efficiency to apply to the visible branching fraction to rank and choose the backgrounds to consider.

Each of the background has been used through the reconstruction workflow, with the reference vertexing performances configuration, in order to extract the reconstruction efficiency (which are the product of the efficiency to find a B^0 candidate and the efficiency to pass the neutrinos reconstruction) and the window efficiency which is the efficiency to be in the B^0 mass window $[5.0, 5.6]$GeV. A total per mode efficiency is then constructed with the product of the two previously defined efficiencies, the results are summarised in table 2.

A per track efficiency is then constructed for each D_s taking the square root of the two D_s modes, assuming a uniform repartition of the K^{*0} tracks in the two D_s track efficiencies. The per track efficiencies are written in equations 6.20, 6.21 and 6.22:

$$\epsilon(D_s \to \tau\nu) = \sqrt{\epsilon(B^0 \to K^{*0} D_s D_s, D_s \to \tau\nu)} = \sqrt{0.101}, \tag{6.20}$$

$$\epsilon(D_s \to 3\pi\pi^0) = \sqrt{\epsilon(B^0 \to K^{*0} D_s D_s, D_s \to 3\pi\pi^0)} = \sqrt{0.005}, \tag{6.21}$$

$$\epsilon(D_s \to 3\pi 2\pi^0) = \sqrt{\epsilon(B^0 \to K^{*0} D_s D_s, D_s \to 3\pi 2\pi^0)} = \sqrt{0.191}. \tag{6.22}$$

Decay	BF (SM/meas.)	Intermediate decay	BF_{had}	Additional missing particles
Signal: $B^0 \to K^{*0}\tau\tau$	$1.30\times\ 10^{-7}$	$\tau \to \pi\pi\pi\nu$, $K^{*0} \to K\pi$	$9.57\times\ 10^{-11}$	
$b \to c\bar{c}s$ bkgs:				
$B^0 \to K^{*0}D_sD_s$	$5.47\times\ 10^{-5}$	$D_s \to \tau\nu$	$1.14\times\ 10^{-10}$	2ν
		$D_s \to \pi\pi\pi\pi^0$	1.45×10^{-10}	$2\pi^0$
		$D_s \to \pi\pi\pi2\pi^0$	1.02×10^{-8}	$4\pi^0$
		$D_s \to \tau\nu, \pi\pi\pi\pi^0$	1.28×10^{-10}	ν , π^0
		$D_s \to \tau\nu, \pi\pi\pi2\pi^0$	1.08×10^{-9}	ν , $2\pi^0$
		$D_s \to \pi\pi\pi\pi^0, \pi\pi\pi2\pi^0$	1.21×10^{-9}	$3\pi^0$
$B^0 \to K^{*0}D_sD_s^*$	1.73×10^{-4}	$D_s \to \tau\nu$	3.60×10^{-10}	2ν, γ/π^0
		$D_s \to \pi\pi\pi\pi^0$	4.57×10^{-10}	$2\pi^0$, γ/π^0
		$D_s \to \pi\pi\pi\pi^0\pi^0$	3.22×10^{-8}	$4\pi^0$, γ/π^0
		$D_s \to \tau\nu, \pi\pi\pi\pi^0$	4.06×10^{-10}	ν , π^0, γ/π^0
		$D_s \to \tau\nu, \pi\pi\pi2\pi^0$	3.41×10^{-9}	ν , $2\pi^0$, γ/π^0
		$D_s \to \pi\pi\pi\pi^0, \pi\pi\pi2\pi^0$	3.84×10^{-9}	$3\pi^0$, γ/π^0
$B^0 \to K^{*0}D_s^*D_s^*$	$1.79\times\ 10^{-4}$	$D_s \to \tau\nu$	3.73×10^{-10}	2ν, $2\gamma/\pi^0$
		$D_s \to \pi\pi\pi\pi^0$	4.73×10^{-10}	$2\pi^0$, $2\gamma/\pi^0$
		$D_s \to \pi\pi\pi\pi^0\pi^0$	3.33×10^{-8}	$4\pi^0$, $2\gamma/\pi^0$
		$D_s \to \tau\nu, \pi\pi\pi\pi^0$	4.20×10^{-10}	ν , π^0, $2\gamma/\pi^0$
		$D_s \to \tau\nu, \pi\pi\pi2\pi^0$	3.52×10^{-9}	ν , $2\pi^0$, $2\gamma/\pi^0$
		$D_s \to \pi\pi\pi\pi^0, \pi\pi\pi2\pi^0$	3.97×10^{-9}	$3\pi^0$, $2\gamma/\pi^0$
$b \to c\tau\nu$ bkgs:				
$B_s \to K^{*0}D\tau\nu$	$7.27\times\ 10^{-5}$	$D \to \pi\pi\pi\pi^0$	1.65×10^{-9}	ν, π^0
$B_s \to K^{*0}D^*\tau\nu$	$1.61\times\ 10^{-4}$	$D^* \to\ D^0\pi, D\pi^0$		
		$D \to \pi\pi\pi\pi^0$	$1.12\times\ 10^{-9}$	ν, $2\pi^0$
		$D^0 \to 2\pi2\pi\pi^0$	8.98×10^{-10}	ν, $2\pi^0$, $\pi^{\pm}$
$B^0 \to K^{*0}D_s\tau\nu$	$9.17\times\ 10^{-6}$	$D_s \to \tau\nu$	$3.59\times\ 10^{-10}$	2ν
		$D_s \to \pi\pi\pi\pi^0$	$4.05\times\ 10^{-10}$	ν, π^0
		$D_s \to \pi\pi\pi2\pi^0$	$3.39\times\ 10^{-9}$	ν, $2\pi^0$
$B^0 \to K^{*0}D_s^*\tau\nu$	$2.03\times\ 10^{-5}$	$D_s \to \tau\nu$	$7.95\times\ 10^{-10}$	2ν, γ/π^0
		$D_s \to \pi\pi\pi\pi^0$	$8.96\times\ 10^{-10}$	ν, π^0, γ/π^0
		$D_s \to \pi\pi\pi\pi^0\pi^0$	$7.51\times\ 10^{-9}$	ν, $\gamma/\pi^0, 2\pi^0$

Table 1: Summary table of the possible backgrounds (bkgs), τ decay not specified means $\tau \to \pi\pi\pi\nu$.

Mode	Reconstruction efficiency	Window efficiency	Total efficiency
Signal: $B^0 \to K^{*0}\tau\tau$	0.384	0.810	0.311
$B^0 \to K^{*0}D_sD_s, D_s \to \tau\nu$	0.475	0.213	0.101
$B^0 \to K^{*0}D_sD_s, D_s \to 3\pi\pi^0$	0.022	0.235	0.005
$B^0 \to K^{*0}D_sD_s, D_s \to 3\pi2\pi^0$	0.563	0.338	0.191
$B^0 \to K^{*0}D_sD_s, D_s \to \tau\nu/3\pi\pi^0$	0.101	0.222	0.023
$B^0 \to K^{*0}D_s^*D_s, D_s \to \tau\nu$	0.483	0.127	0.061
$B^0 \to K^{*0}D_s\tau\nu, D_s \to \tau\nu$	0.428	0.259	0.111

Table 2: Efficiency tables of the simulated modes.

To check the correctness of the method the agreement of $\epsilon(B^0 \to K^{*0} D_s D_s, D_s \to \tau\nu/3\pi\pi^0)$ with the product of the corresponding per track efficiencies is computed in equation 6.23:

$$\epsilon(D_s \to \tau\nu) \times \epsilon(D_s \to 3\pi\pi^0) = 0.022, \tag{6.23}$$

which is the same as the efficiency measured with the simulated sample, but the last digit due to rounding done in the computation.

In addition an efficiency to have a D_s^* in place of a D_s is computed thanks to $\epsilon(B^0 \to K^{*0} D_s^* D_s, D_s \to \tau\nu)$ and $\epsilon(D_s \to \tau\nu)$ in equation 6.24:

$$\epsilon(*) = \frac{\epsilon(D_s^* \to \tau\nu)}{\epsilon(D_s \to \tau\nu)} = \sqrt{0.365}, \tag{6.24}$$

where $\epsilon(D_s^* \to \tau\nu) = \epsilon(B^0 \to K^{*0} D_s^* D_s, D_s \to \tau\nu)/\epsilon(D_s \to \tau\nu)$.

The predicted efficiency is then built for all the modes from these per-track efficiencies. The check about $D_s \to \tau\nu/3\pi\pi^0$ shows that the predicted efficiency seems coherent for the $b \to c\bar{c}s$ backgrounds. On the other hand, the method is less adapted to the $b \to c\tau\nu_\tau$ in B^0 backgrounds, because of the presence of only one D_s, for them only one track efficiency is taken. For $b \to c\tau\nu_\tau$ in B_s backgrounds that have been excluded elsewhere before, the highest predicted efficiency on other $b \to c\tau\nu_\tau$ backgrounds is taken conservatively. The table of the branching fractions times predicted efficiency is displayed in table 3 where the modes are ranked thanks to the multiplication of the visible branching fraction by the predicted efficiency.

Mode	$\mathrm{BF_{had}}$ (10^{-8})	$\varepsilon_{\mathrm{pred}}$	$\mathrm{BF_{had}} \times \varepsilon_{\mathrm{pred}}$ (10^{-9})
$B_d^0 \to K^{*0} D_s^* D_s (D_s \to 3\pi 2\pi^0)$	3.22	0.115393	3.71
$B_d^0 \to K^{*0} D_s^* D_s^* (D_s \to 3\pi 2\pi^0)$	3.33	0.069715	2.32
$B_d^0 \to K^{*0} D_s^* \tau\nu (D_s \to 3\pi 2\pi^0)$	0.751	0.264036	1.98
$B_d^0 \to K^{*0} D_s D_s (D_s \to 3\pi 2\pi^0)$	1.02	0.191000	1.94
$B_d^0 \to K^{*0} D_s \tau\nu (D_s \to 3\pi 2\pi^0)$	0.339	0.437035	1.48
$B_s^0 \to K^{*0} D \tau\nu (D \to 3\pi\pi^0)$	0.165	0.437035	0.72
$B_s^0 \to K^{*0} D^* \tau\nu (D^* \to D\pi^0, D \to 3\pi\pi^0)$	0.112	0.437035	0.49
$B_s^0 \to K^{*0} D^* \tau\nu (D^* \to D^0\pi, D^0 \to 4\pi\pi^0)$	0.090	0.437035	0.39
$B_d^0 \to K^{*0} D_s^* D_s (D_s \to \tau\nu/3\pi 2\pi^0)$	0.341	0.083912	0.29
$B_d^0 \to K^{*0} D_s^* D_s^* (D_s \to \tau\nu/3\pi 2\pi^0)$	0.352	0.050696	0.18
$B_d^0 \to K^{*0} D_s^* \tau\nu (D_s \to \tau\nu)$	0.080	0.192003	0.15
$B_d^0 \to K^{*0} D_s D_s (D_s \to \tau\nu/3\pi 2\pi^0)$	0.108	0.138892	0.15
$B_d^0 \to K^{*0} D_s \tau\nu (D_s \to \tau\nu)$	0.036	0.317805	0.11
$B_d^0 \to K^{*0} D_s^* D_s (D_s \to 3\pi\pi^0/3\pi 2\pi^0)$	0.384	0.018670	0.07
$B_d^0 \to K^{*0} D_s^* D_s^* (D_s \to 3\pi\pi^0/3\pi 2\pi^0)$	0.397	0.011280	0.04
$B_d^0 \to K^{*0} D_s^* \tau\nu (D_s \to 3\pi\pi^0)$	0.090	0.042720	0.04
$B_d^0 \to K^{*0} D_s D_s (D_s \to 3\pi\pi^0/3\pi 2\pi^0)$	0.121	0.030903	0.04
Signal	0.010	0.313000	0.03
$B_d^0 \to K^{*0} D_s \tau\nu (D_s \to 3\pi\pi^0)$	0.041	0.070711	0.03
$B_d^0 \to K^{*0} D_s^* D_s (D_s \to \tau\nu)$	0.036	0.061019	0.02
$B_d^0 \to K^{*0} D_s^* D_s^* (D_s \to \tau\nu)$	0.037	0.036865	0.01
$B_d^0 \to K^{*0} D_s D_s (D_s \to \tau\nu)$	0.011	0.101000	0.01
$B_d^0 \to K^{*0} D_s^* D_s (D_s \to \tau\nu/3\pi\pi^0)$	0.041	0.013577	0.006
$B_d^0 \to K^{*0} D_s^* D_s^* (D_s \to \tau\nu/3\pi\pi^0)$	0.042	0.008202	0.003
$B_d^0 \to K^{*0} D_s D_s (D_s \to \tau\nu/3\pi\pi^0)$	0.013	0.022472	0.003
$B_d^0 \to K^{*0} D_s^* D_s (D_s \to 3\pi\pi^0)$	0.046	0.003021	0.001
$B_d^0 \to K^{*0} D_s^* D_s^* (D_s \to 3\pi\pi^0)$	0.047	0.001825	0.0009
$B_d^0 \to K^{*0} D_s D_s (D_s \to 3\pi\pi^0)$	0.015	0.005000	0.0007

Table 3: Table of the modes ranked as function of the visible branching fraction time predicted efficiency.

To keep the bookkeeping of the simulation at a reasonable rate, it has been chosen to simulate the dominant backgrounds in each category to drive the selection ideas. If a non-simulated background is found to be significant after the selection process, it will be re-examined. Namely, $B^0 \to K^{*0} D_s^* D_s$ and $B^0 \to K^{*0} D_s D_s$ with $D_s \to 3\pi 2\pi^0$ have been simulated, considering backgrounds with and without a D_s^* (implying fewer additional missing particles) and having the highest branching fractions (BF). In addition, $B^0 \to K^{*0} D_s D_s$ with $D_s \to 3\pi 2\pi^0/\tau\nu$ represents the dominant crossed mode without D_s^*, while $B^0 \to K^{*0} D_s D_s$ with $D_s \to 3\pi\pi^0/\tau\nu$ is the most irreducible crossed mode, they are both simulated. Moreover, $B^0 \to K^{*0} D_s^* D_s$ and $B^0 \to K^{*0} D_s D_s$ with $D_s \to \tau\nu$ are simulated as the most irreducible $b \to c\bar{c}s$ modes with and without D_s^*. Additionally, $B^0 \to K^{*0} D_s D_s$ with $D_s \to 3\pi\pi^0$ was already simulated. Finally, for the $b \to c\tau\nu$ backgrounds, $B^0 \to K^{*0} D_s^* \tau\nu$ with $D_s \to 3\pi 2\pi^0$ and $B^0 \to K^{*0} D_s \tau\nu$ with $D_s \to \tau\nu$ are simulated as respectively the dominant and the most irreducible backgrounds of this category.

6.5 Backgrounds generation

The backgrounds defined in Section 6.4 have all been simulated in order to be used in the analysis. The $D_s \to 3\pi n\pi^0$ backgrounds (where $n = 1, 2$) have been generated following the specific intermediate modes by which they are composed, as explained in Section 6.3. The next section details the selection criteria used to reduce the background modes.

The decay files used to generate all the modes of the analysis can be found on the winter2023 branch of the official FCC-config github project following the paths (the corresponding generated root files are available following the path in eos as the one given in section 5.1):

- FCCee/Generator/EvtGen/Bd2KstarTauTau.dec,
- FCCee/Generator/EvtGen/Bd2DsDsKstarDs2Taunu.dec,
- FCCee/Generator/EvtGen/Bd2DsDsKstarDs2TaunuDs2pipipipi0pi0.dec and FCCee/Generator/EvtGen/Bd2DsDsKstarDs2TaunuDs2pipipipi0pi0ChargeConjugation.dec,
- FCCee/Generator/EvtGen/Bd2DsDsKstarDs2TaunuDs2pipipipi0v2.dec and FCCee/Generator/EvtGen/Bd2DsDsKstarDs2TaunuDs2pipipipi0v2ChargeConjugation.dec,
- FCCee/Generator/EvtGen/Bd2DsDsKstarDs2pipipipi0pi0v2.dec,
- FCCee/Generator/EvtGen/Bd2DsDsKstarDs2pipipipi0v2.dec,
- FCCee/Generator/EvtGen/Bd2DsKstarTauNuDs2TauNu.dec,
- FCCee/Generator/EvtGen/Bd2DsstarDsKstarDs2PiPiPiPi0Pi0Dsstar2Dsgamma.dec,
- FCCee/Generator/EvtGen/Bd2DsstarDsKstarDs2TaunuDsstar2Dsgamma.dec,
- FCCee/Generator/EvtGen/Bd2DsstarKstarTauNuDs2pipipipi0pi0.dec.

7 Selection

7.1 Events weighting

The selection is constructed using datasets of simulated signal and background events, appropriately scaled to reproduce their natural proportion given in the Table of visible branching fractions 1. All modes are scaled w.r.t. their associated BF and reconstruction efficiencies in addition to the expected number of Z produced at FCC-ee $N_Z = 6e^{12}$ in order to consider the natural number of events. Finally, as the vertexing is emulated in the analysis, there is no actual vertexing reconstruction efficiency estimation available (ability of the detector to rightly associate tracks). A flat vertexing efficiency $\epsilon_{vertexing} = 0.8$ is therefore conservatively taken [1].

7.2 Selection rule behaviour on the backgrounds

The selection rule developed in Section 3.3 is the only educated way at hand to determine which B^0 signal solution is to be kept. To evaluate the selection rule behaviour on all the modes considered, the invariant-mass distribution of the reference vertexing configuration has been built for both a case where the four possible B^0 solutions are taken for each event and a case where only the selected solution is taken. The distributions of each mode are displayed in Figure 11, w.r.t. to their expected number of events in the $[4.6, 6]$GeV window, their respective branching fractions and the reconstruction efficiencies as determined in the simulation.

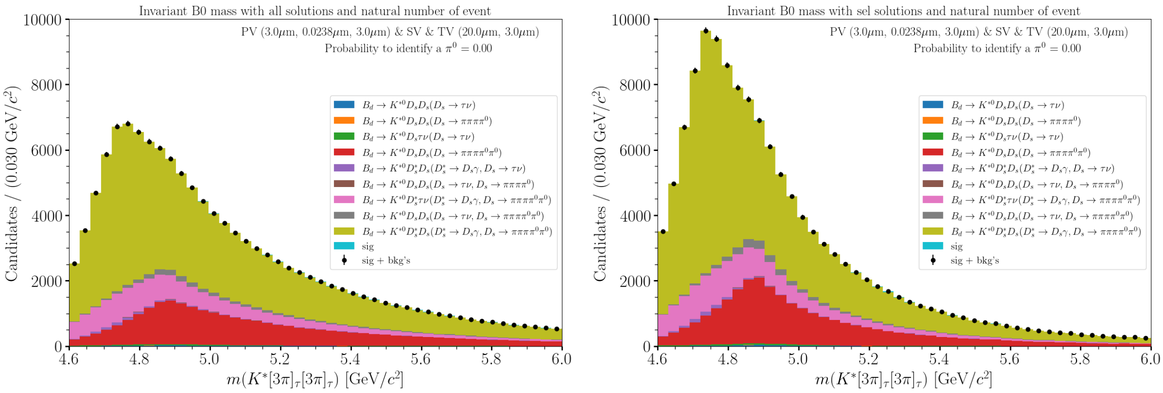

Figure 11: Invariant-mass plot of the B^0 candidates with the $20 - 3$µm vertexing resolution configuration for all solutions (left) and selected solutions (right).

The Figure 11 shows that the selection rule selects preferentially the low invariant-mass solutions, even for the backgrounds for which the average reconstructed mass are below m_{B^0} due to additional missing particles w.r.t. the signal. This behaviour promotes the selection rule as a prominent tool against the backgrounds. From a quantitative point of view, the signal purity can be used as a figure of merit:

$$P = \frac{S}{S+B}, \tag{7.1}$$

where S denotes the signal yield and B denotes the backgrounds yield. The purity observed for the reference vertexing configuration in the $[5.2, 5.6]$GeV/c^2 reduced window around the B^0 mass is twice larger with the selected solutions. In the following, the solutions selected by the selection rule are therefore always taken.

[1]this is supported by studies conducted after this work and in companion studies [33]

Mode	Total reconstruction efficiency (%)
Signal	38.40 ± 0.07
$B^0 \to K^{*0} D_s D_s, D_s \to \tau\nu$	47.49 ± 0.04
$B^0 \to K^{*0} D_s D_s, D_s \to 3\pi\pi^0$	2.190 ± 0.002
$B^0 \to K^{*0} D_s D_s, D_s \to 3\pi 2\pi^0$	56.30 ± 0.05
$B^0 \to K^{*0} D_s D_s, D_s \to \tau\nu/3\pi\pi^0$	10.14 ± 0.01
$B^0 \to K^{*0} D_s D_s, D_s \to \tau\nu/3\pi 2\pi^0$	51.64 ± 0.04
$B^0 \to K^{*0} D_s^* D_s, D_s \to \tau\nu$	48.27 ± 0.04
$B^0 \to K^{*0} D_s^* D_s, D_s \to 3\pi 2\pi^0$	57.30 ± 0.04
$B^0 \to K^{*0} D_s \tau\nu, D_s \to \tau\nu$	42.85 ± 0.04
$B^0 \to K^{*0} D_s^* \tau\nu, D_s \to 3\pi 2\pi^0$	47.26 ± 0.04

Table 4: Summary table of the total reconstruction (including the B^0 candidate building and neutrino reconstruction) efficiency as function of the mode for the reference vertexing performances working point.

The total reconstruction efficiencies are summarised, for each mode with the reference vertexing resolution configuration, in table 4. Several of the backgrounds show better reconstruction efficiencies than the signal; this, together with their branching fraction, justify their apparent toxicities on Figure 11.

7.3 Calorimeter performance impact

A significant part of the dominant backgrounds come with additional π^0 from $D_s \to 3\pi n\pi^0$ ($n = 1, 2$). This type of background is reducible provided that the pi^0 particles can be reconstructed in the calorimeter. Their association with tracks to form a mother particle candidate can be therefore further used to select the signal. The calorimeter performance is parameterised for the sake of simplicity with the sole global π^0 reconstruction efficiency denoted ϵ_{π^0}.

The $D_s \to 3\pi n\pi^0$ decays proceed through the η/ω intermediate state. It is therefore enough to identify only η/ω to reject one of these backgrounds. The surviving probabilities associated to these backgrounds are then:

$$p_{1D_s} = 1 - \epsilon_{\pi^0}, \tag{7.2}$$
$$p_{2D_s} = (1 - \epsilon_{\pi^0})^2, \tag{7.3}$$

where the surviving probability to the calorimeter is defined for both, backgrounds with one $D_s \to 3\pi n\pi^0$ and backgrounds with two $D_s \to 3\pi n\pi^0$ as function of the calorimeter performances.

The ALEPH calorimeter performance showed a π^0 reconstruction efficiency of about 50 % [34]. It is therefore reasonable to consider that electromagnetic calorimeter designs for FCC-*ee*, especially if they are meeting Flavour Physics and *CP* violation physics requirements would reach 80 %. The application of these calorimeter performances in the analysis clearly improves the picture on the invariant-mass plot for the reference vertexing configuration as displayed in Figure 12. A signal purity in the range $[5.2, 5.6]\mathrm{GeV/c^2}$ of 0.102 is obtained. Yet, a further selection is in order and is described in hte next subsection.

7.4 XGBoost selection

Among the possible selection methods, it has been decided to use an XGBoost [35] algorithm, which is a multivariate classifier (MVA) often used in HEP. This section will explain the XG-

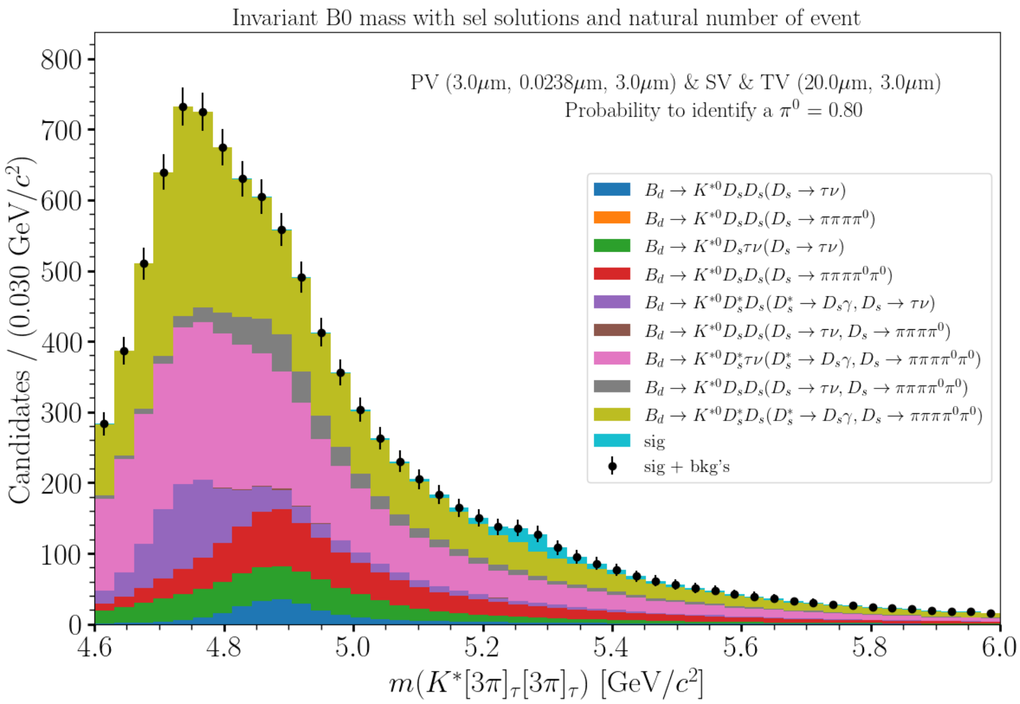

Figure 12: Invariant-mass plot of the B^0 candidates with the $20 - 3\mu$m vertexing resolution configuration after the use of the π^0 reconstruction to reduce the $D_s \to 3\pi n\pi^0$ background.

Boost selection built for the analyses from, first, the identification of the potential discriminative variables, second, a preselection step, and third, the XGBoost itself.

7.4.1 Discriminative variables

In order to build the selection several quantities have been saved in parallel of the analysis workflow, the most relevant to discriminate background from signal are named discriminative variables and those are the ones to use in the selection. The discriminative variables are identified from the comparison of their signal and background distributions, the discriminative variables (all displayed in natural units with c=1) found in the analysis are:

- the reconstructed momentum of the K^{*0} candidate, exhibiting differences because of the phase space of the decay. It is displayed in Figure 13,
- the reconstructed momentum combination of the 3π from τ candidates displayed in Figure 14,
- the highest measured π momentum from τ candidates, characteristic of the τ decay dynamics, proceeding dominantly from a $a_1(1260)$ intermediate amplitude as displayed in Figure 15,
- the lowest measured π momentum from τ candidates based on the properties of the $a_1 \to \rho\pi$ decay (valid for the two latter quantities).It is displayed in Figure 16,
- the determined B^0 candidate flight distance displayed in Figure 17,
- the determined τ candidate flight distance displayed in Figure 18,
- the determined distances between primary and tertiary vertices displayed in Figure 19,
- the reconstructed mass of the 3π from τ candidate displayed in Figure 20,

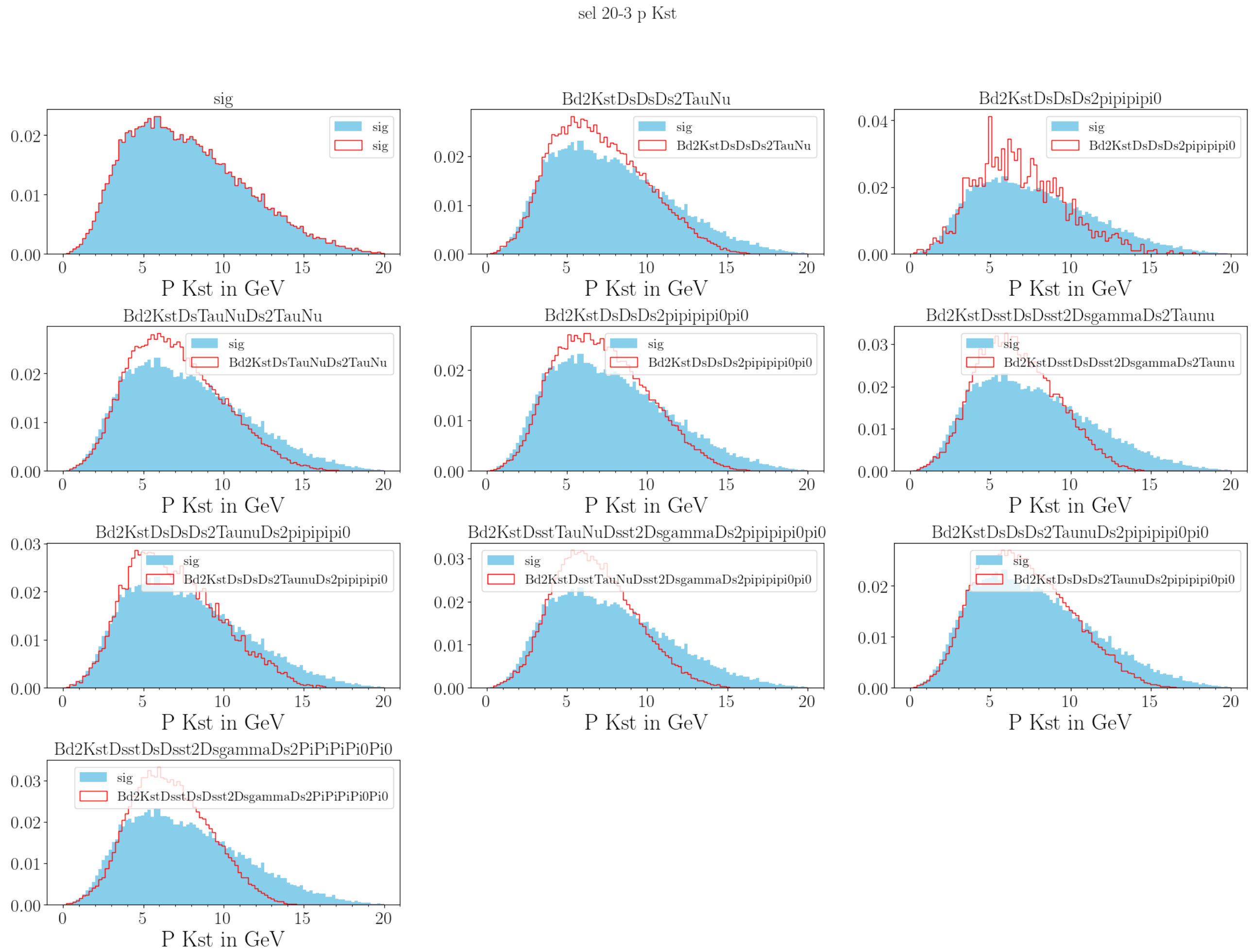

Figure 13: $p_{K^{*0}}$ candidates distribution as function of the mode.

- the reconstructed highest 2π combination mass from τ candidate displayed in Figure 21,
- the reconstructed lowest 2π combination mass from τ candidate displayed in Figure 22,
- the reconstructed τ candidate momentum that take into account the ν reconstruction displayed in Figure 23.

Finally, the Dalitz plane defined by the reconstructed highest 2π combination squared mass and the reconstructed lowest 2π combination squared mass is a powerful tool to remove the dominant backgrounds as displayed in Figure24.

7.4.2 Preselection

The basic discriminative variables identified in section 7.4.1 are first used in a preselection stage in order to reduce, with simple/sanity cuts, the dominant backgrounds. The table 5 summarises the cuts used in the preselection. Sanity cuts are applied on $p_{K^{*0}}$, $p_{\pi\,max}$ and $p_{\pi\,min}$. Initial cuts are applied on $p_{3\pi}$ and FD_{B^0} to remove backgrounds without a significant loss of signal events. Cuts are applied on $m_{3\pi}$, $m_{2\pi\,max}$, $m_{2\pi\,min}$ and the Dalitz $m_{2\pi}$ plan to reduce especially the $D_s \to 3\pi n\pi^0$ backgrounds. Eventually, a requirement is applied on FD_τ to reduce specifically the $D_s \to \tau\nu$ backgrounds.

Figure 25 shows the invariant-mass distribution of the B^0 candidates after the preselection. By comparing the figures 12 and 25 one can see a clear improvement of the signal purity by

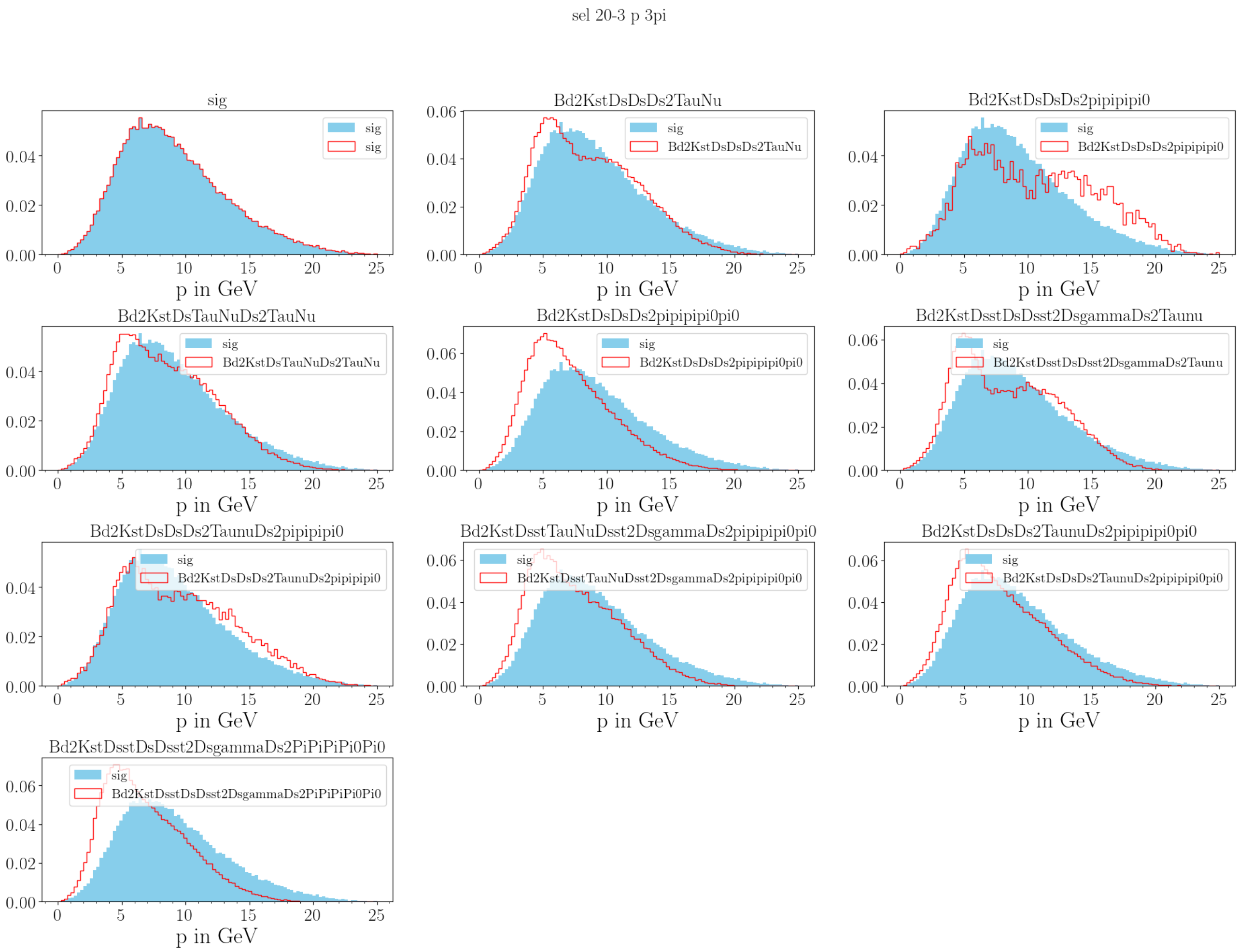

Figure 14: $p_{3\pi}$ from τ candidates distribution as function of the mode.

Variable	Cut
$m^2_{2\pi_{min}}$ & $m^2_{2\pi_{max}}$	< 0.3 & < 0.5 GeV^2/c^4
p_{K^*}	$<$ 1GeV/c
$p_{3\pi}$	$<$ 1GeV/c
$p_{\pi_{max}}$	$<$ 0.25GeV/c
$p_{\pi_{min}}$	$<$ 0.2GeV/c
FD_B	$<$ 0.3mm
FD_τ	$>$ 4mm
$m_{3\pi}$	$<$ 0.750GeV/c^2
$m_{2\pi_{max}}$	$<$ 0.5GeV/c^2
$m_{2\pi_{min}}$	$>$ 1GeV/c^2

Table 5: Preselection table

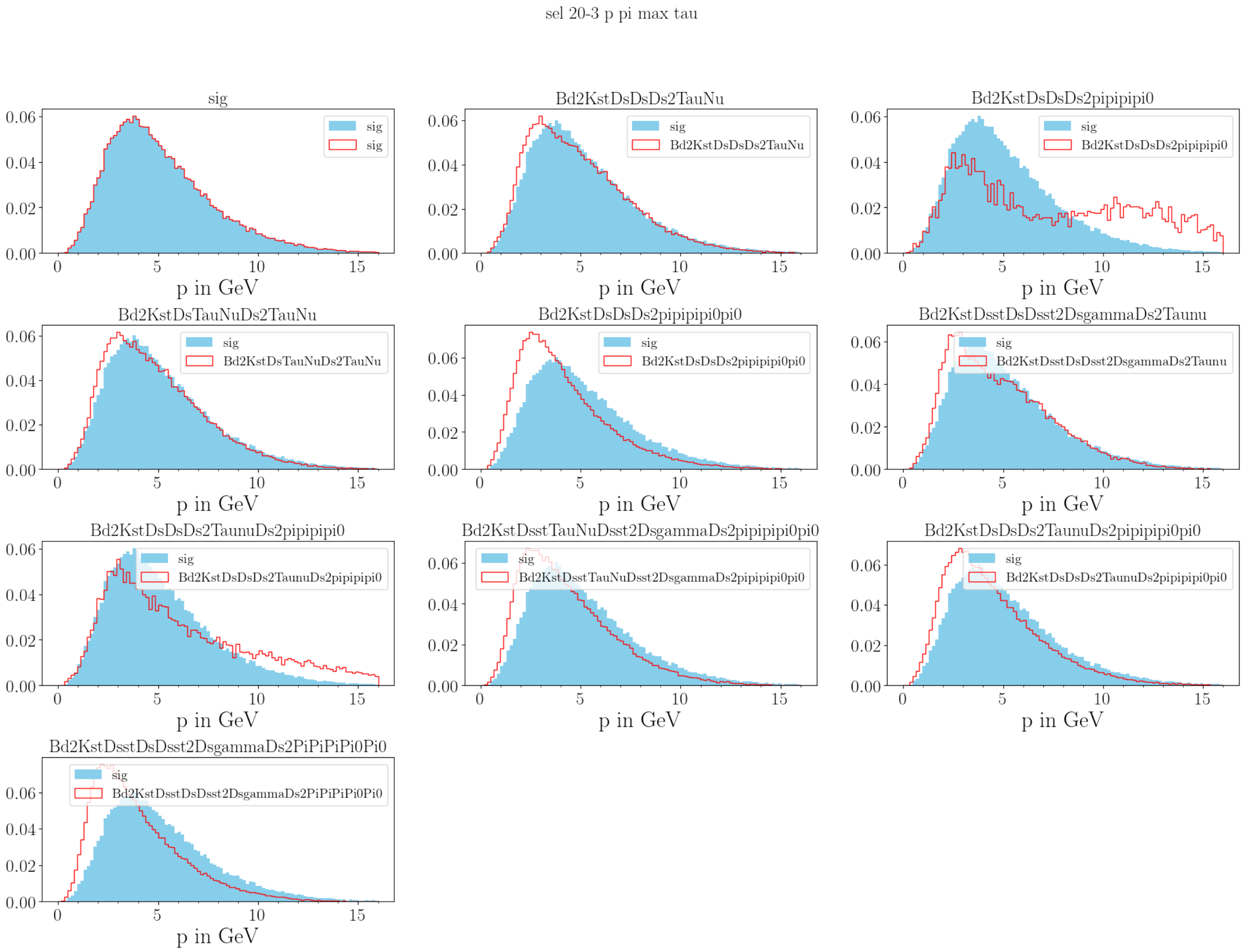

Figure 15: $p_{\pi_{max}}$ from τ candidates distribution as function of the mode.

sel 20-3 p pi min tau

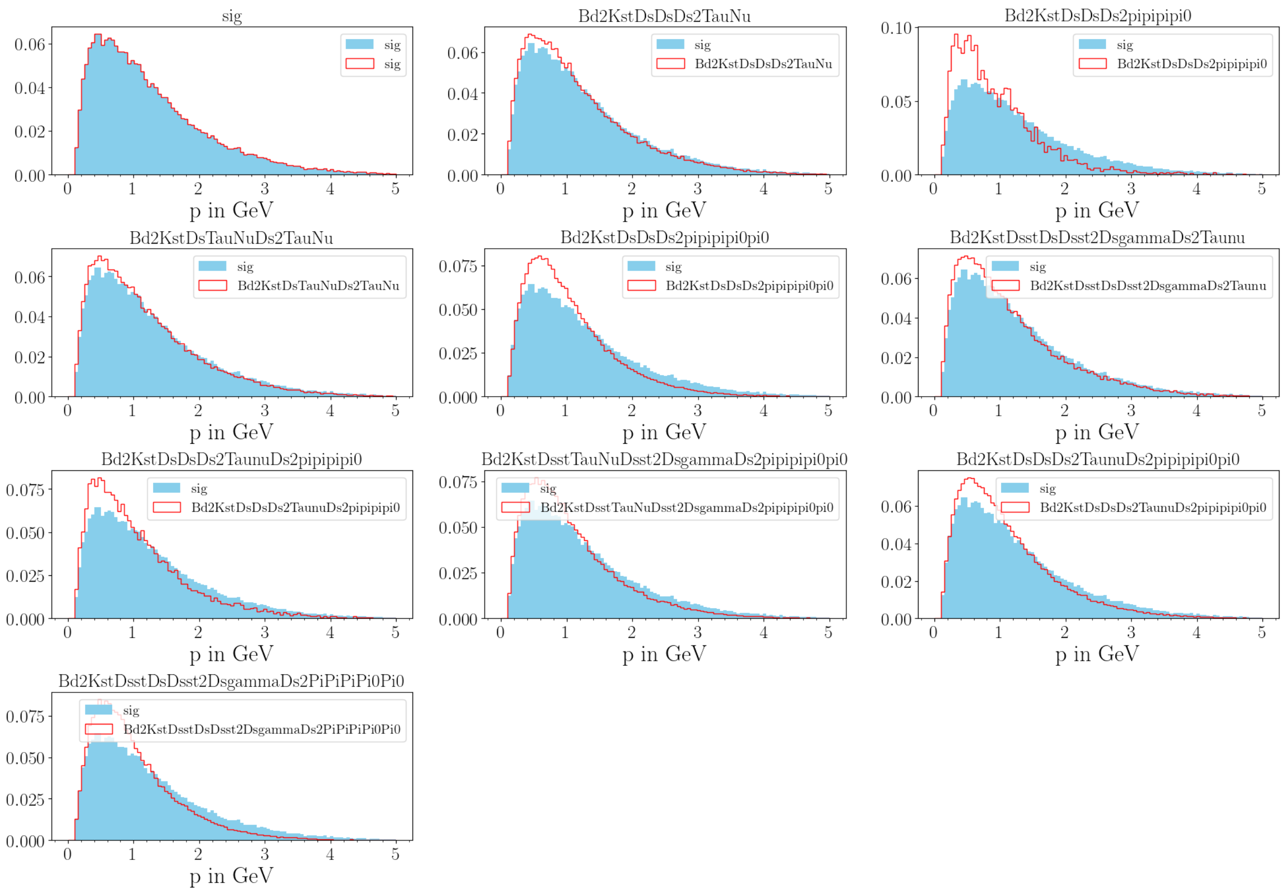

Figure 16: $p_{\pi_{min}}$ from τ candidates distribution as function of the mode.

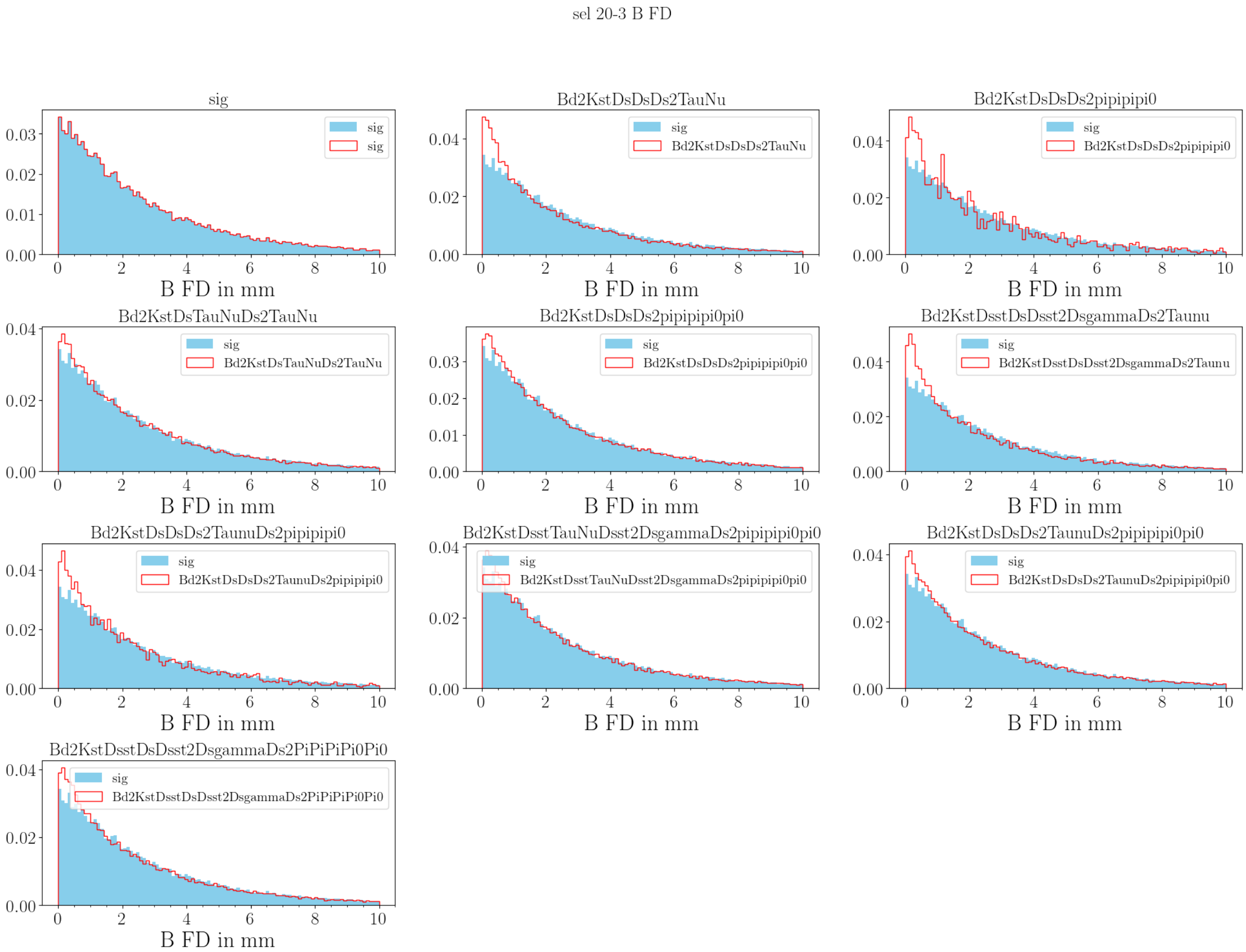

Figure 17: FD_{B^0} candidates distribution as function of the mode.

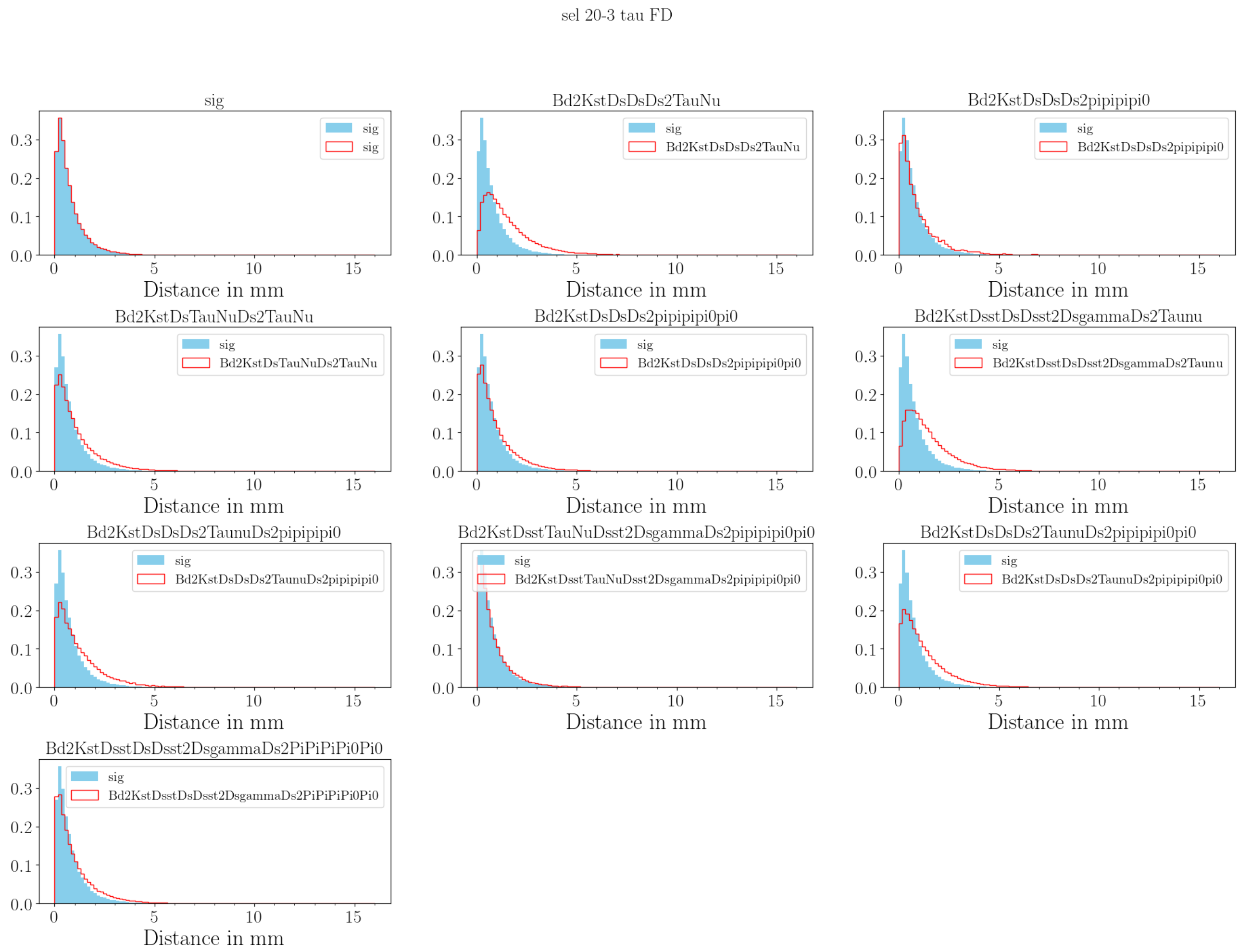

Figure 18: FD_{τ} candidates distribution as function of the mode.

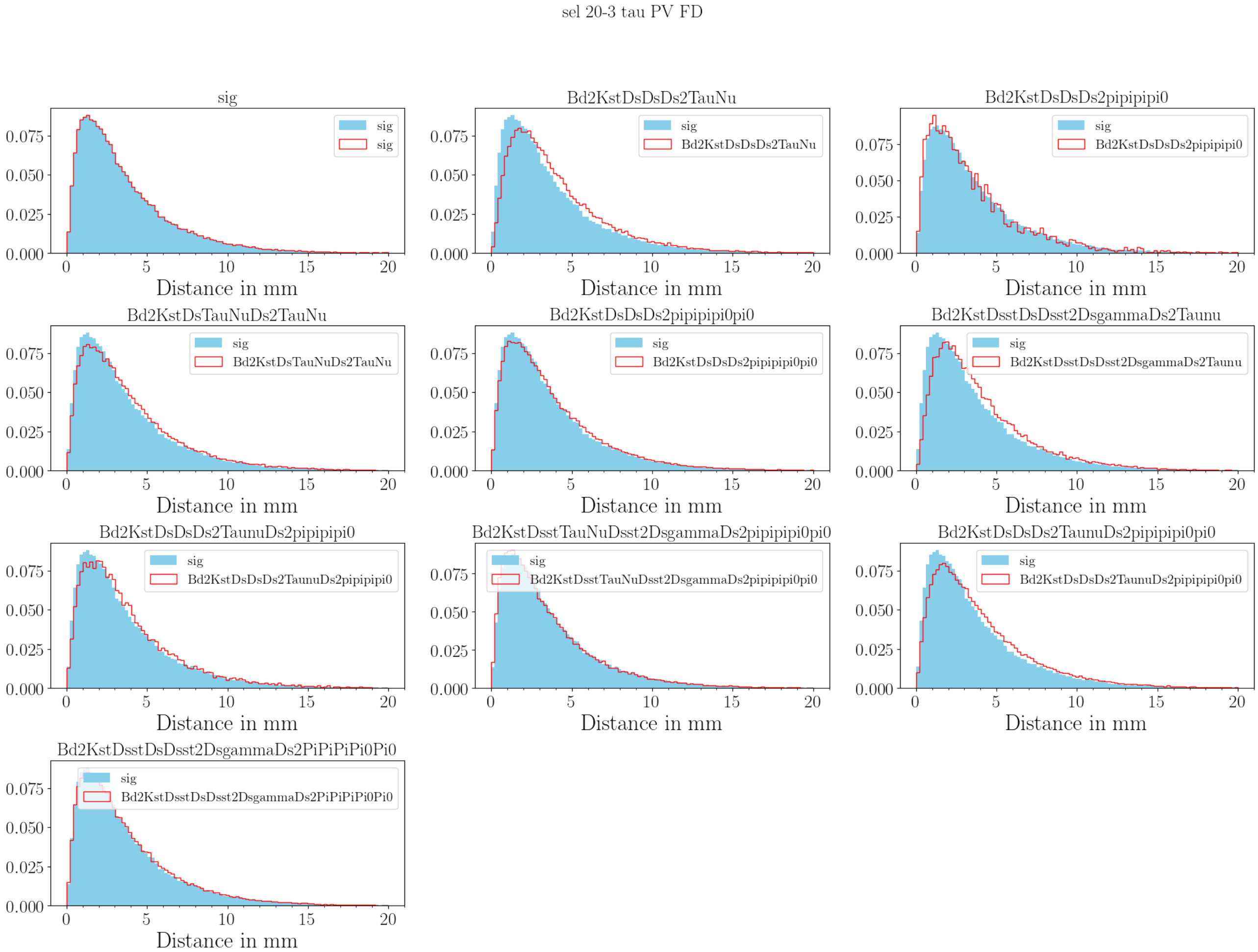

Figure 19: PV to TV distance distribution as function of the mode.

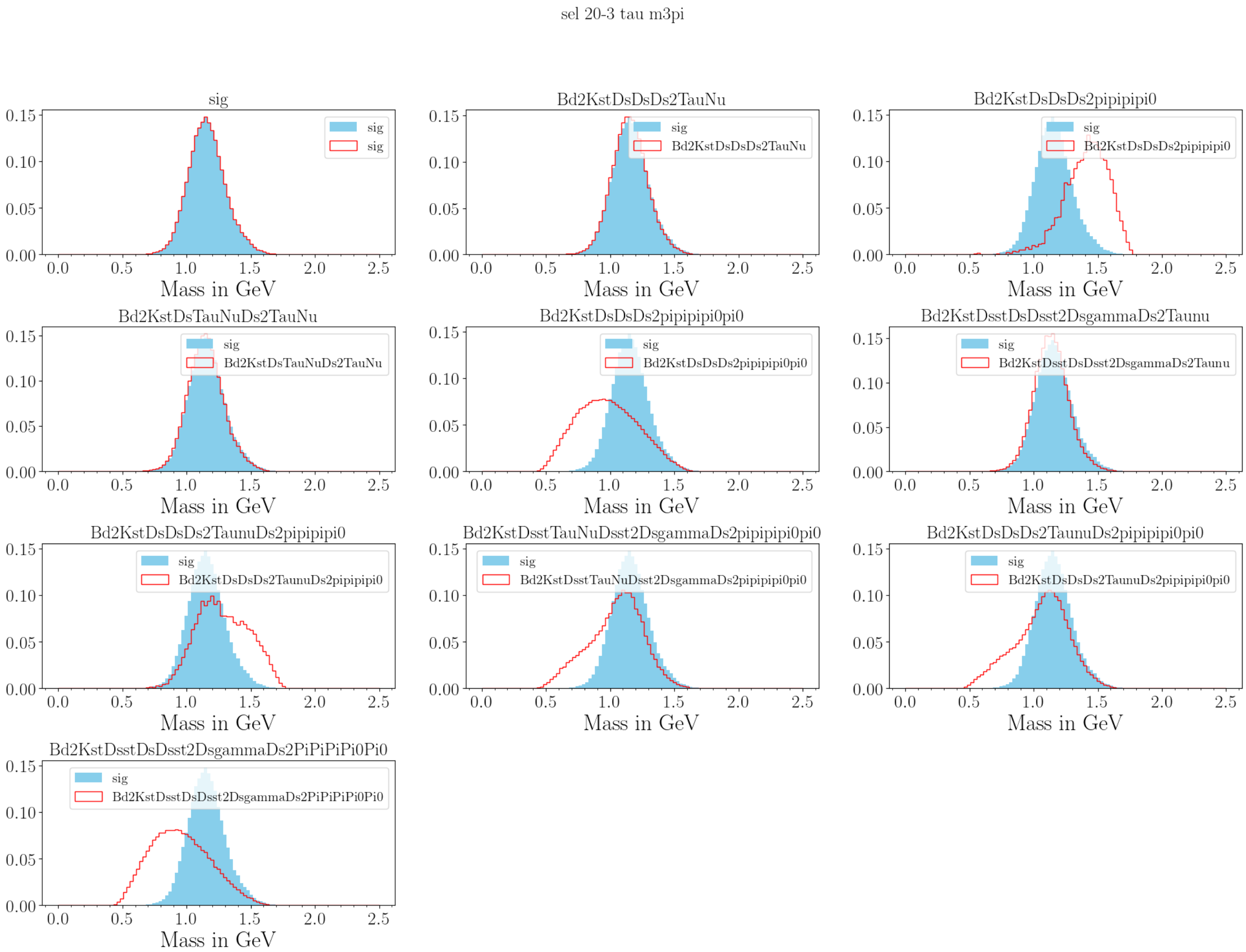

Figure 20: $m_{3\pi}$ from τ candidates distribution as function of the mode.

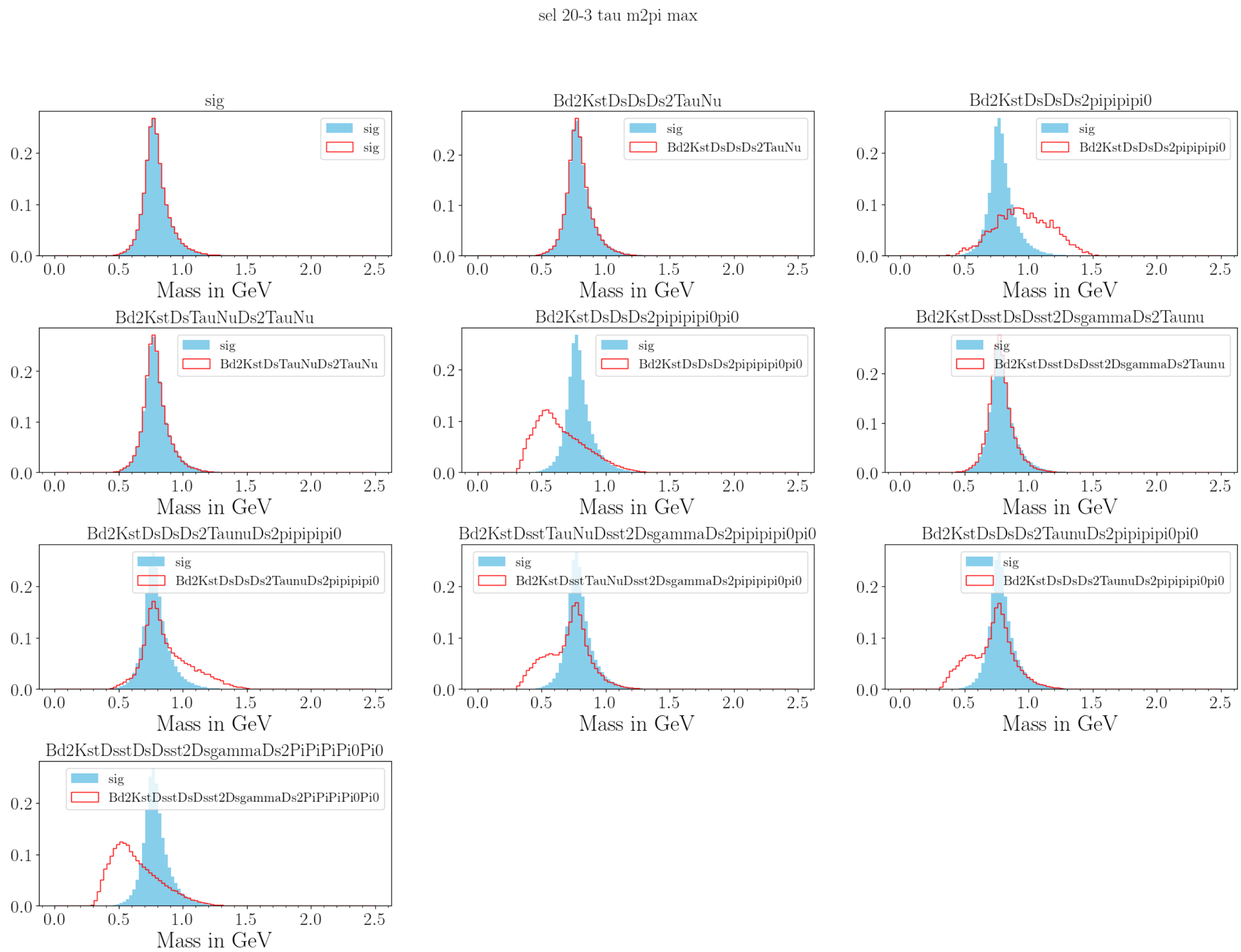

Figure 21: $m_{2\pi\ max}$ from τ candidates distribution as function of the mode.

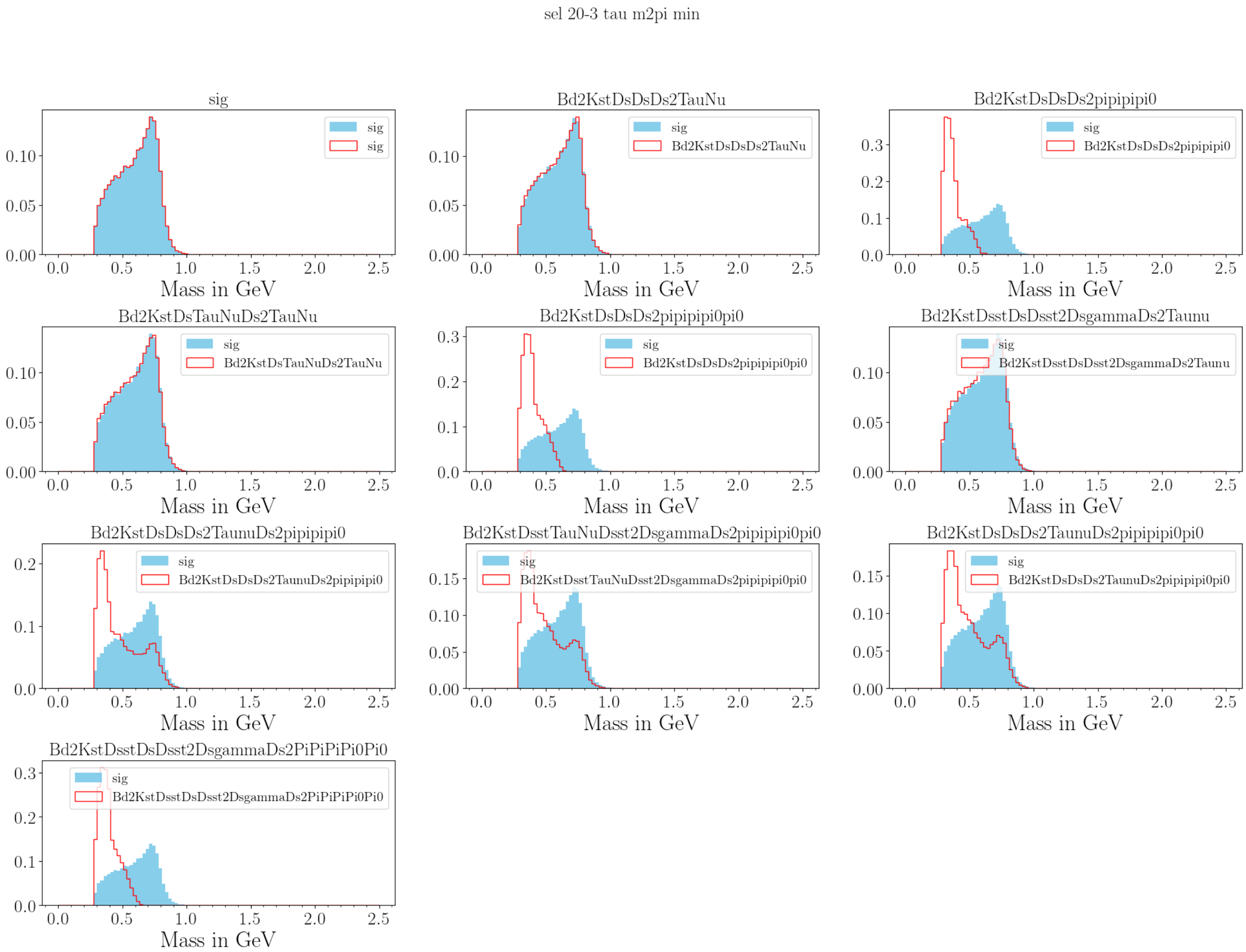

Figure 22: $m_{2\pi\ min}$ from τ candidates distribution as function of the mode.

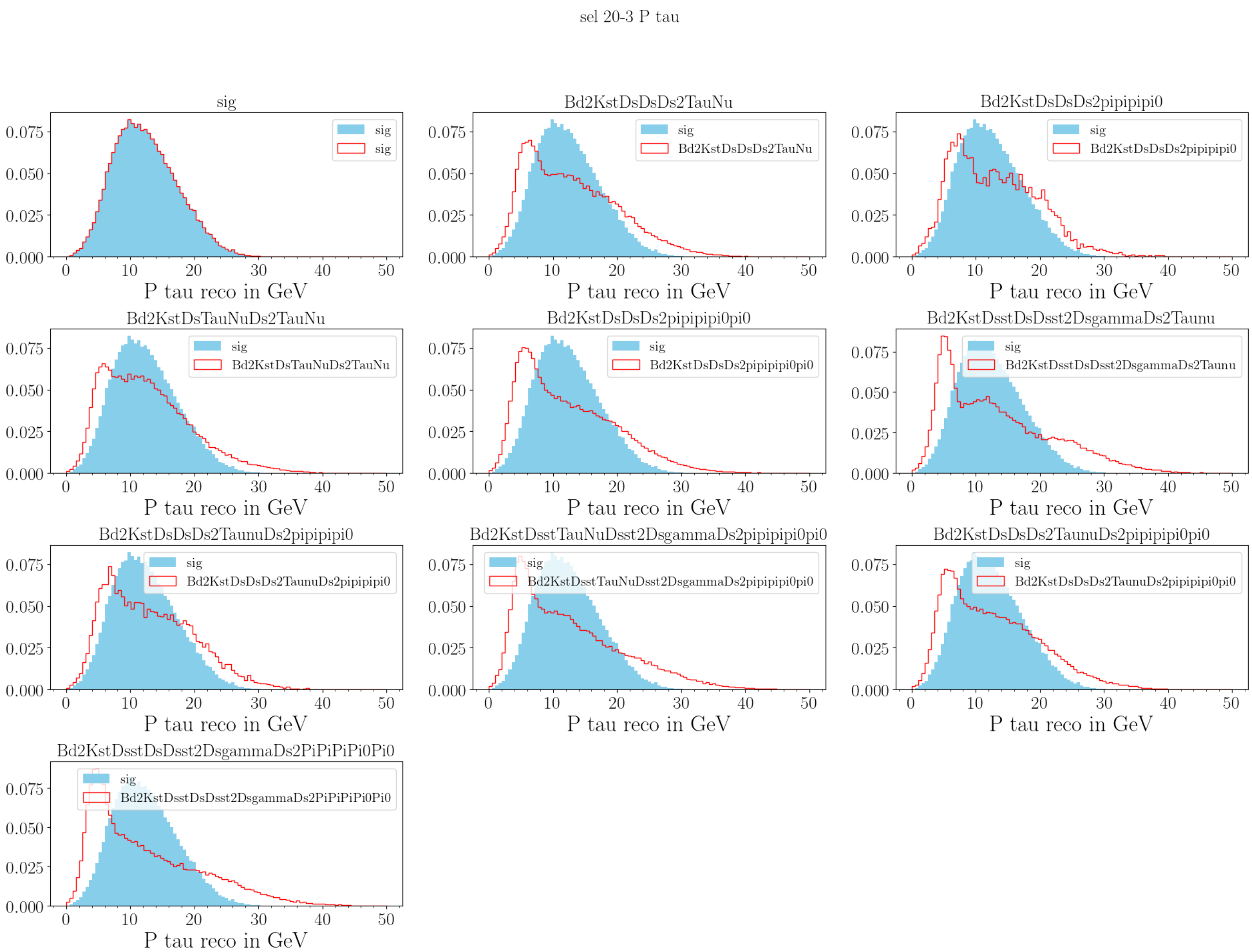

Figure 23: p_τ reconstructed with ν from τ candidates distribution as function of the mode.

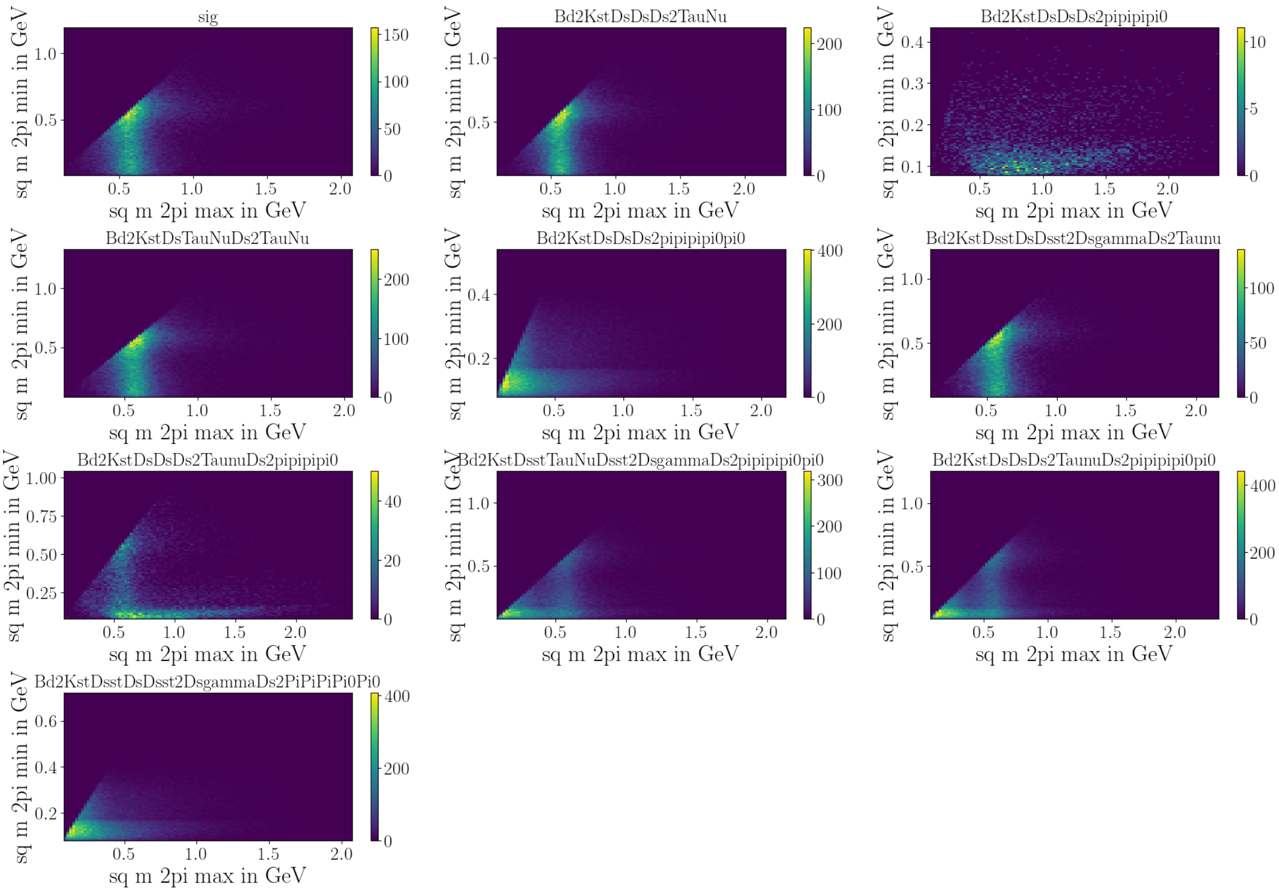

Figure 24: Dalitz plane built from $m_{2\pi}$ of τ candidates distribution as function of the mode.

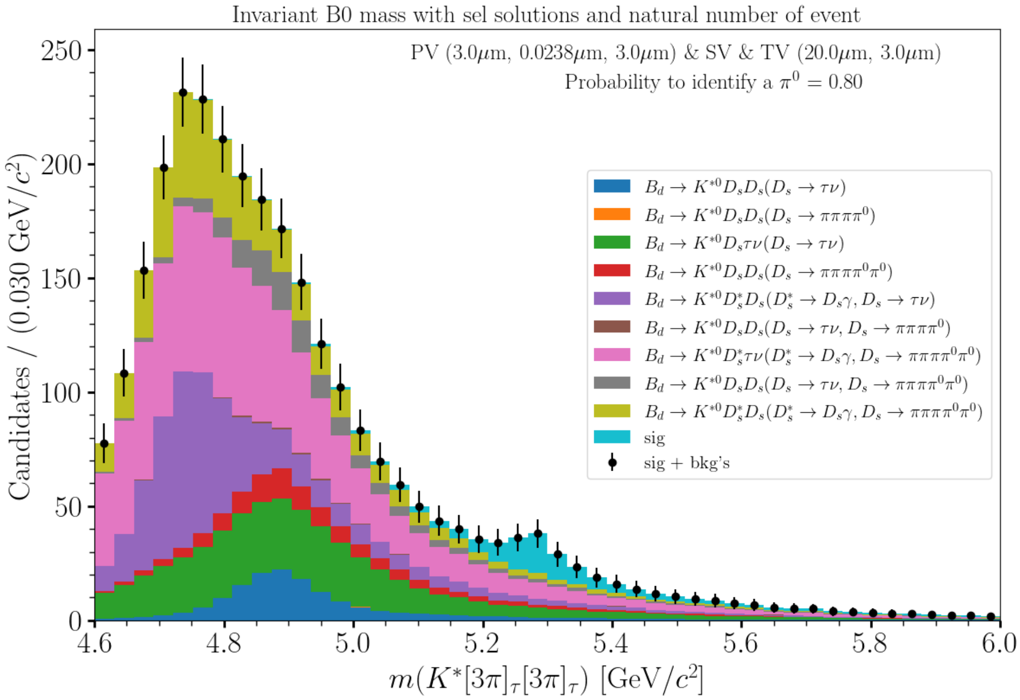

Figure 25: Invariant mass distribution for 20 − 3µm working point after the preselection.

about a factor 3 in the signal region.

7.4.3 Multivariate Analysis

In order to perform the Multivariate Analysis (MVA), it is needed to build a dataset with signal and background events that pass the preselection step, but because of the use of exclusive samples, the available events do not follow the natural proportions of the modes. The strategy to build a coherent dataset is for the signal to take as event as possible w.r.t. the statistics available and for the background to take the same number of event by following the natural proportion of each background w.r.t. the others (taking into account the branching fractions and efficiencies). The whole dataset is then randomly split into 50/50 train/validation datasets.

The XGBoost algorithm is based on the use of a large number of small decision trees (weak classifier individually) in order to classify a set of entries by using their characteristics (set of variables available for each entry). The XGBoost model is created using the dedicated Python package and the Scikit-Learn package tools [36], a hyperparameter tuning step is performed to determine the optimal hyperparameter of the model which are a learning rate of 0.01, a maximum depth of 2, 1000 trees, the objective is set at binary logistic (two class classification in order), the evaluating metric is the AUC (Area Under the Curve of the ROC curve) and the early stopping round parameter is set at 10 (in order to avoid overtrain if there is no improvement by adding trees).

The optimal model is trained on the train dataset and the validation dataset is used to control the overtraining. The discriminative variables defined in Section 7.4.1 are given as features in the MVA. The ROC curves shown in Figure 26 show that the performance of the model is good with an AUC of 0.8749 on the train dataset and 0.8747 on the validation dataset, and the similarity between the two curves gives a first indication of non-overtraining. The overtraining itself is evaluated through the overtraining plot displayed in Figure 27 for which the Kolmogorov-Smirnov tests [37] return p-values of 0.98 for the signal and 0.57 for the background train/validation distributions comparison, which are both above the 0.05 threshold over which the hypothesis that the train/validation distributions are compatible has been considered a

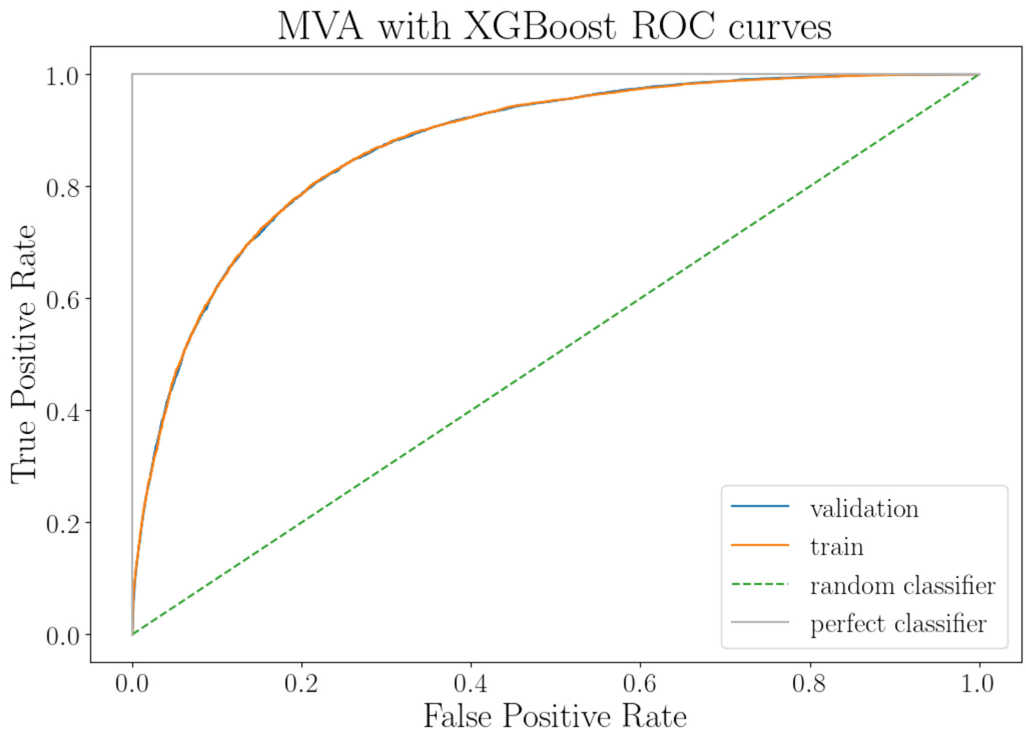

Figure 26: ROC curves.

	all solutions	selected solutions	π^0 detection rate	preselection	MVA
purity	0.004	0.008	0.102	0.307	0.753

Table 6: Summary table of the purity at each step of the selection, evaluated on the $[5.2, 5.6]$GeV mass window for $20 - 3$µm working point. All solutions means without using the selection rule. Selected solutions means with the use of the selection rule.

priori valid. Figure 28 shows the importance of the features that entered into the model.

Finally, the MVA selection is applied after the preselection with a cut at 0.5 on the XGB output, Figure 29 shows that the picture is improved by this step of the selection, this observation is quantitatively confirmed by the purity on the $[5.2, 5.6]$GeV window which is of 0.753 after the whole selection. To quantitatively summarise the improvements brought about by each step of selection, Table 6 displays the purity of the signal evaluated in the $[5.2, 5.6]$GeV/c^2 for each step. None of the backgrounds which have not been generated (see Section 6.4) makes it after the selection.

7.4.4 Selection efficiencies

The efficiencies at each step of the selection in the $[5, 5.6]$GeV mass window are summarised in Table 7. The numbers indicate that the selection is the most efficient against $D_s \to 3\pi 2\pi^0$ backgrounds, which were the dominant ones. The $D_s \to \tau\nu$ backgrounds, which are the most irreducible ones, are reduced, but the selection is expectedly less efficient on them.

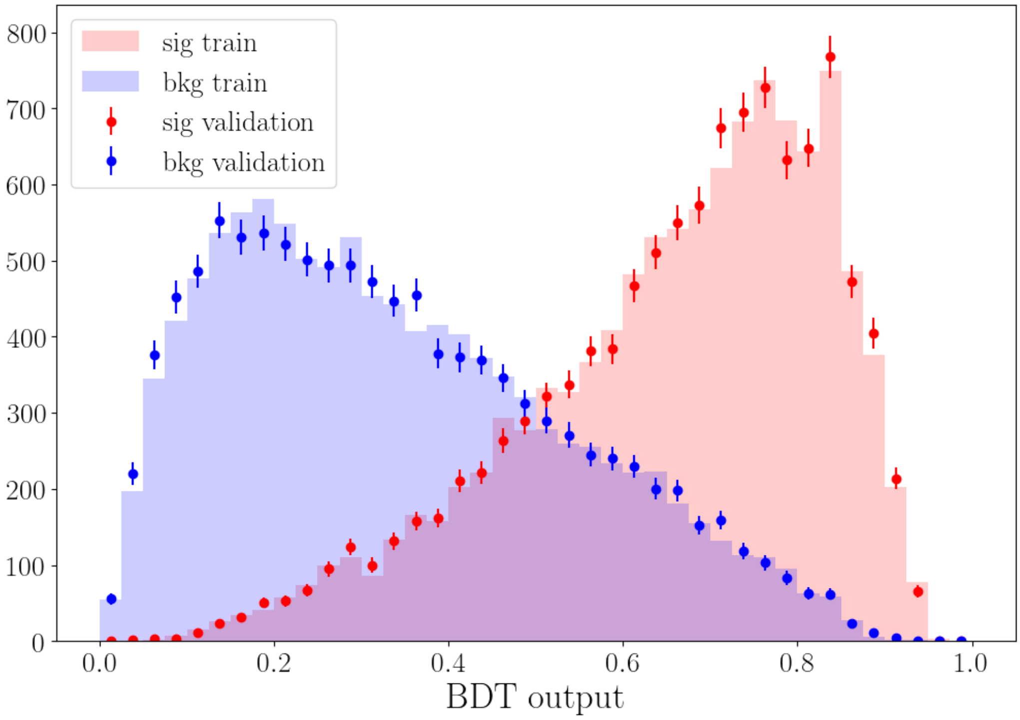

Figure 27: Overtraining plot.

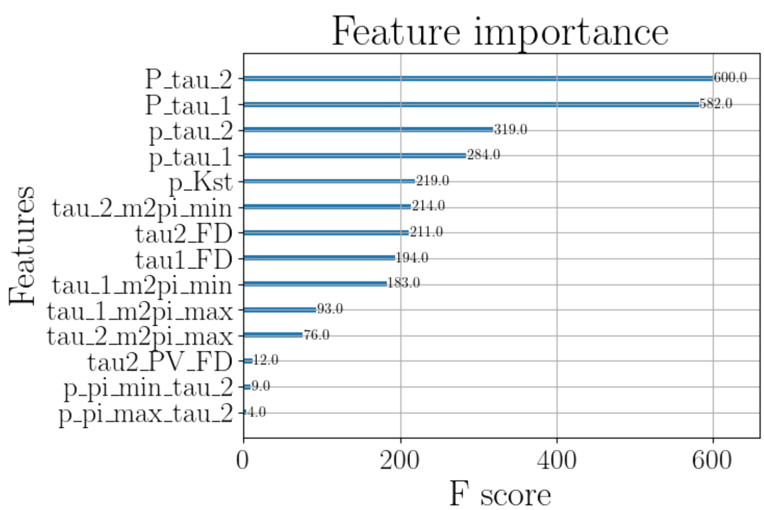

Figure 28: Features importance plot.

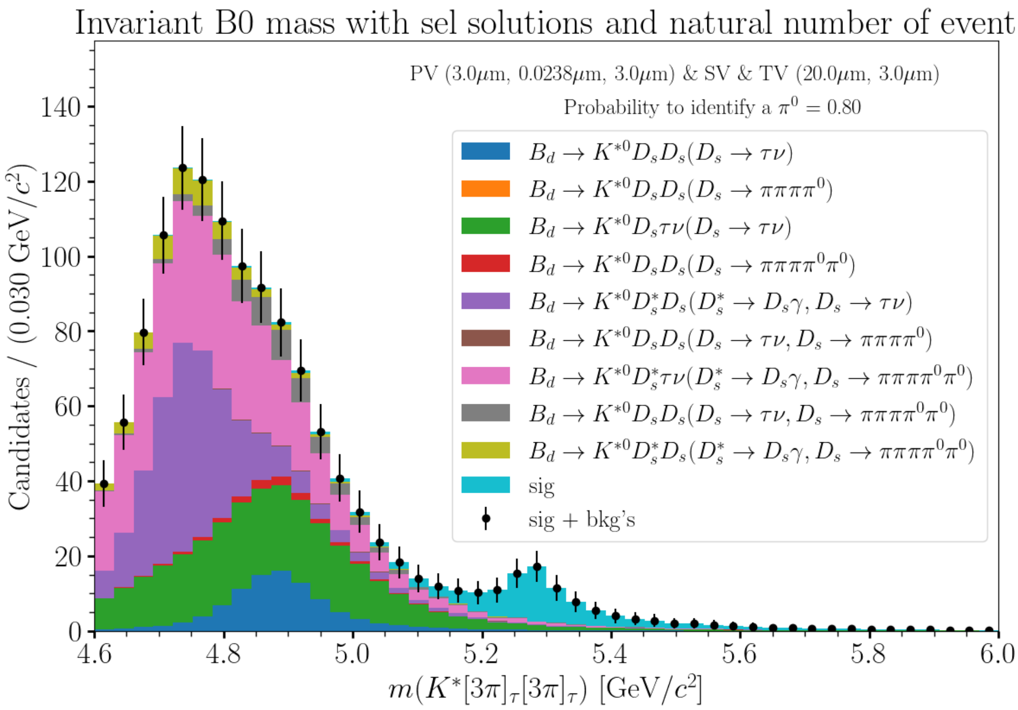

Figure 29: Invariant-mass distribution of the B^0 candidates after the XGBoost selection for the working points $20 - 3$µm.

Mode	Preselection efficiency (%)	MVA efficiency (%)	Total selection efficiency (%)
Signal	70.0	78.1	54.7
$B^0 \to K^{*0} D_s D_s, D_s \to \tau\nu$	59.7	60.9	36.4
$B^0 \to K^{*0} D_s D_s, D_s \to 3\pi\pi^0$	60.3	6.5	3.9
$B^0 \to K^{*0} D_s D_s, D_s \to 3\pi 2\pi^0$	10.2	13.1	1.3
$B^0 \to K^{*0} D_s D_s, D_s \to \tau\nu/3\pi\pi^0$	60.8	33.4	20.3
$B^0 \to K^{*0} D_s D_s, D_s \to \tau\nu/3\pi 2\pi^0$	23.7	38.1	9.0
$B^0 \to K^{*0} D_s^* D_s, D_s \to \tau\nu$	58.9	58.7	34.6
$B^0 \to K^{*0} D_s^* D_s, D_s \to 3\pi 2\pi^0$	7.9	11.2	8.1
$B^0 \to K^{*0} D_s \tau\nu, D_s \to \tau\nu$	64.3	65.4	42.1
$B^0 \to K^{*0} D_s^* \tau\nu, D_s \to 3\pi 2\pi^0$	22.9	42.2	9.7

Table 7: Summary table of the selection efficiency as function of the mode on the $[5, 5.6]$GeV mass window for $20 - 3$µm working point.

8 Precision of the branching fraction measurement

8.1 Method

The goal of this study is to provide vertex detectors requirements in order to measure $B^0 \to K^{*0}\tau\tau$ at FCC-*ee*. The quantity chosen to evaluate the feasibility of the measurement is the precision on the branching fraction measurement. The precision on the branching fraction measurement is accessed from a fit to the invariant-mass distributions of the signal and backgrounds that pass the selection (e.g. distributions like the one in Figure 29) for each vertexing configuration. The precision of the branching fraction measurement is defined as:

$$P = \frac{\sigma_{N_{\text{signal}}}}{N_{\text{signal}}}, \tag{8.1}$$

where N_{signal} can be either the fitted or the expected signal yield and $\sigma_{N_{\text{signal}}}$ is the uncertainty. The number of signal and background events are determined in the range of invariant masses[5.0,6.0] GeV/c^2 from a maximum likelihood fit. The significance of the signal in this range is used as a conservative figure of merit of the reconstruction performance. A comment is in order about the dependance of the performance with the choice of the invariant-mass range: restricting it to the region [5200,5600] MeV/c^2 would yield to a better local significance of the signal. Yet, this assumes an accurate knowledge of the functional shapes of signal and background candidates that would require the definition and the use of background calibration samples; this study is beyond the scope of this work.

The fit is performed in the invariant mass range of $[5.0, 6.0]$GeV in order to consider the signal and the decreasing part of the backgrounds. The model used to fit the signal part is a double-sided Crystal Ball P.D.F. (Probability Density Function) that describes the tails and the peak, and an additional Gaussian P.D.F. with a shared mean to improve the description of the peak. The background part is described with a double decreasing exponential P.D.F.. The fit is performed with the Maximum Logarithmic Likelihood (MLL) method implemented in RooFit [38] and the convergence is evaluated with error estimates given by Minuit2 minimizer and Hesse.

The fitting scheme is the following :

1. definition of the signal fit model,
2. fit of the signal only on the whole available statistics (no rescale),
3. extraction of the signal fit parameters,
4. set as constant all the signal fit shape parameters,
5. definition of the signal and background fit model (combination of the constrained signal pdf and the free background pdf) by introducing yields parameters,
6. fit of the rescaled signal and background distributions together,
7. extraction of the final fit parameters (yields and background pdf parameters).

As an illustration of the fitting scheme, Figure 30 displays the fit of the signal alone and a fit of the background and the signal together for the reference vertexing working point. The uncertainties are given to the readers to judge for the sensitivity of the measurement with the actual statistics.

The precision of the measurement is determined for each vertexing configuration, as explained above. The plots equivalent to Figure 30 for other configurations are given in Appendix

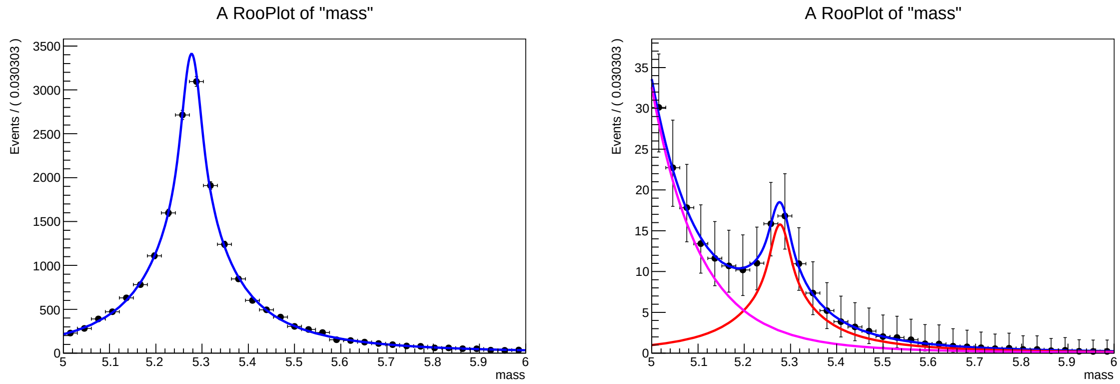

Figure 30: Fit of the signal (left) and fit of signal + background (right) in order to determine the precision on the BF measurement for the $20-3$µm working point.

L-T smearing configuration	20-1µm	20-2µm	20-3µm	20-4µm	20-5µm	20-6µm	20-7µm	20-8µm
N_{signal}	117.79	100.27	86.02	75.70	66.79	59.69	53.62	48.32
$\sigma_{N_{signal}}$	16.55	17.97	20.12	22.09	24.14	24.95	27.76	29.21
Precision	0.14	0.18	0.23	0.29	0.36	0.42	0.52	0.60

Table 8: Table of the precision on the branching fraction measurement as function of the transverse emulated smearing on secondary and tertiary vertices, for a longitudinal smearing of 20 µm.

??. The signal yield uncertainty as defined in equation 8.1 is measured from the fit, the expected signal yield is used (extracted from the distributions after selection) to minimise the impact of the statistical fit fluctuation from one working point to another and the precision is finally determined.

8.2 Results and vertexing requirements

The results of the precision of the BF measurement of $B^0 \to K^{*0}\tau\tau$ with $\tau \to \pi\pi\pi\nu$ are stored in tables 8 to 10. In terms of visualisation, the results are shown in Figures 31 (only 20 µm longitudinal configuration for readability) and 32. The plots show that the main driver of the branching fraction measurement is the transverse resolution on the secondary/tertiary vertices. To be able to observe this mode, even at its SM expectation and regarding the actual baseline luminosity of FCC-*ee*, a very good transverse vertexing resolution is required $\mathcal{O}(1\,\mu\text{m})$.The next step of the analysis is to evaluate the vertexing performances of IDEA, an actual simulation of the detector available for FCC-*ee* to add an IDEA working point in the analysis to determine where the state-of-the-art is.

L-T smearing configuration	10-1µm	10-2µm	10-3µm	10-4µm	10-5µm	10-6µm	10-7µm	10-8µm
N_{signal}	125.97	104.07	87.98	76.83	67.86	60.29	54.82	49.10
$\sigma_{N_{signal}}$	15.91	17.09	19.42	21.16	21.98	25.84	26.89	27.94
Precision	0.13	0.16	0.22	0.28	0.32	0.43	0.49	0.57

Table 9: Table of the precision on the branching fraction measurement as function of the transverse emulated smearing on secondary and tertiary vertices, for a longitudinal smearing of 10 µm

L-T smearing configuration	5-1µm	5-2µm	5-3µm	5-4µm	5-5µm	5-6µm	5-7µm	5-8µm
N_{sig}	128.09	105.10	89.44	76.00	67.88	61.10	55.01	49.16
$\sigma_{N_{sig}}$	15.68	17.01	18.74	20.48	22.24	24.71	28.11	26.61
Precision	0.12	0.16	0.21	0.27	0.33	0.40	0.51	0.54

Table 10: Table of the precision on the branching fraction measurement as function of the transverse emulated smearing on secondary and tertiary vertices, for a longitudinal smearing of 5 µm

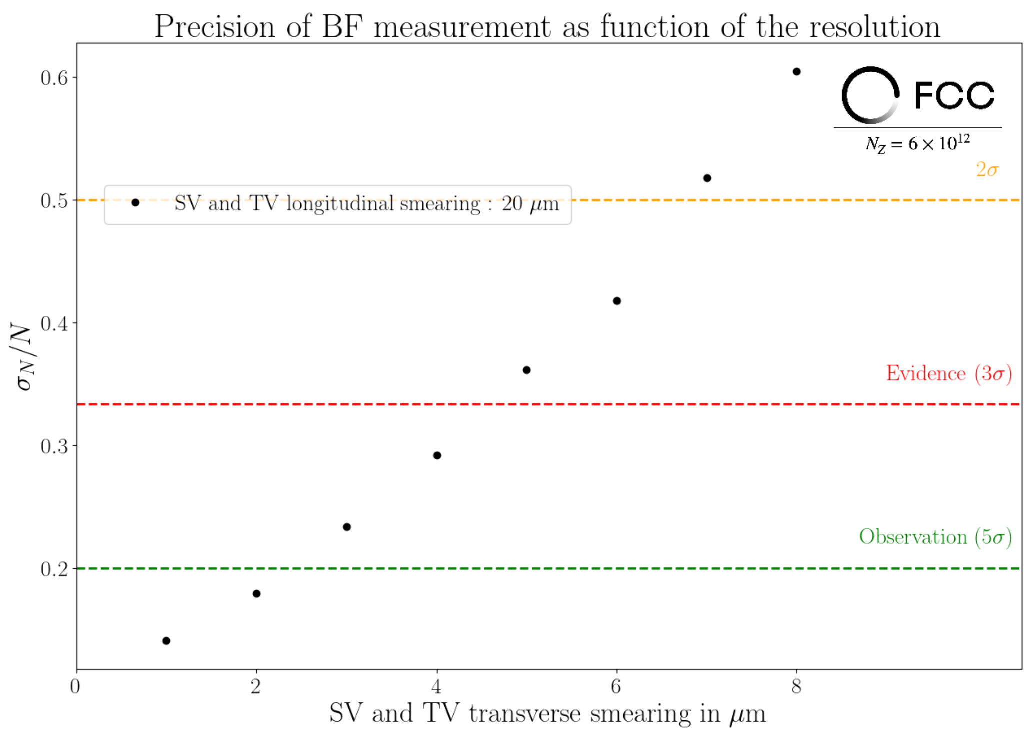

Figure 31: Precision of the measurement as function of the transverse vertexing resolution with a longitudinal resolution set at 20 µm.

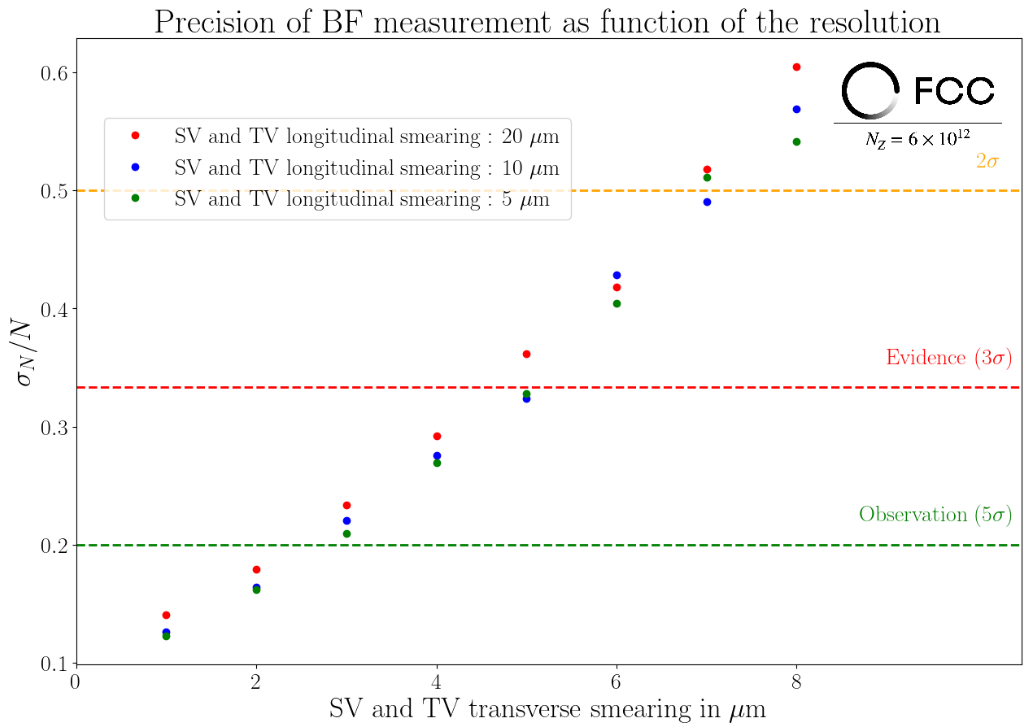

Figure 32: Precision of the measurement as function of the transverse vertexing resolution with all longitudinal resolutions.

9 Comparison to one state of the art vertex detector concept

9.1 Actual IDEA vertexing performance on $B^0 \to K^{*0}\tau\tau$

In order to add a state-of-the-art vertex detector working point to the analysis, the FCCAnalyses software VertexFitterSimple tools (allowing to perform vertexing with the IDEA simulated vertex detector) is used. For that purpose another FCCAnalysis analyzer is created to run on the whole available signal statistics and evaluate the primary, secondary and tertiary vertices reconstruction performances. Given the signal samples generated for the analysis, the analyzer determines the reconstructed vertex position in Cartesian coordinates w.r.t. the Beam Spot Constraints set to the default FCC$-ee$ Z pole values of $(4.5, 20e^{-3}, 300)$ µm and concurrently saves the MC-Truth vertices information for the upcoming resolution determination.

The primary vertex positions are fitted in the classic way of the vertexing tools implementation; the vertex is first fitted with all the tracks, only the tracks compatible with it are kept and then the vertex is refitted from them. Concerning the secondary and tertiary vertices positions, the algorithm was not adapted to this analysis due to the large soft tracks multiplicity of the signal and was not able to fit their vertices from the secondary tracks alone. To be able to fit the position of the secondary and tertiary vertices in the right way, the tracks have been MC-seeded in the analyser; this procedure prevents to determine the actual IDEA vertexing efficiency. A conservative vertexing efficiency of $\epsilon_{vertexing} = 0.8$ is therefore used similarly to what was used in the signal selection design. The analyzer outputs are used to construct the distributions of the displacement of the reconstructed vertices w.r.t. the MC-Truth vertices positions. Concerning the primary vertices, the displacements are built and projected onto the detector Cartesian basis. For the secondary and tertiary vertices, it is more challenging, the displacements are projected onto the particle decaying direction (longitudinal component) and on two orthogonal directions picked up randomly in the transverse plan of the decay (plan orthogonal to the particle decaying direction and that contain the MC-Truth vertex position) by parameterising a unit circle in the transverse plane of each vertex.

Namely, the first step is to use the Cartesian equation of the plane containing the true vertex position and orthogonal to the decaying particle direction. A random vector that belongs to this plane originating at a random (x, y) point can be defined:

$$z = -\frac{a(x - x_0) + b(y - y_0)}{c} + z_0, \tag{9.1}$$

where (x_0, y_0, z_0) are the coordinates of the true vertex, $\hat{p} = (a, b, c)$ is the unitary vector corresponding to the decaying particle direction. (x, y) denotes a randomly taken point on a circle in the 2D cartesian xOy basis of the detector and z is determined in order to satisfy that (x, y, z) belongs to the transverse plan. The unitary vector $\vec{Y}$ corresponding to the direction between the true vertex and the (x, y, z) point is then formed. A third unitary vector orthogonal to $\vec{Y}$ and $\vec{Z}$ is subsequently built following $\vec{X} = \vec{Y} \times \vec{Z}$. At this step, $\vec{X}$ and $\vec{Y}$ form an orthonormal basis in the transverse plan of the decay. The last transformation features the parameterisation of a unit circle (with a single parameter θ) in the transverse plane in order to determine an unbiased random vector following equation 9.2:

$$\vec{Y'} = \cos\theta \vec{X} + \sin\theta \vec{Y}, \tag{9.2}$$

where $\vec{X}$ and $\vec{Y}$ are used as characteristic (unitary and orthogonal) vectors of the transverse plane. $\vec{Y'}$ is therefore the vector between a random point on the circle and the true vertex position. $\vec{X'}$ is then determined from the vectorial product $\vec{X'} = \vec{Y'} \times \vec{Z}$. The basis described by $\vec{X'}$ and $\vec{Y'}$ is now really random and ready for use.

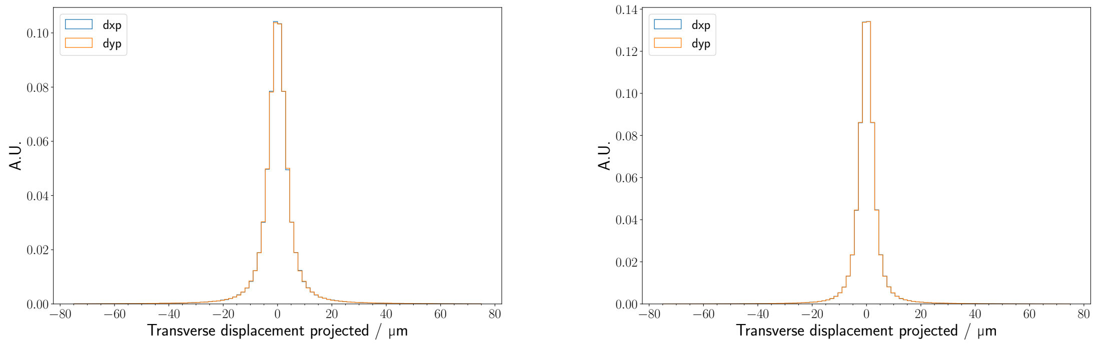

Figure 33: Superposition of the displacements along each randomly pick-up transverse direction denoted as dxp (along $\vec{X'}$) and dyp (along $\vec{Y'}$), for the secondary vertex (left) and tertiary vertex(right).

The two transverse directions picked up randomly are by construction equivalent, as can be seen in Figure 33 and are combined to determine a signed transverse displacement of the vertices in a single distribution for each vertex. In the following IDEA vertex resolutions are determined on each type of vertex (primary, secondary, and tertiary).

Resolutions are estimated by fitting the vertices displacement distributions with the zfit tool [39]. The primary vertex resolutions are fitted with double-Gaussian models on the x and z directions and with a simple Gaussian model for the y axis. Regarding the Figure 34, the combined sigma of the fit provides an estimate of the IDEA primary vertex resolution of $(4.1, 24e^{-3}, 2.9)$µm (the assumptions on the primary vertex fast emulation, in Section 5.4.2, hare set close to this measurement). The primary vertex y resolution is dominated by the beam spot constraints. Concerning the secondary and tertiary vertices, the resolutions are fitted with triple-Gaussian models. Figure 35 displays the resolutions fitted in the longitudinal direction and Figure 36 displays the ones fitted in the transverse direction. There the poor part of the fit taken by the larger Gaussian prevents us from a quick comparison with the fast vertexing emulation shown before but the core gaussian resolutions seem commensurate with the initial working point assumptions in the emulation study. It is interesting to notice that the vertexing performances on the tertiary vertices are better than the one on the secondary vertices due to the additional track used at the tertiary vertices (3 vs. 2) despite the lower momentum on average of these tracks.

In addition of the actual IDEA vertexing working point, a tool that allows to tune the IDEA vertexing performances themselves is available in the FCCAnalyses software. This can be useful in order to determine which experimental parameters have to be improved in priority for this analysis. The next section will present the use of this tool to build various IDEA vertexing working points.

9.2 Vertexing improvement by tuning the tracks performance

To understand how to improve if possible the vertex detector design, a first approach can consist in arbitrarily improve the track parameters determinations. A specific FCC-*ee* software has been used to centrally produce four new samples with improved track performance: twice better resolution on the curvature of the track Ω, impact parameters $(z_0; d_0)$ resolutions improved by 17%, 33% and 50%.

The resolutions from the various IDEA working points are fitted similarly to what has been done for the IDEA baseline working point, all these fits are available from Figures 37 to 48.

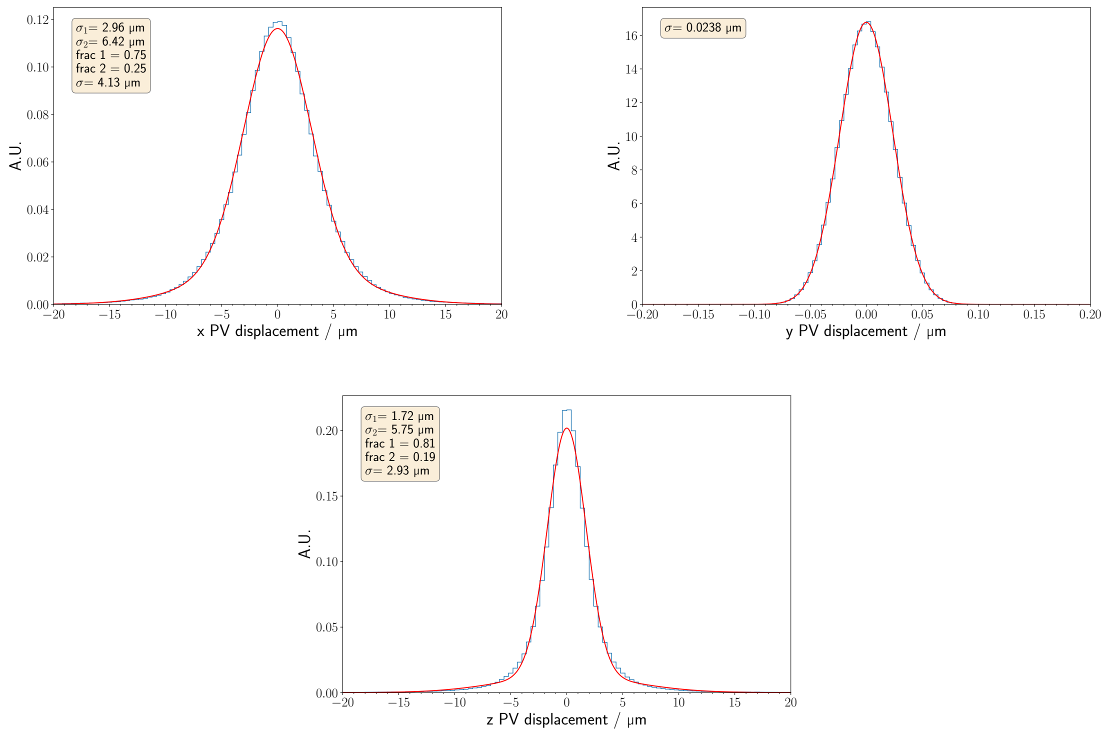

Figure 34: Fit of the IDEA primary vertexing resolutions on cartesian coordinates x (upper left), y(upper right) and z (bottom).

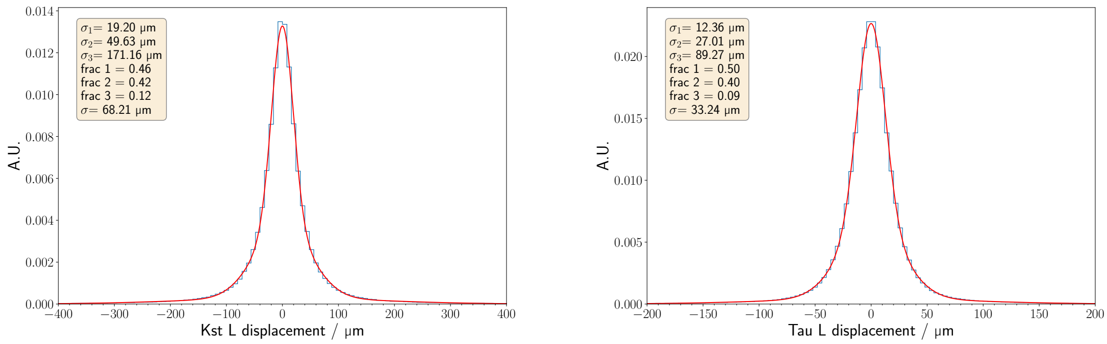

Figure 35: Fit of the IDEA secondary (left) and tertiary (right) longitudinal resolutions.

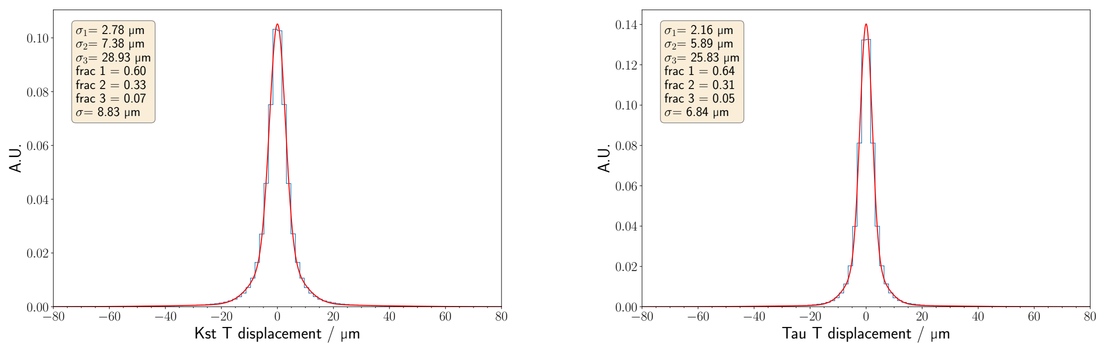

Figure 36: Fit of the IDEA secondary (left) and tertiary (right) transverse resolutions.

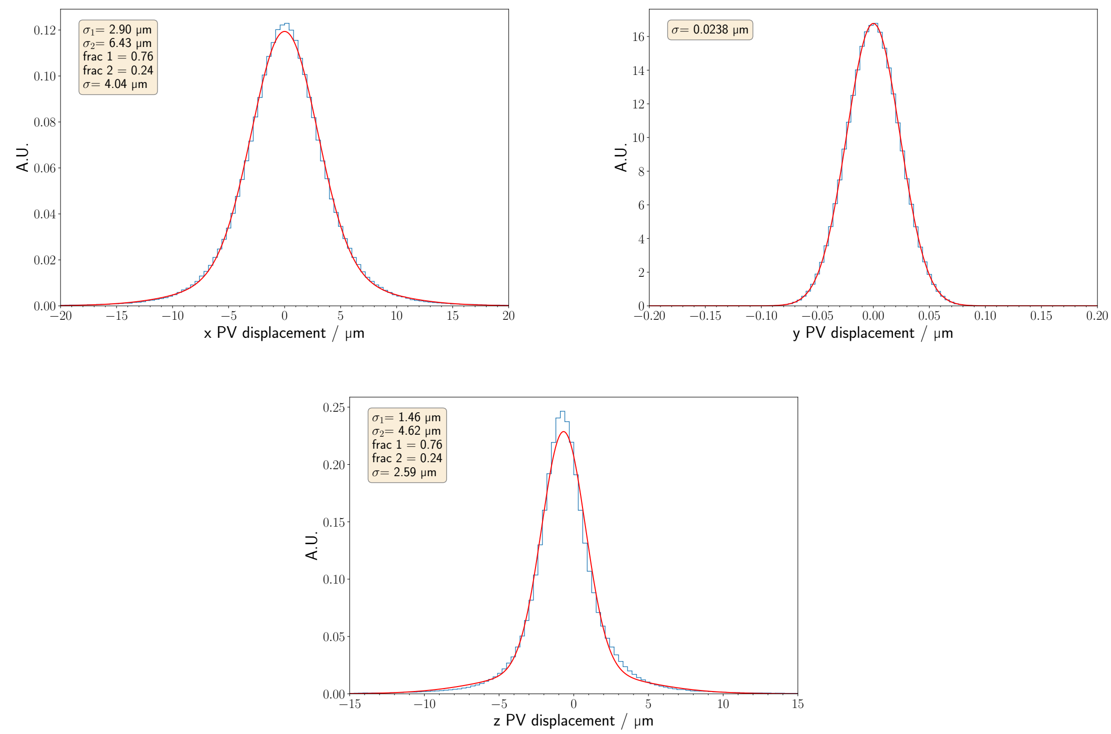

Figure 37: Fit of the various IDEA, with two times better Ω measurement, primary vertexing resolutions on cartesian coordinates x (upper left), y(upper right) and z (bottom).

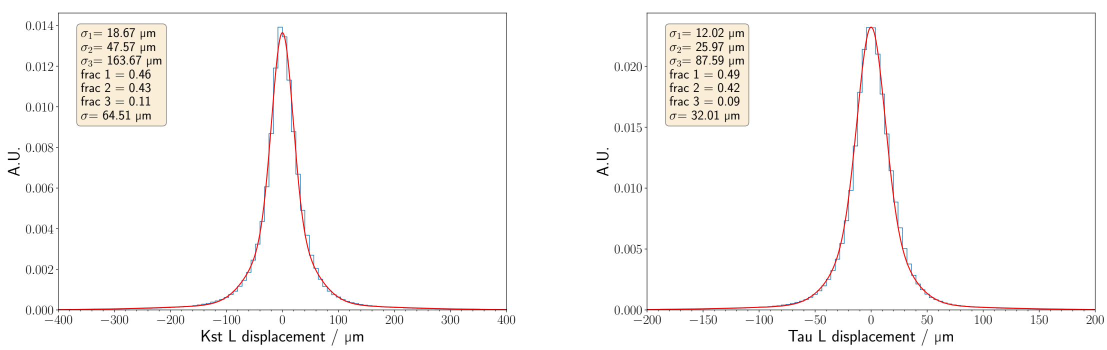

Figure 38: Fit of the various IDEA, with two times better Ω measurement, secondary (left) and tertiary (right) longitudinal resolutions.

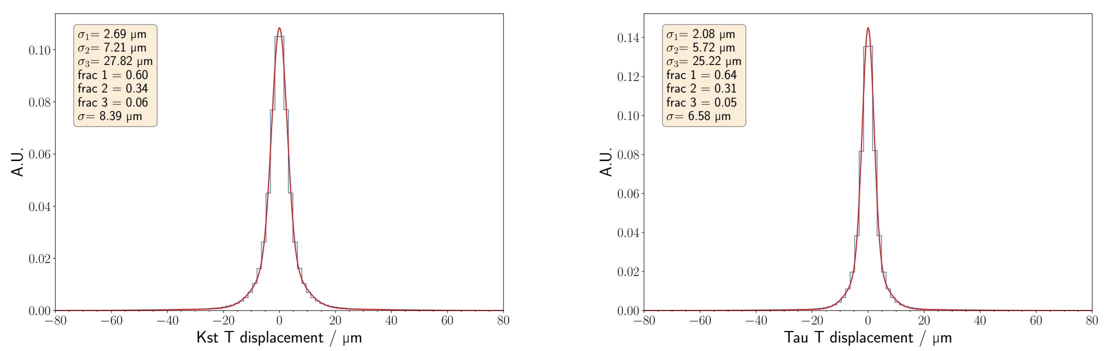

Figure 39: Fit of the various IDEA, with two times better Ω measurement, secondary (left) and tertiary (right) transverse resolutions.

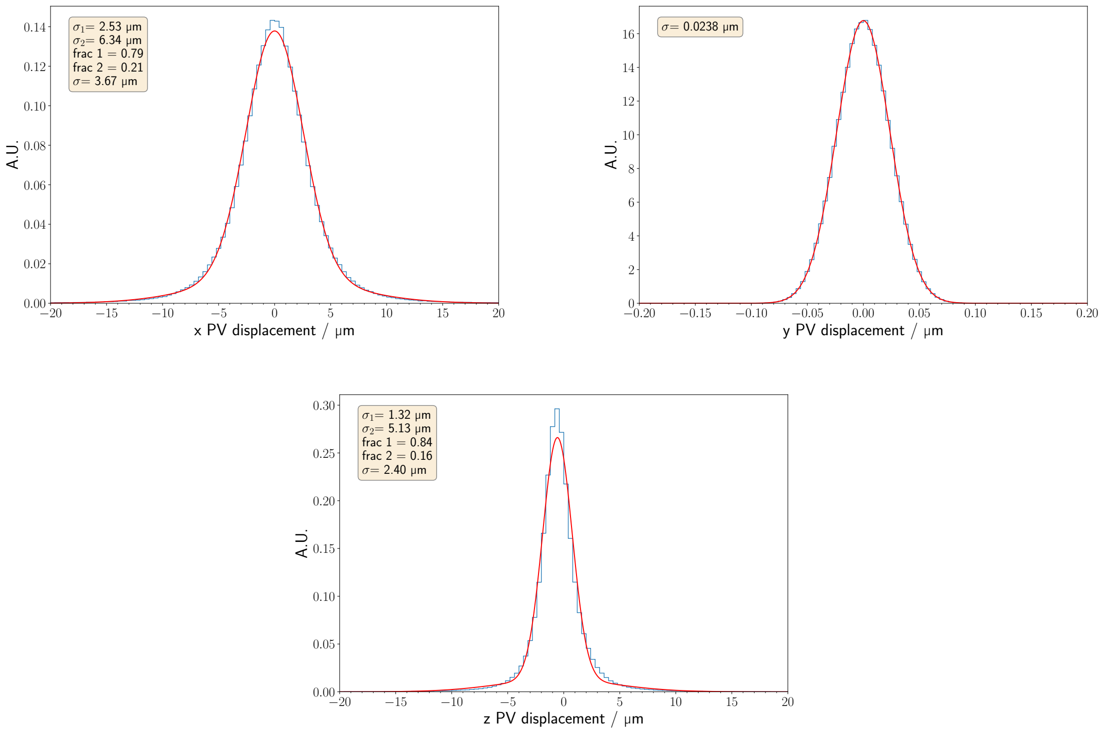

Figure 40: Fit of the various IDEA, with 1.2 times better IP measurement, primary vertexing resolutions on cartesian coordinates x (upper left), y(upper right) and z (bottom).

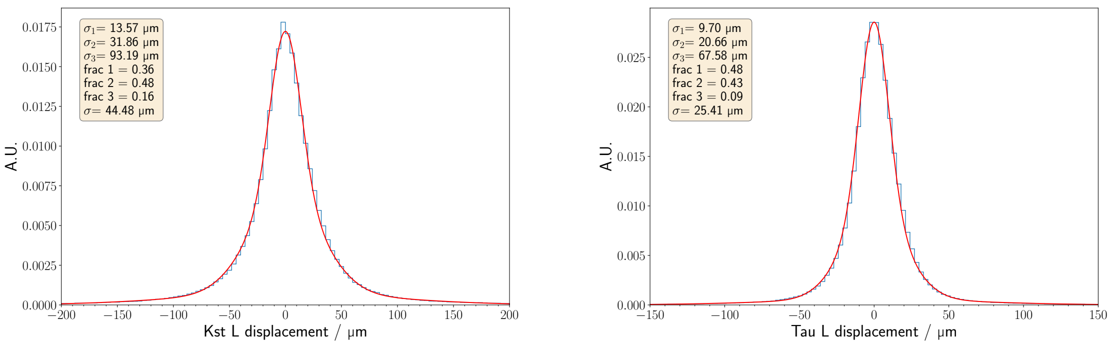

Figure 41: Fit of the various IDEA, with 1.2 times better IP measurement, secondary (left) and tertiary (right) longitudinal resolutions.

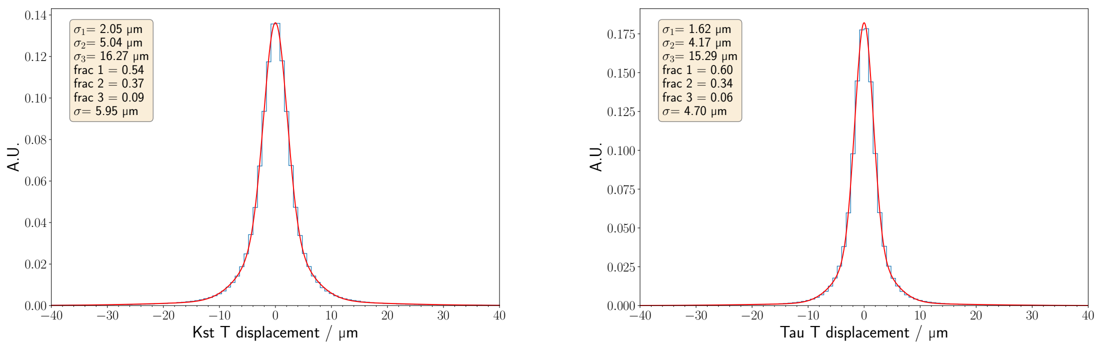

Figure 42: Fit of the various IDEA, with 1.2 times better IP measurement, secondary (left) and tertiary (right) transverse resolutions.

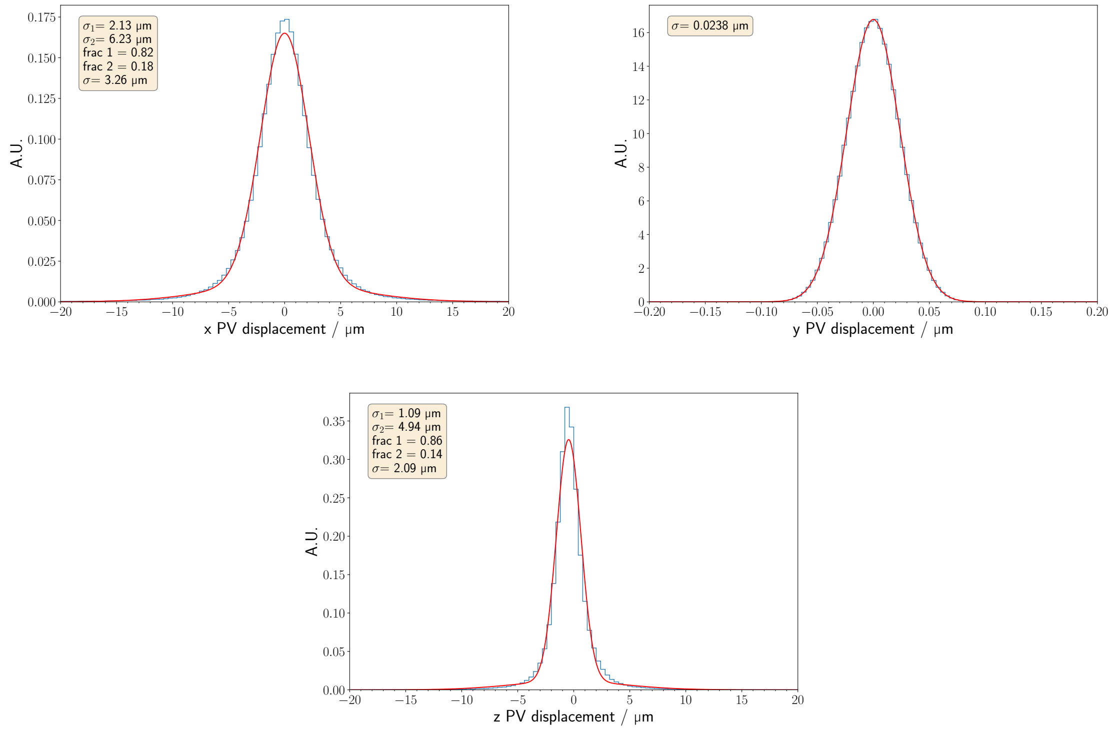

Figure 43: Fit of the various IDEA, with 1.5 times better IP measurement, primary vertexing resolutions on cartesian coordinates x (upper left), y(upper right) and z (bottom).

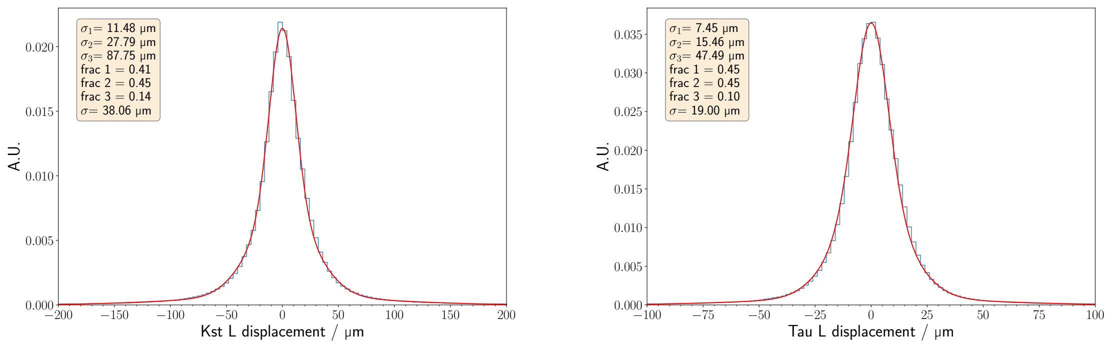

Figure 44: Fit of the various IDEA, with 1.5 times better IP measurement, secondary (left) and tertiary (right) longitudinal resolutions.

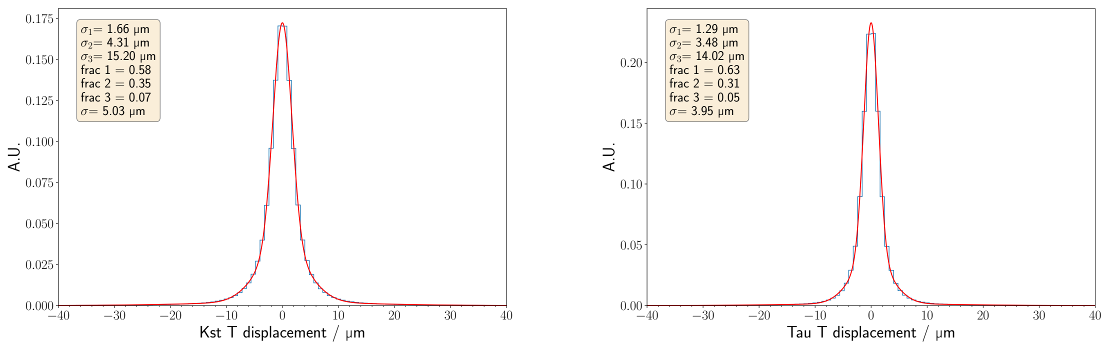

Figure 45: Fit of the various IDEA, with 1.5 times better IP measurement, secondary (left) and tertiary (right) transverse resolutions.

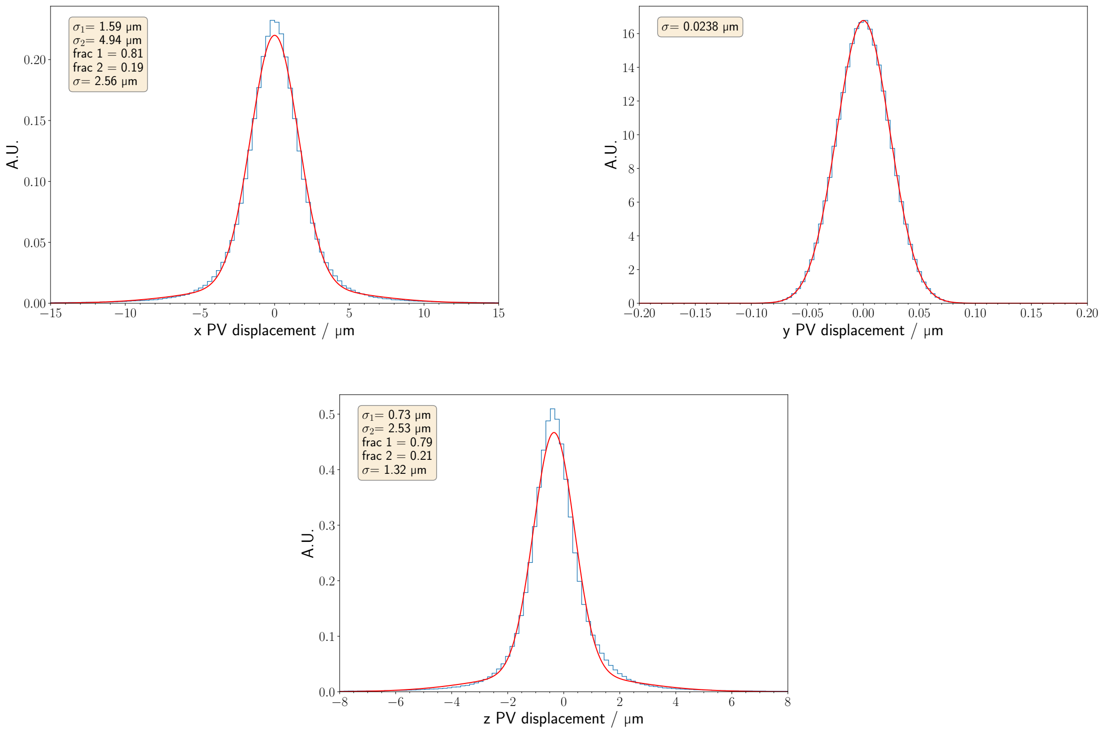

Figure 46: Fit of the various IDEA, with two times better IP measurement, primary vertexing resolutions on cartesian coordinates x (upper left), y(upper right) and z (bottom).

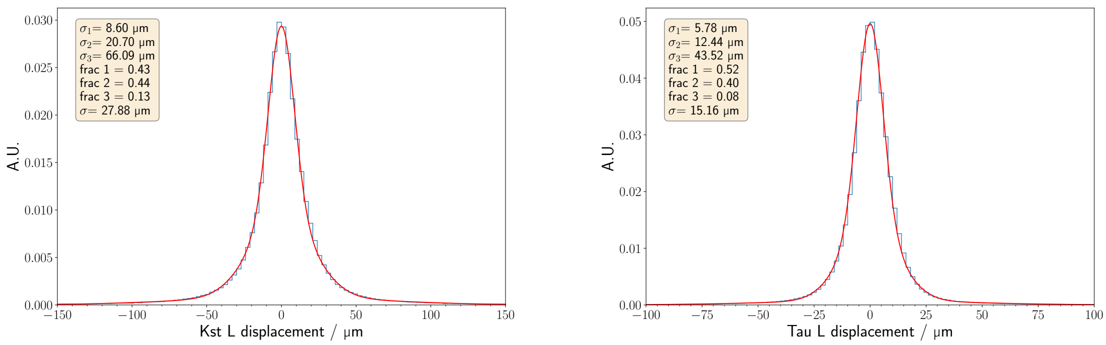

Figure 47: Fit of the various IDEA, with two times better IP measurement, secondary (left) and tertiary (right) longitudinal resolutions.

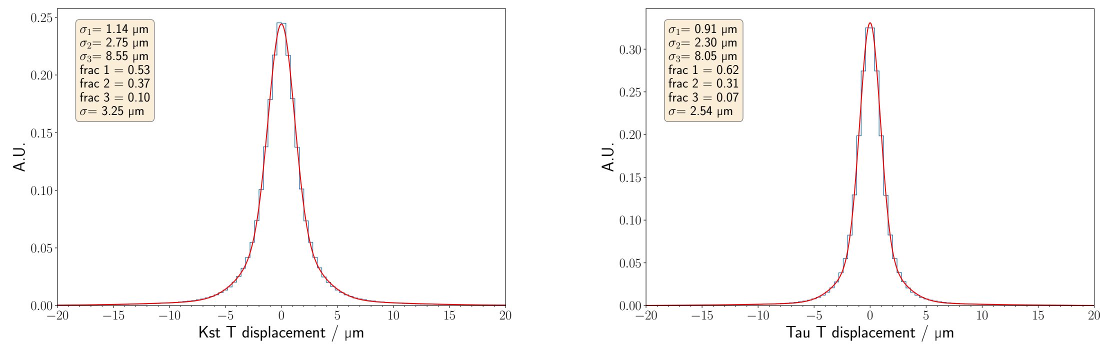

Figure 48: Fit of the various IDEA, with two times better IP measurement, secondary (left) and tertiary (right) transverse resolutions.

9.3 IDEA emulation

Each IDEA working point is emulated in the analysis following the aforementioned resolutions. Because of the fact that the primary vertex resolution is not the main driver of the performances, the primary vertex position for the IDEA working point is smeared in the analysis by a 3D Gaussian smearing that follows the combined σ given by the fits. Concerning the secondary and tertiary vertices, which are the lever arm of the analysis (the most demanding part in terms of vertexing), the smearing of the longitudinal-transverse direction of these vertices are applied following their fitted pdf. The model and their parameters used to smear the vertices for the IDEA working points are given in Table 11.

Vertex smeared / model	Parameter	IDEA baseline	IDEA $2\times\Omega$	IDEA $1.2\times$ IP	IDEA $1.5\times$ IP	IDEA $2\times$ IP
PV x / Gauss$(x,0,\sigma)$	σ(µm)	4.13	4.04	3.67	3.26	2.56
PV y / Gauss$(x,0,\sigma)$	σ(µm)	2.38e^{-2}	2.38e^{-2}	2.38e^{-2}	2.38e^{-2}	2.38e^{-2}
PV z / Gauss$(x,0,\sigma)$	σ(µm)	2.93	2.59	2.40	2.09	1.32
SV L / 3-Gauss$(x,0,\sigma_1,\sigma_2,\sigma_3,f_1,f_2,f_3)$	σ_1(µm)	19.20	18.67	13.57	11.48	8.60
	σ_2(µm)	49.63	47.57	31.86	27.79	20.70
	σ_3(µm)	171.16	163.67	93.19	87.75	66.09
	f_1	0.46	0.46	0.36	0.41	0.43
	f_2	0.42	0.43	0.48	0.45	0.44
	f_3	0.12	0.11	0.16	0.14	0.13
SV T / 3-Gauss$(x,0,\sigma_1,\sigma_2,\sigma_3,f_1,f_2,f_3)$	σ_1(µm)	2.78	2.69	2.05	1.66	1.14
	σ_2(µm)	7.38	7.21	5.04	4.31	2.75
	σ_3(µm)	28.93	27.82	16.27	15.20	8.55
	f_1	0.60	0.60	0.54	0.58	0.53
	f_2	0.33	0.34	0.37	0.35	0.37
	f_3	0.07	0.06	0.09	0.07	0.10
TV L / 3-Gauss$(x,0,\sigma_1,\sigma_2,\sigma_3,f_1,f_2,f_3)$	σ_1(µm)	12.36	12.02	9.70	7.45	5.78
	σ_2(µm)	27.01	25.97	20.66	15.46	12.44
	σ_3(µm)	89.27	87.59	67.58	47.49	43.52
	f_1	0.50	0.49	0.48	0.45	0.52
	f_2	0.40	0.42	0.43	0.45	0.40
	f_3	0.09	0.09	0.09	0.10	0.08
TV T / 3-Gauss$(x,0,\sigma_1,\sigma_2,\sigma_3,f_1,f_2,f_3)$	σ_1(µm)	2.16	2.08	1.62	1.29	0.91
	σ_2(µm)	5.89	5.72	4.17	3.48	2.30
	σ_3(µm)	25.83	25.22	15.29	14.02	8.05
	f_1	0.64	0.64	0.60	0.63	0.62
	f_2	0.31	0.31	0.34	0.31	0.31
	f_3	0.05	0.05	0.06	0.05	0.07

Table 11: Summary of the fitted model used to emulate the IDEA working points resolutions in the analysis. Gauss denotes a Gaussian P.D.F. and 3-Gauss denotes a 3 Gaussian P.D.F.s defined as the linear combination of three Gaussian P.D.F.s. Resolution fits are always centered on 0.

In concrete order to perform the ellipsoidal smearing of the secondary and tertiary vertices, an accept/reject algorithm enhanced in 2D is used to smear each vertex following its associated resolution. As an illustration, a 2D smearing generation is displayed in Figure 49 for both secondary and tertiary vertices for the IDEA baseline working point. The IDEA working points are used in the analysis following the same way as the fast emulation points: the reconstruction is performed for it; then the same selection is applied; the precision of the branching fraction measurement is accessed. The precision fits of the IDEA baseline working points are displayed in Figure 50; the ones corresponding to the other configurations are given in Appendix ??.

9.4 IDEA results and vertexing requirements

The detailed results of the IDEA working points are available in Table 12. The precision in the measurement of the branching fraction is shown in Figure 51 (only the longitudinal configuration 20 µm for readability) and Figure 52, where the IDEA working points are displayed on the same plot as the fastly emulated one. The comparison between the IDEA working points and the

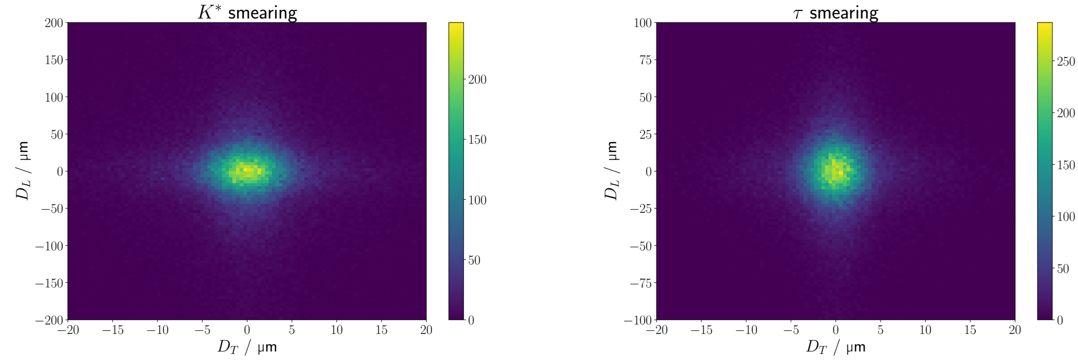

Figure 49: Generation of 100000 smearing for the IDEA vertexing working point on secondary (left) and tertiary (right) vertices, D_T denotes the transverse smearing and D_L the longitudinal one.

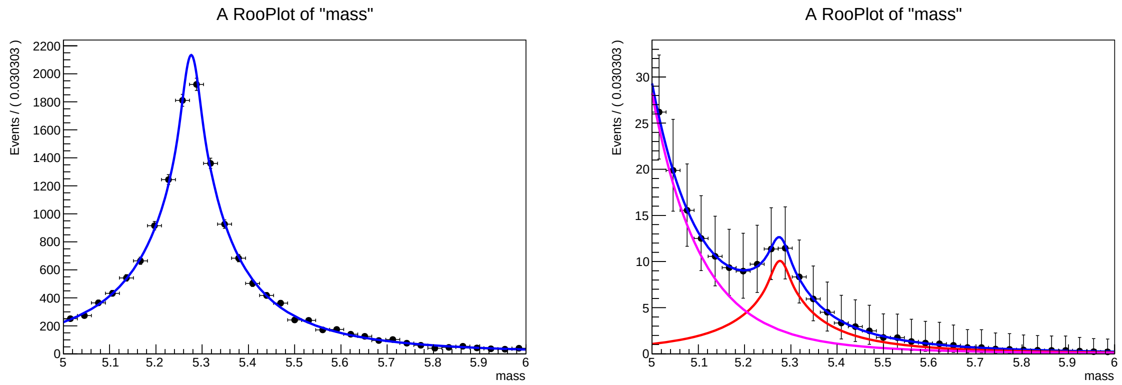

Figure 50: Fit of the signal (left) and of signal + background (right) in order to determine the precision on the BF measurement for the IDEA baseline working point.

emulated ones is not totally fair: the IDEA points are indeed placed at the interpolated position w.r.t. the 20 μm longitudinal configuration for a better readability. Both plots confirm that the Ω improvement has a modest impact on precision, while the improvement in IP leads to a far better precision, up to factor 2!

With respect to figures 51 and 52, only a hint of $B^0 \to K^{*0}\tau\tau$ at SM value can be obtained with the baseline state-of-the-art vertex detector. However, improvement of the IP resolutions seems to be the better detector-dependent way to reach at least the evidence of this mode. The twice better IP resolution working point can reach the observation level. The improvements presented in this section are directly applied to the tracks and do not correspond to regular detector improvements, that will be explored in the next section.

It is worth noting that an increase of luminosity by a factor 5 brings this analysis at SM value at the level of observation with a state-of-the-art detector (see Figure 53).

IDEA smearing configuration	IDEA baseline	IDEA $2\times\Omega$	IDEA $1.2\times$IP	IDEA $1.5\times$IP	IDEA $2\times$IP
N_{signal}	66.08	66.76	77.49	85.23	100.06
$\sigma_{N_{signal}}$	23.32	22.98	21.52	19.25	17.44
Precision	0.35	0.34	0.28	0.23	0.17

Table 12: Precision on the branching fraction measurement for the various IDEA working points

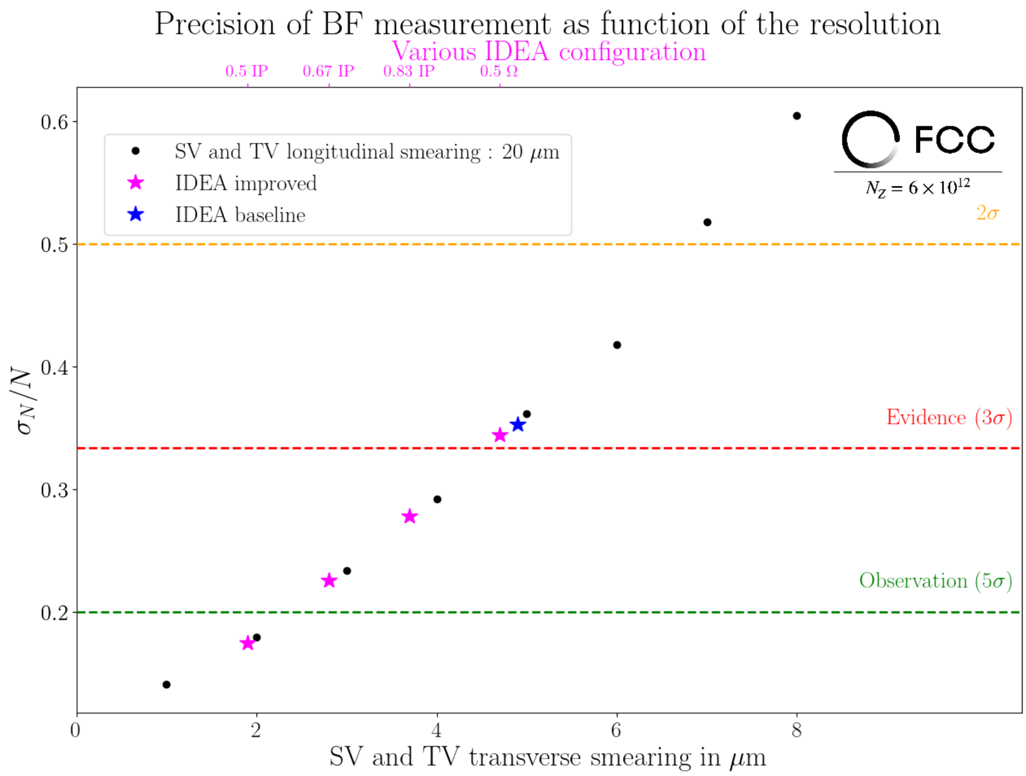

Figure 51: Precision of the measurement as function of the transverse vertexing resolution with a longitudinal resolution set at 20 µm for the fast vertexing working point and the addition of the IDEA working points.

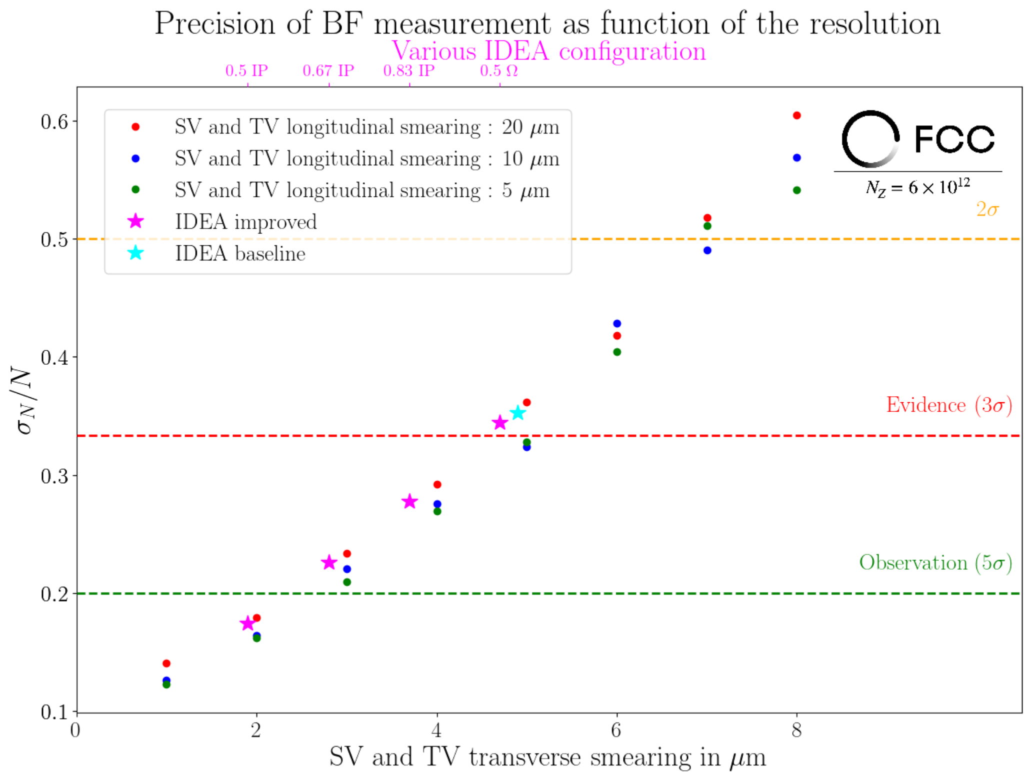

Figure 52: Precision of the measurement as function of the transverse vertexing resolution with all the longitudinal resolutions for the fast vertexing working point and the addition of the IDEA working points.

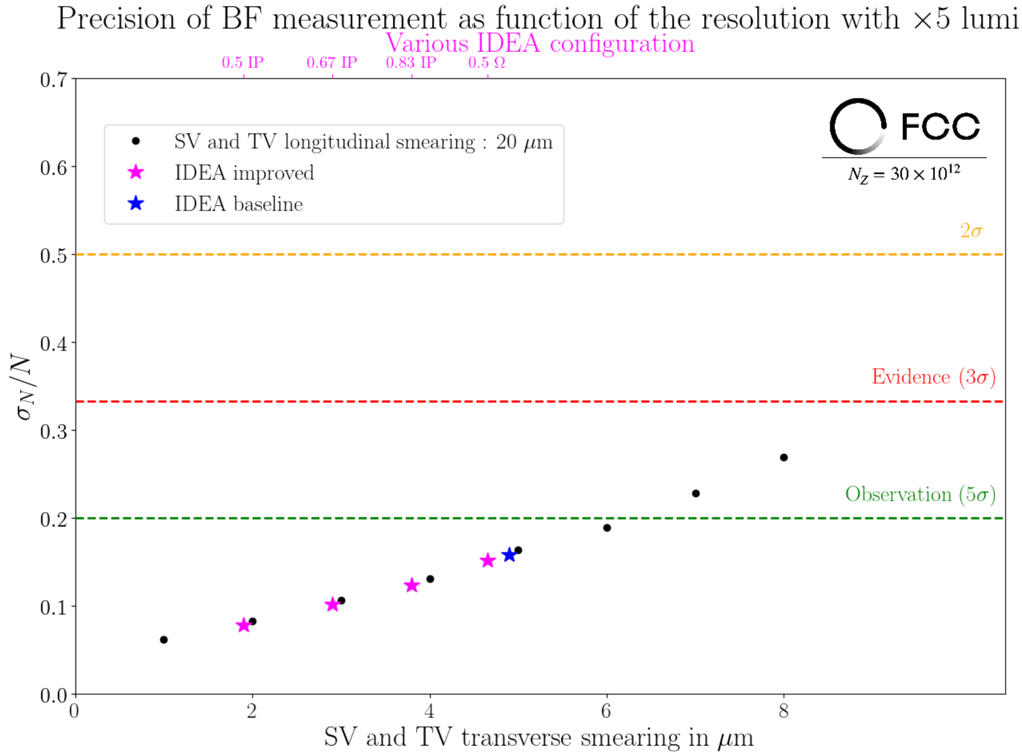

Figure 53: Precision of the measurement as function of the transverse vertexing resolution with a longitudinal resolution set at 20 µm for the fast vertexing working point and the additions of the IDEA working points, with in each case a five times higher luminosity.

9.5 Regular detector improvements

Motivated by the conclusion of Section 9.4, three signal samples with improved vertex detectors have been generated. The first sample features a 30% improvement of the vertex detector single hit resolution, by bringing it from 3 µm to 2 µm for the barrel layers. The second sample involves a 50% reduction of the material budget in the vertex detector layers. The third sample plays a 50% reduction of the material budget in the vertex detector layers and in the beam-pipe.

The generic transverse impact parameter resolution formula, involving the detector characteristics, reads as:

$$\sigma_{\mathrm{d}_0} \simeq \sqrt{\frac{r_2^2\sigma_1^2 + r_1^2\sigma_2^2}{(r_2 - r_1)^2}} \oplus \frac{r}{p_T \sin^{1/2}\theta} 13.6\,\mathrm{MeV} \sqrt{\frac{x}{X_0}}, \tag{9.3}$$

where the first term is linked to detector resolution and the second to multiple scattering (depending at first order on p_T^{-1}). The quantity $r_{1(2)}$ is the distance between the first (second) hit of the track and the PV; $\sigma_{1(2)}$ is the resolution on the first (second) hit of the track; r is the distance between the PV and the contact points of the track with the vertex detector layer; p_T is the transverse momentum of the track; θ is the polar angle of the track, x is the thickness and X_0 is the radiation length. Practically, improvements on single hit resolution are expected to decrease linearly the first term, while material budget reductions play linearly with the thickness and so with a square root dependence on the second term.

The first check performed consisted in understanding whether the detector improvements play as expected on the d_0 resolution. For that purpose, the distribution of the differences between the MC truth and the reconstructed d_0 has been determined for the signal tracks on all samples, in several p_T^{-1} bins. Then, resolutions are given in each bin by the sigma fitted with a double crystal ball model (the power law threshold parameter is fixed in all the bins to the one fitted in the higher p_T bin corresponding to the better defined tracks). Finally, the

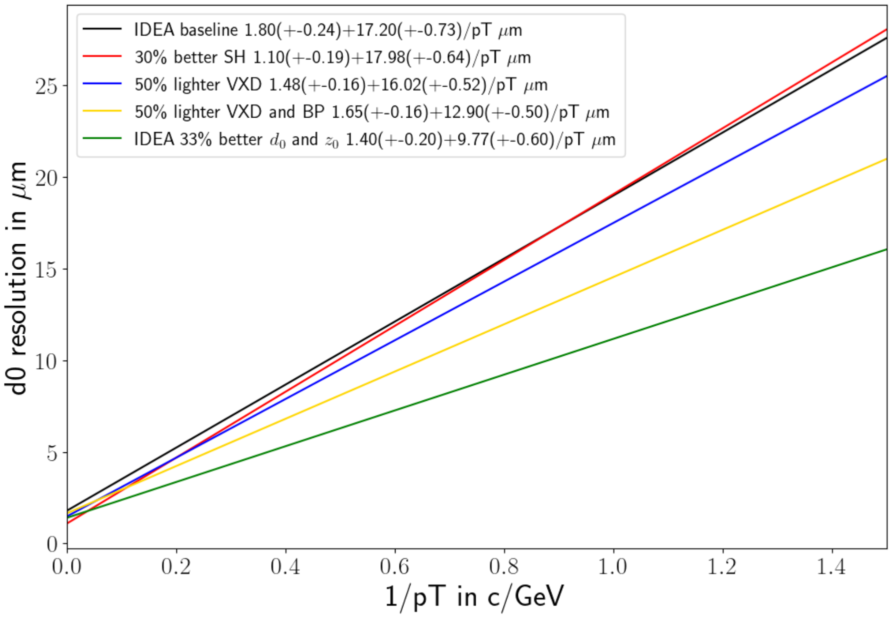

Figure 54: d_0 resolution fits corresponding to IDEA baseline, a detector with a 30% better single hit resolution, a detector with 50% lighter VerteX Detector (VXD) layers, a detector with 50% lighter VXD layers and Beam Pipe (BP), and IDEA with 33% better IP.

sigma fitted and the associated errors are used to fit the d_0 resolution as a function of p_T^{-1} with a linear function. Figure 54 shows that, compared to IDEA, the detector with improved single hit resolution enhanced the offset of the fit linearly, as expected; and detectors with reduced material budget display the expected square root enhancement of the slope only if the beam pipe and the vertex detector layers are both concerned.

This behaviour is expected since the slope is dominated by multiple Coulombian scatterings and is already limited by the beam pipe material. On the other hand, the direct track improvements applied to IDEA simulation are far too optimistic. Actually, they can only be recovered if one reduces the beam pipe material, which dominates the multiple Coulombian scatterings contributions. Any significant further improvement goes therefore via a reduction of the beam pipe material.

In order to look for the impact of regular detector improvements in the analysis, the precision of the branching fraction measurement has been evaluated for three new working points corresponding to their vertexing performance emulations, following all the previously defined methods. Appendix **??** shows the intermediate plots. Figure 55 and Table 13 show the precision results. Finally, the regular detector improvements simulated allow one to reach the 3σ threshold but still fail to reach the observation at SM value of the branching fraction. The material budget reduction is as expected the way to reduce the Coulombian scatterings and to improve the measurement status, but the configurations presented here are already very optimistic. With the baseline luminosity, going beyond the observation of the process at SM value level would require new vertex detector designs. The figure 56 displays the invariant-mass distribution obtained with state-of-the-art vertex detector performance.

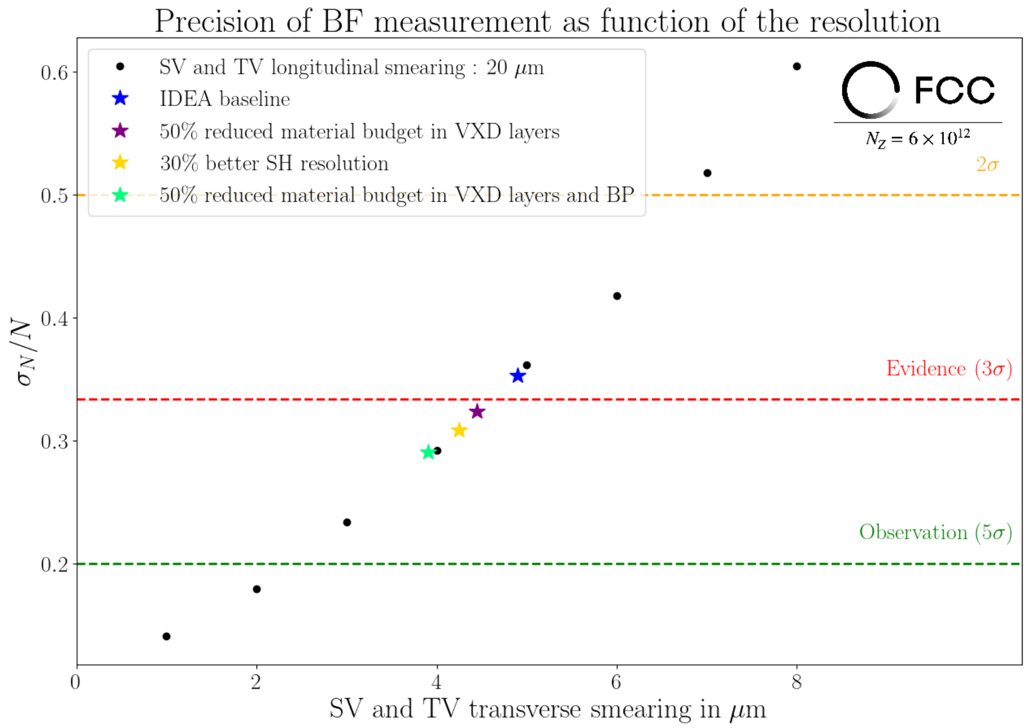

Figure 55: Precision of the measurement as function of the transverse vertexing resolution with a longitudinal resolution set at 20 µm for the fast vertexing working points in addition of the IDEA baseline and regular improved detector working points.

Configuration	IDEA baseline	50% lighter VXD layers	30% better SH resolution	50% lighter VXD layers and BP
N_{signal}	66.08	68.47	70.70	74.03
$\sigma_{N_{\text{signal}}}$	23.32	22.14	21.83	21.52
Precision	0.35	0.32	0.31	0.29

Table 13: Table of the precision on the branching fraction measurement for the IDEA baseline and regular improved detector working points

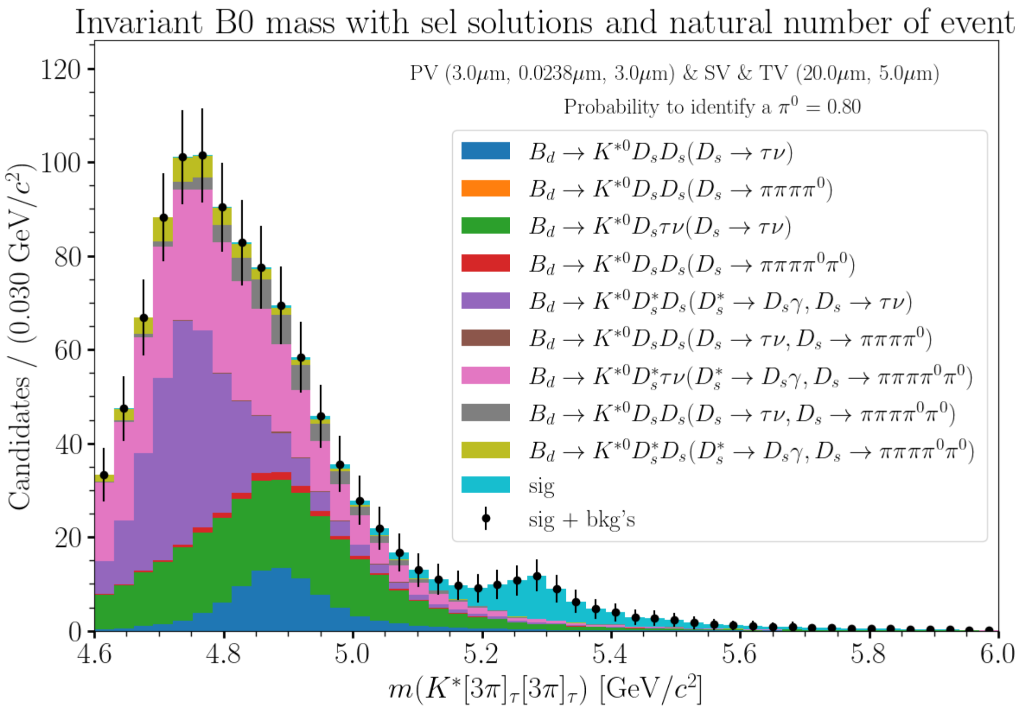

Figure 56: Invariant-mass distribution of the B^0 candidates after the XGBoost selection for the working point that would correspond to the actual IDEA state-of-the-art vertex detector performance: $20 - 5\mu\text{m}$.

10 Conclusion

The scientific context of the study and measurements of the decay mode $B^0 \to K^{*0}\tau^+\tau^-$ is presented. It is used accordingly to provide vertex detector requirements. A method to reconstruct the two undetected neutrinos of $B^0 \to K^{*0}\tau^+\tau^-$ with $\tau \to \pi\pi\pi\nu$ is developed and validated through simulated signal samples. A complete analysis workflow is developed and tested on signal sample with in particular a dedicated emulation of vertexing performances to test several hypotheses. Regarding the small yield of signal expected and for the completeness of the analysis, the possible backgrounds are explored and the dominant ones are considered. Because of the importance of the backgrounds with respect to the signal, an ML based selection is built via the use of the most discriminative variables inside an XGBoost algorithm. After selection, the method to extract the BF($B^0 \to K^{*0}\tau^+\tau^-$) measurement precision as function of the vertex measurement resolution is presented and used on fastly emulated vertexing working points. Finally, thanks to recent improvements in the FCC-*ee* software, several state-of-the-art vertex detector performance working points (baseline + various ones) are added into the analysis.

The main goal of the study is to draw the requirements on vertex detector performances to observe $B^0 \to K^{*0}\tau^+\tau^-$ at FCC-*ee*. It is achieved first by the use of the emulated vertexing performances working points, which provides the information that the level arm to make the measurement is the vertexing performances on the secondary/tertiary vertices projected in the transverse plan of the decaying particle direction, and gives the target of a 2 µm transverse resolution to reach the observation (5σ threshold) or 4 µm to 5 µm to meet the evidence (at 3σ threshold) at SM value. In a second step, the use of vertexing configurations based on state-of-the-art simulated vertex detectors show that the baseline detectors only manage to have a hint of the signal at SM value, and the main area to improve the picture is to enhance the Impact Parameters measurement. In a third stage, vertexing configurations based on regular detector improvements show that the best way to improve the picture is to reduce the material budget in both the vertex detector layers and the beam-pipe. But it seems difficult with actual vertex detector design. Naturally, another way to improve performances without any change on the detector could be to make an experiment with higher integrated luminosity; several improved instantaneous luminosity designs are being considered [40]. For that, one possibility is tested with a times 5 hypothesis, and in that case the observation becomes possible with the state-of-the-art performances.

At the moment to conclude on this work, one has to keep in mind that the goal is not to provide the ultimate analysis to make the observation; there will certainly be, at the moment to manipulate real data, room for several improvements. For example, the selection done in this analysis is a first educated one, but it is certainly possible to find other interesting discriminative variables to train the MVA, and even at the MVA place one can imagine that to apply two MVA in place of one, each one trained against one type of background depending on the D_s decay ($\tau\nu$ or $3\pi n\pi^0$). In addition, despite the luminosity or detector improvements assumptions, another way to improve the probability to make this mode could be to consider other τ channels, for example, taking one leptonic τ decay could bring a factor seven for the signal statistic, and considering fully leptonic τ decays could bring a factor fourteen. But in both cases the reconstruction itself becomes more demanding due to the presence of one or two additional missing neutrinos, and other methods will have to be developed. As a last word, all the work reported here is done under the SM hypothesis, if New Physics plays in $B^0 \to K^{*0}\tau^+\tau^-$ one can imagine its BF to be higher than expected, allowing the state-of-the-art detector to make the measurement and to discover a clear discrepancy with the SM.

11 Analysis repositories / data preservation

Three Github/Gitlab repositories have been created that contain the scripts used at different steps of the analysis.

The version of FCCAnalyses containing all the analyzers used and the scripts needed to produce .root tuples ready for resolution determination is available at `https://github.com/Tristan63170/FCCAnalyses/tree/FCCAnalyses_V_ANAnote_B2KstTauTau`, on the FCCAnalyses_V_ANAnote_B2KstTauTau branch.

The scripts used to perform the reconstruction with the emulation of the vertexing performance and saving the analysis variables, which have been used in SWAN [41], are available in `https://gitlab.cern.ch/tmiralle/fcc_bd2ksttautau_lpc/-/tree/master/`.

The notebooks used to determine the resolutions, build the selection, and determine the precision on the BF measurement are at `https://github.com/Tristan63170/FCC_Bd2KstTauTau_results`.

A README is available for each repository.

References

[1] JF Kamenik, S Monteil, A Semkiv, and L Vale Silva. Lepton polarization asymmetries in rare semi-tauonic $b \to s$ exclusive decays at fcc-ee. *The European Physical Journal C*, 77(10):1–19, 2017.

[2] Paul Langacker. The physics of heavy z' gauge bosons. *Reviews of Modern Physics*, 81(3):1199, 2009.

[3] I Dorsner, S Fajfer, A Greljo, JF Kamenik, and N Kosnik. Physics of leptoquarks in precision experiments and at particle colliders. *Physics Reports*, 641:1–68, 2016.

[4] Gustavo Castelo Branco, PM Ferreira, L Lavoura, MN Rebelo, Marc Sher, and Joao P Silva. Theory and phenomenology of two-higgs-doublet models. *Physics reports*, 516(1-2):1–102, 2012.

[5] Abdus Salam and J Strathdee. Super-symmetry and non-abelian gauges. *Physics Letters B*, 51(4):353–355, 1974.

[6] TV Dong, T Luo, I Adachi, H Aihara, DM Asner, H Atmacan, V Aulchenko, T Aushev, R Ayad, V Babu, et al. Search for the decay $b^0 \to k^{*0}\tau^+\tau^-$ at the belle experiment. *Physical Review D*, 108(1):L011102, 2023.

[7] Roel Aaij, B Adeva, M Adinolfi, Z Ajaltouni, S Akar, J Albrecht, F Alessio, M Alexander, S Ali, G Alkhazov, et al. Search for the decays $b_s^0 \to \tau^+\tau^-$ and $b^0 \to \tau^+\tau^-$. *Physical review letters*, 118(25):251802, 2017.

[8] J De Favereau, Christophe Delaere, Pavel Demin, Andrea Giammanco, Vincent Lemaitre, Alexandre Mertens, Michele Selvaggi, Delphes 3 Collaboration, et al. Delphes 3: a modular framework for fast simulation of a generic collider experiment. *Journal of High Energy Physics*, 2014(2):57, 2014.

[9] G Chiarello, A Corvaglia, F Grancagnolo, A Miccoli, M Panareo, and GF Tassielli. The tracking system for the idea detector at future lepton colliders. *Nuclear Instruments and Methods in Physics Research Section A: Accelerators, Spectrometers, Detectors and Associated Equipment*, 936:503–504, 2019.

[10] R Aly, M Antonello, P Azzi, F Bedeschi, G Bencivenni, L Borgonovi, MLM Caccia, X Chu, G Cibinetto, T Coates, et al. First test-beam results obtained with idea, a detector concept designed for future lepton colliders. *Nuclear Instruments and Methods in Physics Research Section A: Accelerators, Spectrometers, Detectors and Associated Equipment*, 958:162088, 2020.

[11] Marzia Bordone, Claudia Cornella, Javier Fuentes-Martin, and Gino Isidori. A three-site gauge model for flavor hierarchies and flavor anomalies. *Phys. Lett. B*, 779:317–323, 2018.

[12] A Augusto Alves Jr, LM Andrade Filho, AF Barbosa, I Bediaga, G Cernicchiaro, G Guerrer, HP Lima Jr, AA Machado, J Magnin, F Marujo, et al. The lhcb detector at the lhc. *Journal of instrumentation*, 3(08):S08005, 2008.

[13] Paolo Branchini. The belle ii experiment: Status and prospects. *Universe*, 4(10):101, 2018.

[14] Roel Aaij, B Adeva, M Adinolfi, A Affolder, Z Ajaltouni, S Akar, J Albrecht, F Alessio, M Alexander, S Ali, et al. Test of lepton universality using $b^+ \to k^+\ell^+\ell^-$ decays. *Physical Review Letters*, 113(15):151601, 2014.

[15] LHCb Collaboration et al. Measurement of lepton universality parameters in $b^+ \to k^+\ell^+\ell^-$ and $b^0 \to k^{*0}\ell^+\ell^-$ decays. *Physical Review D-Particles, Fields, Gravitation and Cosmology*, 2023.

[16] Roel Aaij, B Adeva, M Adinolfi, A Affolder, Z Ajaltouni, S Akar, J Albrecht, F Alessio, M Alexander, S Ali, et al. Measurement of the ratio of branching fractions b ($b^0 \to d^{*+}\tau^-\nu_\tau$)/ b ($b^0 \to d^{*+}\mu^-\nu_\mu$). *Physical review letters*, 115(11):111803, 2015.

[17] Alejandro Alfonso Albero, Alexey Badalov, Miriam Calvo Gomez, Alessandro Camboni, Samuel Coquereau, G Fernandez, Lluis Garrido Beltran, David Gascon Fora, Ricardo Graciani Diaz, Carla Marin Benito, et al. Measurement of the ratio of the $b^0 \to d^{*+}\tau^-\nu_\tau$ and $b^0 \to d^{*+}\mu^-\nu_\mu$ branching fractions using three-prong τ-lepton decays. *Physical Review Letters, 2018, vol. 120, num. 17, p. 171802*, 2018.

[18] LHCb Collaboration et al. Angular analysis of the b^0ß$k^{*0}\mu^+\mu^-$ decay using 3 fb- 1 of integrated luminosity. *Journal of High Energy Physics*, 2016(2):1–79, 2016.

[19] S Wehle, C Niebuhr, S Yashchenko, I Adachi, H Aihara, S Al Said, DM Asner, V Aulchenko, T Aushev, R Ayad, et al. Lepton-flavor-dependent angular analysis of $b \to k^*\ell\ell$. *Physical review letters*, 118(11):111801, 2017.

[20] R. L. Workman et al. Review of Particle Physics. *PTEP*, 2022:083C01, 2022.

[21] Asmaa Abada, Marcello Abbrescia, Shehu S AbdusSalam, I Abdyukhanov, J Abelleira Fernandez, A Abramov, Mohamed Aburaia, AO Acar, PR Adzic, Prateek Agrawal, et al. Fcc physics opportunities. *The European Physical Journal C*, 79(6):1–161, 2019.

[22] FCC collaboration et al. Fcc-ee: The lepton collider: Future circular collider conceptual design report volume 2. *European Physical Journal: Special Topics*, 228(2):261–623, 2019.

[23] FCC collaboration et al. Fcc-hh: The hadron collider: Future circular collider conceptual design report volume 3. *European Physical Journal: Special Topics*, 228(4):755–1107, 2019.

[24] W Snoeys, M Campbell, E Cantatore, V Cencelli, R Dinapoli, E Heijne, P Jarron, P Lamanna, D Minervini, V O'Shea, et al. Pixel readout electronics development for the alice pixel vertex and lhcb rich detector. *Nuclear Instruments and Methods in Physics Research Section A: Accelerators, Spectrometers, Detectors and Associated Equipment*, 465(1):176–189, 2001.

[25] Torbjörn Sjöstrand, Stefan Ask, Jesper R Christiansen, Richard Corke, Nishita Desai, Philip Ilten, Stephen Mrenna, Stefan Prestel, Christine O Rasmussen, and Peter Z Skands. An introduction to pythia 8.2. *Computer physics communications*, 191:159–177, 2015.

[26] Anders Ryd, David Lange, Natalia Kuznetsova, Sophie Versille, Marcello Rotondo, DP Kirkby, FK Wuerthwein, and A Ishikawa. Evtgen: a monte carlo generator for b-physics. *BAD*, 522:v6, 2005.

[27] Jim Pivarski, Pratyush Das, Matthew Feickert, Henry Schreiner, Daniel Marley, Ruggero Turra, Chris Burr, Chao Gu, et al. Scikit-hep/uproot: 3.2. 2. *Zenodo*, 2019.

[28] Jim Pivarski, Peter Elmer, and David Lange. Awkward arrays in python, c++, and numba. In *EPJ Web of Conferences*, volume 245, page 05023. EDP Sciences, 2020.

[29] Yasmine Amhis, Sw Banerjee, Eli Ben-Haim, Florian Urs Bernlochner, Marcella Bona, Andrzej Bozek, Concezio Bozzi, Jolanta Brodzicka, M Chrzaszcz, J Dingfelder, et al. Averages of b-hadron, c-hadron, and τ τ-lepton properties as of 2018: Heavy flavor averaging group (hflav). *The European Physical Journal C*, 81:1–326, 2021.

[30] LHCb collaboration. First observation of the $b^+ \to d_s^+ d_s^- k^+$ decay, 2022.

[31] RH Dalitz. Cxii. on the analysis of τ-meson data and the nature of the τ-meson. *The London, Edinburgh, and Dublin Philosophical Magazine and Journal of Science*, 44(357):1068–1080, 1953.

[32] Lingfeng Li and Tao Liu. b$\to$ sτ+ τ- physics at future z factories. *Journal of High Energy Physics*, 2021(6):1–31, 2021.

[33] Kevin Kroeninger, Romain Madar, Stéphane Monteil, Fabrizio Palla, and Lars Roehrig. Reconstructed exclusive b-hadron decays as hemisphere jet charge tagger and its application for the measurement of R_b and A^b_{FB}, September 2023.

[34] Damir Buskulic, D Casper, I De Bonis, D Decamp, P Ghez, C Goy, J-P Lees, M-N Minard, P Odier, B Pietrzyk, et al. Performance of the aleph detector at lep. *Nuclear Instruments and Methods in Physics Research Section A: Accelerators, Spectrometers, Detectors and Associated Equipment*, 360(3):481–506, 1995.

[35] Tianqi Chen and Carlos Guestrin. Xgboost: A scalable tree boosting system. In *Proceedings of the 22nd acm sigkdd international conference on knowledge discovery and data mining*, pages 785–794, 2016.

[36] Oliver Kramer and Oliver Kramer. Scikit-learn. *Machine learning for evolution strategies*, pages 45–53, 2016.

[37] Vance W Berger and YanYan Zhou. Kolmogorov–smirnov test: Overview. *Wiley statsref: Statistics reference online*, 2014.

[38] Wouter Verkerke and David Kirkby. The roofit toolkit for data modeling. In *Statistical Problems in Particle Physics, Astrophysics and Cosmology*, pages 186–189. World Scientific, 2006.

[39] Jonas Eschle, Albert Puig Navarro, Rafael Silva Coutinho, and Nicola Serra. zfit: Scalable pythonic fitting. *SoftwareX*, 11:100508, 2020.

[40] FCC Collaboration. Future Circular Collider (FCC) Feasibility Study Midterm Report.

[41] Danilo Piparo, Enric Tejedor, Pere Mato, Luca Mascetti, Jakub Moscicki, and Massimo Lamanna. Swan: A service for interactive analysis in the cloud. *Future Generation Computer Systems*, 78:1071–1078, 2018.